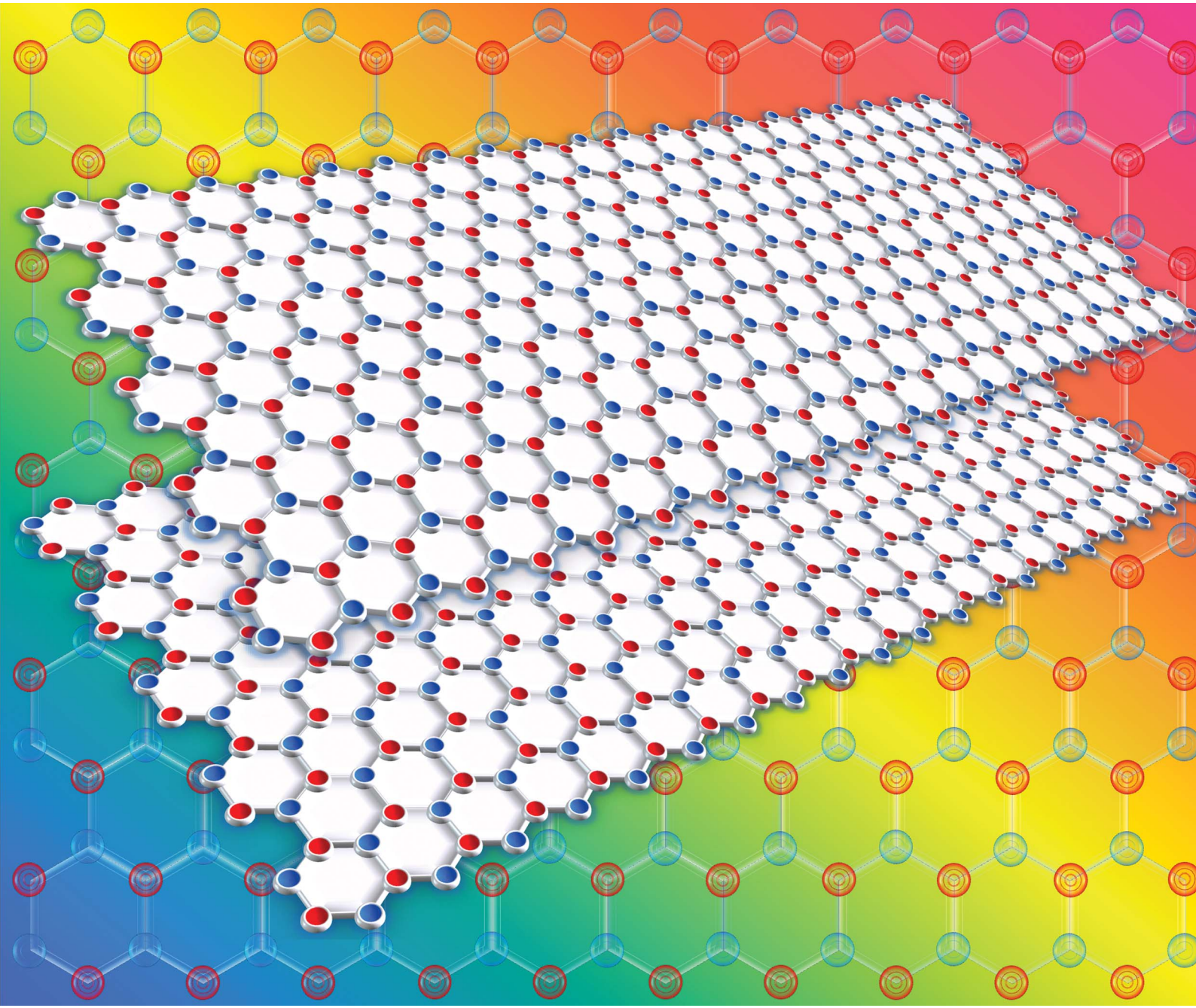


# Nanoscale

[www.rsc.org/nanoscale](http://www.rsc.org/nanoscale)

Volume 4 | Number 22 | 21 November 2012 | Pages 6889–7282



ISSN 2040-3364

**COVER ARTICLE**  
Lin and Connell  
Advances in 2D boron nitride nanostructures: nanosheets, nanoribbons, nanomeshes, and hybrids with graphene



**NCNST**



2040-3364 (2012) 4:22;1-G

RSC Publishing

Cite this: *Nanoscale*, 2012, **4**, 6908

[www.rsc.org/nanoscale](http://www.rsc.org/nanoscale)

REVIEW

## Advances in 2D boron nitride nanostructures: nanosheets, nanoribbons, nanomeshes, and hybrids with graphene

Yi Lin<sup>\*a</sup> and John W. Connell<sup>b</sup>

Received 8th August 2012, Accepted 31st August 2012

DOI: 10.1039/c2nr32201c

The recent surge in graphene research has stimulated interest in the investigation of various 2-dimensional (2D) nanomaterials. Among these materials, the 2D boron nitride (BN) nanostructures are in a unique position. This is because they are the isolectric analogs to graphene structures and share very similar structural characteristics and many physical properties except for the large band gap. The main forms of the 2D BN nanostructures include nanosheets (BNNSs), nanoribbons (BNNRs), and nanomeshes (BNNMs). BNNRs are essentially BNNSs with narrow widths in which the edge effects become significant; BNNMs are also variations of BNNSs, which are supported on certain metal substrates where strong interactions and the lattice mismatch between the substrate and the nanosheet result in periodic shallow regions on the nanosheet surface. Recently, the hybrids of 2D BN nanostructures with graphene, in the form of either in-plane hybrids or inter-plane heterolayers, have also drawn much attention. In particular, the BNNS-graphene heterolayer architectures are finding important electronic applications as BNNSs may serve as excellent dielectric substrates or separation layers for graphene electronic devices. In this article, we first discuss the structural basics, spectroscopic signatures, and physical properties of the 2D BN nanostructures. Then, various top-down and bottom-up preparation methodologies are reviewed in detail. Several sections are dedicated to the preparation of BNNRs, BNNMs, and BNNS-graphene hybrids, respectively. Following some more discussions on the applications of these unique materials, the article is concluded with a summary and perspectives of this exciting new field.

<sup>a</sup>National Institute of Aerospace, 100 Exploration way, Hampton, VA 23666, USA. E-mail: yi.lin@nianet.org; Tel: +1-757-864-2219

<sup>b</sup>Advanced Materials and Processing Branch, NASA Langley Research Center, Mail Stop 226, Hampton, VA 23681, USA



Yi Lin

*Yi Lin is a senior research scientist at the National Institute of Aerospace and a resident in the Advanced Materials and Processing Branch at the NASA Langley Research Center. He received his B.S. (1996) and M.S. (1999) degrees at the University of Science and Technology of China. He earned his Ph.D. in chemistry in 2004 at Clemson University. He was a research assistant professor in the Department of Chemistry at Clemson University in 2004–2006 and became a NASA postdoctoral fellow in 2007. He joined the National Institute of Aerospace in 2009. He has also been an adjunct assistant professor in the Department of Applied Science at the College of William and Mary since 2011. He is the author of over 70 peer-reviewed journal articles and 6 book chapters.*



John W. Connell

*John W. Connell is a senior scientist in the Advanced Materials and Processing Branch at the NASA Langley Research Center. He received his B.S. (1982) and Ph.D. (1986) degrees from Virginia Commonwealth University. He is the author of 115 journal articles, 150 conference publications, and 40 U.S. Patents. He received the prestigious NASA Medal for Exceptional Scientific Achievement in 1997 and Co-Inventor Commercial Invention of the Year for NASA in 2008. He is the Editor-in-Chief of High Performance Polymers Journal and a Fellow of the Institute of Physics and the Society for the Advancement of Material and Process Engineering (SAMPE).*

## 1. Introduction

Boron nitride (BN) is the lightest Group III–V compound. It closely resembles elemental carbon structures by sharing the same total number of electrons between the neighboring atoms.<sup>1</sup> For example, graphite and diamond, the two most common carbon allotropes, consist of  $sp^2$  conjugated carbon (*i.e.*, graphene) layers and an  $sp^3$  carbon atom network, respectively. The comparable isolectric BN polymorphs are the hexagonal (h-BN) and cubic BN (c-BN), which similarly consist of layered and tetrahedral structures, respectively. Unlike the carbon fullerenes such as  $C_{60}$ , however, BN fullerenes feature squares or octagons rather than pentagons in order to avoid thermodynamically unfavorable B–B and N–N bonds.<sup>2</sup>

In the “nanomaterials” regime, one-dimensional (1D) boron nitride nanotubes (BNNTs) can be isolectric to carbon nanotubes (CNTs) with the same chirality, diameter, and number of walls.<sup>3</sup> Although two-dimensional (2D) nanomaterials have been discussed for several decades,<sup>4</sup> the current surge of interest in these materials only started in 2004 when Novoselov, Geim and co-workers isolated one-atomic-layer-thick graphene sheets and discovered their extraordinary electronic properties.<sup>5</sup> Since then, other 2D nanomaterials, such as nanosheets of h-BN and various metal chalcogenides, have also drawn attention due to their structural similarities to graphene.<sup>6,7</sup> The electronic properties of most of these graphene-like 2D nanomaterials are perhaps not as intriguing as graphene itself, but other unique combinations of dielectric, electromagnetic, thermoelectric, mechanical, and chemical properties could find superiority in applications if few-layered and monolayer sheets could be isolated experimentally.

Since “graphene” is the formal name for an individual graphite layer, some researchers suggested the use of “boron nitrene”<sup>8</sup> or “boronitrene”<sup>9–12</sup> as the equivalent name for an individual h-BN layer. So far, this nomenclature has not been widely adopted in the literature. A potential for confusion exists as “nitrene” usually refers to the highly reactive neutral compound R–N (similar to carbene RR’C), while N atoms within a perfect h-BN basal plane are covalently bonded with 3 adjacent B atoms. In this review, we choose to use the most common terms in the literature: an individual h-BN layer (*i.e.* a basal plane) is called a “monolayer BN nanosheet (BNNS)”; a thin h-BN crystal with several atomic layers is called a “few-layered BNNS”. There are

also sub-categories within the generally defined “BNNSS” according to different structural and/or topographical characteristics, such as BN nanoribbons (BNNRs; nanosheets with variable lengths but narrow widths typically  $<20$  nm) and BN nanomeshes (BNNMs; metal-supported, epitaxially grown nanosheets with periodically shallow regions/patterns).

In this review, we first discuss the structural characteristics of BNNSs, followed by various experimental results and predictions of their properties. Currently available “top-down” and “bottom-up” synthetic approaches for nanosheets are then reviewed in detail. A section is dedicated to in-plane and inter-plane BN–graphene hybrid structures, both of which have attracted significant attention recently. Applications and research perspectives for these novel 2D BN nanostructures are also presented.

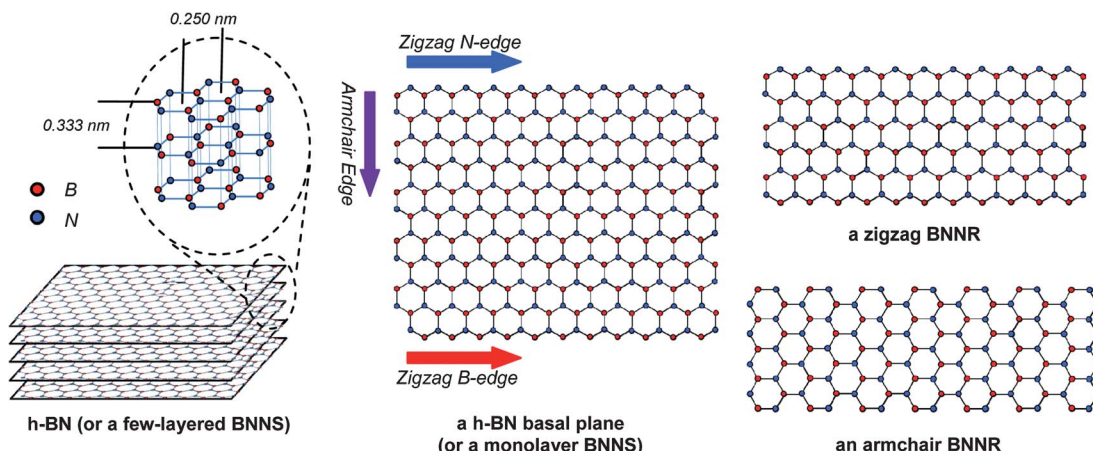
## 2. Structural characteristics

### 2.1. Structural basics

As shown in Scheme 1, an individual h-BN basal plane, or a monolayer BNNS, is a honeycomb structure made up of ring units of borazine ( $B_3N_3H_6$ ), the isolectric and isostructural analog of benzene. The B–N bonds, covalent in nature but with ionic characteristics, are  $1.45\text{ \AA}$  in length. The distance between the centers of neighboring borazine rings is  $2.50\text{ \AA}$  (vs.  $2.46\text{ \AA}$  for a graphene basal plane). The edge of a nanosheet/nanoribbon could be either zigzag (B- or N-edged) or armchair (BN pair-edged).

The lateral sizes for h-BN crystals in commercially available powder are typically in the range of a few hundred nanometers to tens of microns. BNNSSs obtained from exfoliating these crystals are often of similar or smaller lateral sizes,<sup>7,13–16</sup> while those from chemical vapor deposition (CVD) growth could be as large as a few centimeters.<sup>17–19</sup> The transmission electron microscope (TEM) image in Fig. 1a shows a BNNS (from chemical functionalization and exfoliation<sup>16</sup>) with a diagonal lateral size of  $\sim 700$  nm.

Multiple basal planes stack on top of each other to form few-layered BNNSSs (or a thin h-BN crystal *per se*), with the neighboring layers held by van der Waals forces at a distance of  $0.333\text{ nm}$  (vs.  $0.337\text{ nm}$  for few-layered graphene or graphite).



Scheme 1 Structural basics of 2D BN nanostructures.

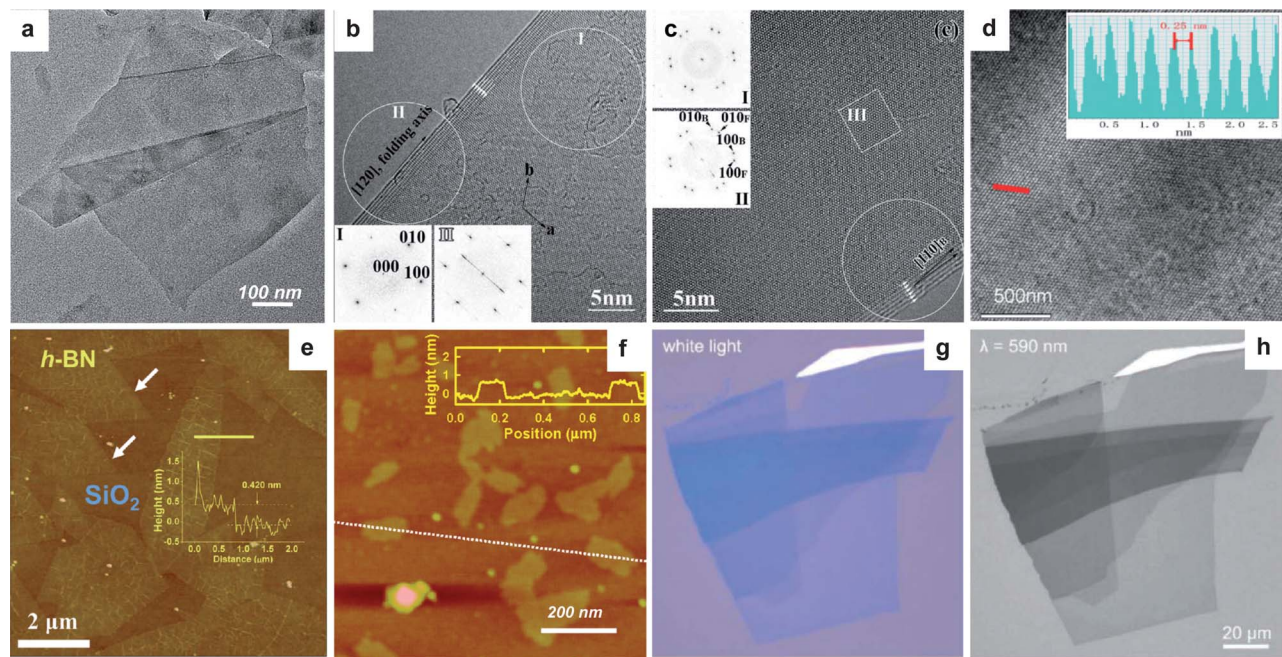


**Fig. 1** Microscopy images of BNNSs. (a) A low-magnification TEM image of an exfoliated six-layered BNNS.<sup>16</sup> (b) and (c) are HR-TEM images of two exfoliated six-layered BNNSs of rotation angles of 0° and 13.8° at their folded edges, respectively.<sup>14</sup> Insets I and II in (b) are the electron diffraction patterns corresponding to the circled areas. Insets I and II in (c) are the electron diffraction patterns from the whole image and the circled area, respectively. Inset III in (c) is a simulated image showing a Moiré pattern in good agreement with the experimental image. (d) A HR-TEM image of an exfoliated few-layered BNNS showing the atomic lattice with a constant of 0.25 nm (inset: intensity profile along the red line). The lack of a Moiré pattern indicates a perfect AA' stacking order.<sup>15</sup> (e) An AFM image of CVD-grown monolayer BNNSs (inset: height profile along the yellow line). The white arrows indicate the sharp edges of the nanosheets.<sup>19</sup> (f) An AFM image of water-exfoliated monolayer BNNSs (inset: height profile along the white line).<sup>21</sup> (g) and (h) are optical images of the same mechanically exfoliated BNNS on a 90 nm SiO<sub>2</sub>/Si wafer under white light and a specific wavelength of incident light ( $\lambda = 590$  nm), respectively.<sup>20</sup> Reproduced with permission from ref. 16 (Copyright © 2010 American Chemical Society), ref. 14 (Copyright © 2008 American Institute of Physics), ref. 15 (Copyright © 2009 Wiley-VCH), ref. 19 (Copyright © 2012 American Chemical Society), ref. 21 (Copyright © 2011 American Chemical Society), and ref. 20 (Copyright © 2011 Wiley-VCH), respectively.

The most straightforward method to determine the layer number of a BNNS is to directly count the straight lines at the folded edges in high resolution TEM (HR-TEM) imaging (Fig. 1b), which is also capable of differentiating atomic lattices of BNNSs (Fig. 1b-d).<sup>13-19</sup> Alternatively, the layer numbers can be extrapolated from the step height information of the nanosheet obtained *via* using an atomic force microscope (AFM).<sup>13,16-21</sup> Typically, monolayer BNNSs from mechanical exfoliation<sup>20</sup> and CVD growth<sup>19</sup> have a height of ~0.4 nm (Fig. 1e) despite trapped moisture under ambient conditions.<sup>22</sup> However, for wet-exfoliated nanosheets, the trapped solvents between a monolayer BNNS and the underlying substrate might make its AFM height close to 1 nm (Fig. 1f), similar to monolayer graphene oxide.<sup>16,21</sup> Other impurities or functional groups on BNNS surfaces might further interfere with the measured height value. Therefore, the layer number extrapolation from AFM height measurements should be reported with caution and preferably confirmed with other techniques.

Because of the convenience, the use of an optical microscope has been popular in the determination of the layer numbers of large area thin graphene sheets due to their relatively high optical contrast in reference to the substrate (usually a standard Si wafer with an ~300 nm SiO<sub>2</sub> layer).<sup>23</sup> However, BNNSs do not absorb in the visible region so that they exhibit a much lower contrast. By investigating large lateral size (~100 μm) BNNSs exfoliated

from h-BN single crystals (also see Section 4.1.1.), Gorbachev *et al.* found that a Si wafer with an ~80 nm SiO<sub>2</sub> layer should be optimal for optical identification of a monolayer and few-layered BNNSs (Fig. 1g and h).<sup>20</sup> The white light contrast reached ~2.5% for a monolayer, which was much lower than in the case of graphene (10%) but sufficient to identify the nanosheets when searching under an optical microscope. The contrast did increase with BNNS layer numbers, and was either positive or negative depending upon the wavelength used.

The stacking orders of the atomic layers in few-layered BNNSs/h-BN and few-layered graphene/graphite are different. The typical stacking of graphene layers is called AB stacking, in which each carbon atom is sitting above the center of a benzene ring in the neighboring layer.<sup>5</sup> In comparison, h-BN and exfoliated few-layered BNNSs typically exhibit AA' stacking, in which each B atom eclipses with an N atom on the adjacent layer due to favorable electrostatic or polar–polar interactions (Scheme 1).<sup>3</sup> These interactions between individual BNNS layers, also referred to as “lip–lip” interactions, are somewhat stronger than those between graphene layers. Therefore, the exfoliation of h-BN has appeared to be more difficult under conditions that are effective for graphene preparation from graphite exfoliation. It is interesting though that such interactions have only a negligible effect on the interlayer distance in comparison to that of graphite.<sup>24</sup>

Although the AA' stacking is always observed in few-layered BNNSs prepared by top-down exfoliation processes,<sup>13–16,21</sup> the nanosheets from some bottom-up synthetic techniques do not necessarily exhibit this stacking order.<sup>17,18</sup> In addition, there have been calculations that suggest that the adjacent BN layers might freely slide from AA' stacking to one of the AB stacking types (N centered on borazine rings on adjacent layers) along certain energetically favorable directions despite a bandgap reduction of ~0.6 eV.<sup>25</sup>

In TEM, Moiré patterns appear from the interference of a transmitted electron due to offset atomic structures at different depths of a sample. Such patterns have been used to resolve the rotational stacking faults in few-layered graphene.<sup>26</sup> Due to the AA' stacking, perfect honeycomb structures with no Moiré interference patterns are typically seen in the TEM image of exfoliated BNNSs, along with one set of hexagonal electron diffraction patterns regardless of the layer number (Fig. 1b and d).<sup>14</sup> However, a folded BNNS, multiple stacked BNNSs, and those with stacking faults (such as the CVD-grown nanosheets) can exhibit Moiré interference characteristics due to the rotation angle between two or more sets of AA' stacked layers. This also causes multiple sets of hexagonal electron diffraction patterns (Fig. 1c, insets I and II).<sup>14</sup>

## 2.2. Defects

Stone–Wales defects in the form of pentagon–heptagon fused rings on BNNSs are thermodynamically unfavorable due to the requirement of formation of B–B or N–N bonds.<sup>2,3</sup> Although theoretical calculations predicted that such defects could be stabilized from the distortion of the nanosheet plane nearby<sup>27</sup> or the formation of squares and octagons, they have rarely been observed experimentally under atomic-resolution HR-TEM.<sup>28–31</sup> This is in clear contrast to sp<sup>2</sup> carbon allotropes such as graphene and CNTs, where Stone–Wales defects are very commonly formed.<sup>32,33</sup>

Vacancy defects, or point defects, seem to be much more common for BNNSs. Because of the unique atomic structure of BNNS basal planes, *i.e.*, the alternating B and N atoms, these defects, when under a few nanometers in size, often exhibit well-defined geometrical shapes (mostly triangles and sometimes hexagons). Several research groups independently reported such defects from mechanically or solvent exfoliated few-layered BNNSs that were further thinned down to a monolayer by an electron beam or reactive ion etching.<sup>28–31</sup> Discrete sizes of normal triangular-shaped holes were observed upon electron beam irradiation under HR-TEM, with the smallest ones corresponding to mono-vacancy (missing only one atom in the lattice) (Fig. 2). Interestingly, almost all triangles had the same orientation on one monolayer and the opposite direction on the adjacent layer. This indicated that the same type of vacancy (B or N) was not only within the same basal plane, but also throughout the entire few-layered structure. By differentiating B and N atoms using exhaustive techniques,<sup>28,30</sup> some researchers were able to identify the observed vacancies as missing B atoms. This left dominating zigzag N-edges, although both armchair edges (exposed B–N pairs) and hexagonal vacancies (partially B- and partially N-zigzag edged or armchair B–N-edged) were also occasionally observed.<sup>30,31</sup>

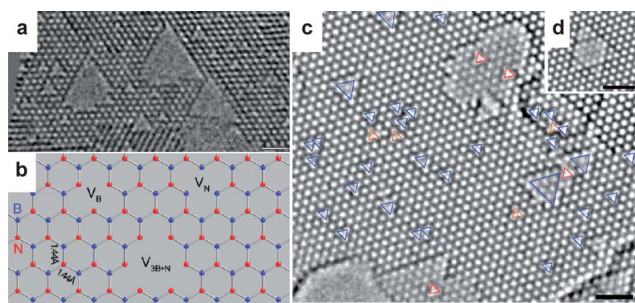


**Fig. 2** Vacancy defects of BNNSs. (a) A monolayer BNNS: different sizes of triangular vacancies had the same orientation.<sup>28</sup> (b) A model for vacancy defects on a monolayer BNNS:  $V_B$  and  $V_N$  stand for B and N monovacancies, respectively. Note:  $V_B$  and  $V_{3B+N}$  have the same orientation with N-edges, while  $V_N$  (and  $V_{3N+B}$ , not shown) ones have opposite directions with B-edges.<sup>28</sup> (c) A mostly bilayer BNNS: triangular vacancies are in the same orientation on one layer (blue) – with only a few exceptions (brown) – but in the opposite orientation in the adjacent layer (red).<sup>29</sup> (d) Triangular vacancies in opposite orientations on adjacent layers of a 3-layered BNNS.<sup>29</sup> Scale bars = 1 nm. Reproduced with permission from ref. 28 (Copyright © 2009 American Physical Society) and ref. 29 (Copyright © 2009 American Chemical Society), respectively.

The mechanism causing the dominating observance of B vacancies under electron beam irradiation has been debated because prior calculations suggested that N vacancies should be thermodynamically more stable.<sup>34,35</sup> This was initially attributed to the lower knockon energy of B atoms vs. N atoms (74 vs. 84 keV, calculated from a tight-binding model<sup>36</sup>). However, the TEM acceleration voltage used in some cases (*e.g.* 120 kV) was much higher than both values, which should have led to both types of vacancies. Some researchers proposed that the electron-rich environment in TEM might have selectively stabilized negatively charged N-edges (*i.e.*, B vacancies).<sup>37,38</sup>

Alternatively, Kotakoski *et al.* proposed a kinetic model and suggested that, rather than the difference in knockon energy or the stabilization of charged edges, it was the higher B atomic displacement rate under electron irradiation that induced the dominating formation of triangular B vacancies.<sup>39</sup> Such a kinetic model implies that the defect formation preference under other experimental conditions could be different. For example, in a theoretical study investigating the irradiation effect of various noble gas ions instead of an electron beam, Lehtinen *et al.*<sup>40</sup> suggested that the formation probabilities of B and N vacancies (*i.e.* zigzag N- and B-edges) were nearly equal but combined to dominate over double vacancy (*i.e.* armchair edges) in a wide energy range (up to ~100 keV). The latter only occurred at intermediate energies (~0.1 to 1.0 keV).

Both vacancy defects<sup>41</sup> and Stone–Wales defects<sup>42,43</sup> can reduce the bandgap of 2D BN nanostructures. Interestingly, according to several authors,<sup>44–47</sup> B vacancies may induce large spin polarization, leading to half-metallicity (also see Section 3.3.). In contrast, N vacancies have little influence on the magnetic moments of the nanosheets. Conversely, an N adatom (*i.e.*, atomic adsorption on a nanosheet surface) would have a more magnetic influence than a B adatom.<sup>46</sup>

Defects may affect other properties of 2D BN nanostructures. For example, triangular vacancies may induce phonon scattering and thus reduce the thermal conductivity of BNNRs,<sup>48</sup> with the

phonon transport being asymmetric according to the orientation of the triangles.<sup>49</sup> It is now well established that the presence of defects in graphene and CNT can significantly enhance their chemical reactivities.<sup>50</sup> This appears to be also true for 2D BN systems as shown in both theoretical<sup>42,51,52</sup> and experimental<sup>53</sup> studies. For example, Chen and co-workers studied the effect of Stone–Wales defects on BNNRs in detail using gradient-corrected density function theory (DFT).<sup>42</sup> Compared to perfect BNNRs, those with Stone–Wales defects are more reactive toward carbene cycloaddition, with the more exothermic sites at the newly formed B–B and N–N bonds, followed by the 5–7 fused rings. Experimentally, we have recently demonstrated that the Lewis acid–base functionalization–solubilization efficiency of BNNSs may be significantly improved by purposely introducing defects onto the starting h-BN structure (more discussions in Section 4.1.3.).<sup>53</sup>

### 3. Physical properties

#### 3.1. Appearance and absorption properties

BNNSs have no optical absorption in the visible region. Therefore, similar to the white appearance of commercially available powder or transparent single-crystal bulk h-BN,<sup>54–56</sup> BNNSs also appear white in bulk and translucent in dispersions (Fig. 3).<sup>7,15,16,21</sup> Thin films of BNNSs from exfoliation<sup>13,20,57</sup> or CVD-grown (Fig. 3b) are also of high transparency. As h-BN

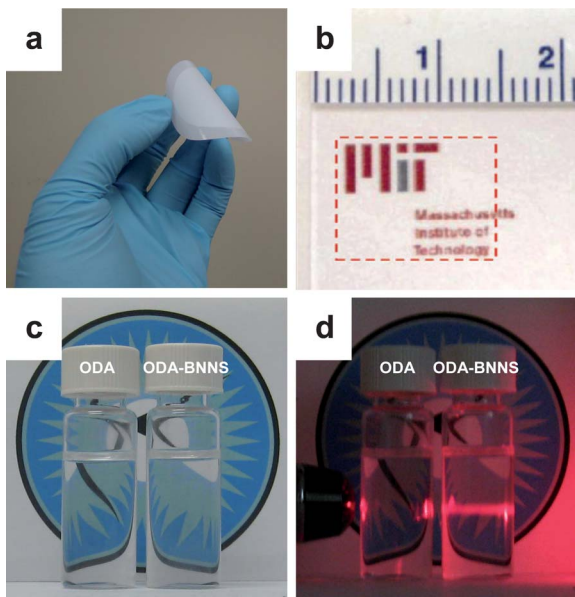


**Fig. 3** Appearances of BNNSs. (a) White-colored exfoliated BNNSs collected on a filter membrane;<sup>21</sup> (b) a highly transparent CVD-grown monolayer BNNS sample on a quartz substrate (indicated by the red dashes);<sup>19</sup> (c) a transparent dilute dispersion of exfoliated BNNSs from chemical functionalization (right) in comparison to that of just the functional molecule [octadecylamine (ODA)] in the same solvent tetrahydrofuran (THF) (left);<sup>16</sup> (d) the same liquids in (c) with the irradiation of a laser beam from the left, showing a Tyndall effect of the dispersion containing BNNSs.<sup>16</sup> Reproduced with permission from ref. 21 (Copyright © 2011 American Chemical Society), ref. 19 (Copyright © 2012 American Chemical Society) and ref. 16 (Copyright © 2010 American Chemical Society), respectively.

is nicknamed “white graphite”, a BNNS has also been called “white graphene”.<sup>58,59</sup> The BNNS dispersions, even when appearing transparent at low concentrations (Fig. 3c), exhibit the Tyndall effect (a visible light path through the dispersion when illuminated with a laser; Fig. 3d) and often appear “milky” at higher concentrations because the lateral dimensions of the nanosheets are larger than the wavelength of the light and cause optical scattering (see more photographs in Section 4.1.2.). The scattering effect dominated the featureless optical spectrum of BNNSs in the visible region. The measured total extinction coefficients ( $\epsilon \sim 10$  and  $3 \text{ L mol}^{-1} \text{ cm}^{-1}$  at 600 and 1000 nm, respectively)<sup>16</sup> were still much lower than that of graphene ( $\sim 300 \text{ L mol}^{-1} \text{ cm}^{-1}$  at 660 nm),<sup>60</sup> for which both absorption and scattering have significant contributions. Dispersions of highly defective and smaller-sized BNNSs showed much higher  $\epsilon$  values ( $\sim 25$  to  $42 \text{ L mol}^{-1} \text{ cm}^{-1}$  at 1000 nm), which might be attributed to the absorption of a distribution of small bandgaps that were opened at the Fermi level due to the presence of defects.<sup>53</sup>

#### 3.2. Spectroscopic signatures

Because of the lack of availability of bulk quantities of BNNSs with exclusively monolayers, most spectroscopic results available to date, with only a few exceptions, were obtained with samples containing mostly few-layered nanosheets with a broad distribution of lateral sizes (tens of nm to  $>1 \mu\text{m}$ ) and layer numbers (from a monolayer to  $\sim 30$  layers or more). Spectroscopic signatures for these BNNS samples are, for the most part, quite similar to their parent h-BN materials. For example, h-BN is a wide bandgap semiconductor–insulator with a peak optical absorption at  $\sim 6 \text{ eV}$  (or  $\sim 206 \text{ nm}$ ).<sup>54,61</sup> Exfoliated few-layered BNNS samples, with or without functionalities attached, seem to retain this property, with experimental results showing similar absorption peak values at  $\sim 6.1 \text{ eV}$  (or  $\sim 203 \text{ nm}$ ) with a very low intensity scattering tail in the visible and near-IR (as discussed in the previous section).<sup>16,21</sup> The peak shifted slightly toward deeper UV for smaller and thinner nanosheets isolated from high speed centrifugation.<sup>21</sup> CVD-grown BNNSs also showed a similar absorption peak at  $\sim 203 \text{ nm}$  (Fig. 4a).<sup>17</sup> According to the Tauc equation, the electronic bandgap can be deduced from the peak to be  $5.56 \text{ eV}$  (or  $\sim 223 \text{ nm}$ ). Results from other CVD synthesis studies showed the bandgap of monolayer and few-layered BNNSs at  $\sim 6.07$  (ref. 19) and  $\sim 5.92 \text{ eV}$ ,<sup>18</sup> respectively. The larger bandgap value for monolayer BNNSs was attributed to the lack of interlayer interactions.<sup>19</sup>

In X-ray photoelectron spectroscopy (XPS), the B 1s ( $\sim 190 \text{ eV}$ ) and N 1s ( $\sim 398 \text{ eV}$ ) peaks for BNNSs (Fig. 4b) were found to be essentially the same as for h-BN.<sup>17,18,62</sup> In FT-IR, BNNSs show peaks at  $\sim 1340$  to  $1390$  and  $\sim 800$  to  $820 \text{ cm}^{-1}$  (Fig. 4c), corresponding to the B–N stretching and bending modes, respectively, also similar to h-BN.<sup>18,21,62</sup> The Raman signature for BNNSs is the peak typically found in the region of  $1366$ – $1373 \text{ cm}^{-1}$ , corresponding to the  $E_{2g}$  phonon mode of h-BN (similar to the G-band for graphene).<sup>17,18,20,21</sup> The  $E_{2g}$  peak of mechanically exfoliated monolayers and bilayers exhibited a small peak broadening with slight blue ( $+2$  to  $4 \text{ cm}^{-1}$ ) and red ( $-2 \text{ cm}^{-1}$ ) shifts in comparison to bulk h-BN, respectively (Fig. 4d).<sup>20</sup> However, it was suggested that the shift might be due to the small local strain induced by the substrate, making it

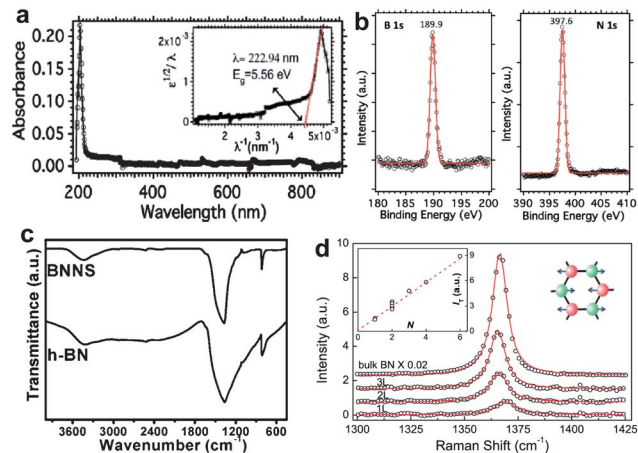


**Fig. 4** Spectroscopic signatures of BNNS. (a) Optical absorption spectrum of a CVD-grown few-layered BNNS sample on quartz showing high transmittance in the visible region and a bandgap peak at 203 nm. The inset shows that the bandgap wavelength was calculated to be 222.94 nm (or 5.56 eV) according to the Tauc equation.<sup>17</sup> (b) XPS spectra (Gaussian fitting shown in red) of B and N 1s core levels.<sup>17</sup> (c) FT-IR spectrum of an exfoliated BNNS sample compared to that of the bulk h-BN starting material.<sup>62</sup> (d) Raman spectra showing the  $E_{2g}$  peak of mechanically exfoliated BNNSs with 1–3 layers in comparison to that of the h-BN single crystal. The insets show (left) the dependence of spectral peak intensity ( $I_T$ ) on the layer number ( $N$ ) and (right) the phonon mode of the peak.<sup>20</sup> Reproduced with permission from ref. 17 (Copyright © 2010 American Chemical Society), ref. 62 (Copyright © 2011 Royal Society of Chemistry) and ref. 20 (Copyright © 2011 Wiley-VCH), respectively.

possibly sample and/or substrate dependent. A  $2.5\text{ cm}^{-1}$  blue shift was also found for the  $E_{2g}$  peak of CVD-grown few-layered BNNSs, which was also attributed to a substrate effect or the surface wrinkle-induced stress.<sup>17</sup> On the other hand, since the peak intensity notably decreased with smaller layer numbers, it could be a less ambiguous measure than peak position to determine the BNNS layer numbers given careful calibration.<sup>20</sup>

For defect identification purposes, Raman spectroscopy is much less useful for BNNSs (and BNNTs) than it has been for sp<sup>2</sup> carbon allotropes.<sup>50</sup> c-BN has significant phonon modes at  $1305$  (longitudinal; LO) and  $1055\text{ cm}^{-1}$  (transverse; TO), respectively, similar to the D-band for diamond.<sup>63</sup> However, unlike graphene and CNTs whose defective sp<sup>3</sup> carbon concentration can be semi-quantitatively measured by the D-band intensity, even for a highly defective h-BN sample the LO/TO bands were found to be absent, but only with a much weaker and broadened  $E_{2g}$  peak.<sup>53</sup> The lack of c-BN-like Raman modes is possibly due to the absence of dangling B and N atoms with sp<sup>3</sup> hybridizations in defective 2D BN nanostructures. Without a simple and dependable spectroscopic tool, defect density determination for BNNSs (and sp<sup>2</sup> BN materials in general) is so far much less straightforward as compared to sp<sup>2</sup> carbon allotropes. Nevertheless, similar to the Raman  $E_{2g}$  peak, the intensity of the characteristic (002) peak at  $26.7^\circ$  in X-ray diffraction (XRD) for h-BN and BNNSs<sup>18</sup> may decrease upon exfoliation and/or introduction of a significant amount of defects in the sample.<sup>53,64</sup> It is worth mentioning that the peak morphology in X-ray fluorescence spectra (XFS) was used for the identification of h-BN defects<sup>65</sup> but has yet to be applied to BNNSs.

### 3.3. Modulation of electronic and magnetic properties

Because of the large bandgap, BNNSs are excellent insulators in both lateral and through-thickness directions, with typical breakdown fields as high as  $1 \times 10^6\text{ V m}^{-1}$  as measured experimentally.<sup>66,67</sup> Theoretical investigations on the electronic bandgap and magnetic properties of 2D BN nanostructures have mostly focused on BNNRs despite the fact that there are only a couple of low-yield synthetic methods available (see Section 4.1.4.).<sup>58,68</sup> Like graphene nanoribbons (GNRs), BNNRs with either zigzag or armchair edges experience much enhanced quantum confinement from the edge effect with anisotropic electronic or magnetic properties that are not present in nanosheets of large lateral sizes. It should be noted that the edges of bare BNNRs are usually not quite thermodynamically stable and they are subject to reconstruction (a fact not considered in many reports).<sup>69,70</sup> Simple passivation (such as with hydrogen) could help minimize the edge formation energy.

Bandgaps of zigzag BNNRs are indirect and decrease monotonically with an increase of ribbon width, but the armchair configurations exhibit typical direct gap oscillation with distinct family behavior (Fig. 5).<sup>71–75</sup> However, bandgap tuning using nanoribbon width is rather limited (typically  $<30\%$ ). Various methodologies can be applied for much greater modulation. For example, as discussed previously in Section 2.2., introduction of either topographic or vacancy defects may induce significant bandgap reduction and modulation of magnetic properties of 2D BN nanostructures.<sup>41,44–47,76</sup> A recent study showed that these properties may also be conveniently modulated by introducing a “triwing” (*i.e.*, a branched sheet) in the BNNR to form a Y-shaped structure.<sup>77</sup>

Remarkable bandgap tuning of BNNRs might be achieved by the application of an external electric field (“Stark effect”).<sup>73,74,78</sup> The bandgap decrease may eventually lead to nanoribbons with metallic properties at a critical electric field. Despite variations in the stacking order and interlayer spacing, bilayer BNNRs may

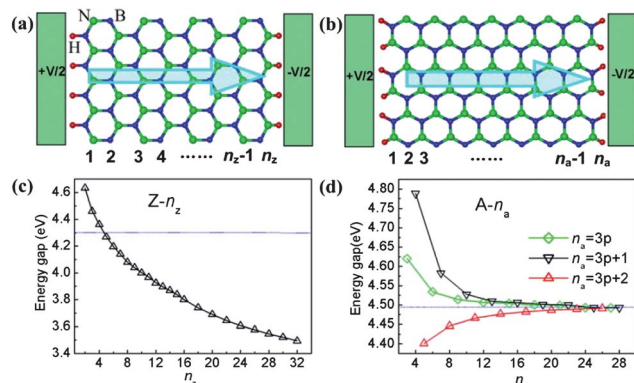


**Fig. 5** Electronic bandgap of zigzag and armchair BNNRs.<sup>73</sup> (a) and (b) are diagrams of the two types of BNNRs (edges passivated with H atoms) with widths of  $n_z = 8$  and  $n_a = 15$ , respectively. (c) and (d) are their bandgaps as functions of the widths, respectively. Dotted lines denote the energy gap of an isolated BNNS along the corresponding directions. P is a positive integer in (d). The arrows in (a) and (b) indicate the directions of the transverse electrical field across the width of the nanoribbons in further modulating their bandgaps. Reproduced with permission from ref. 73 (Copyright © 2008 American Physical Society).

also exhibit a strong Stark effect.<sup>79</sup> The bandgap of BNNRs or BNNSs could also be significantly reduced by the application of planar strain (accompanied with the increase of the lattice constant)<sup>80–82</sup> or by hydrostatic pressure in the GPa range.<sup>83</sup>

The bandgap modulations of BNNRs are often accompanied by a change in magnetic properties. While bare zigzag BNNRs were found to be magnetic semiconductors with spin-polarized states localized along the edges,<sup>84</sup> they may be turned into half-metals (*i.e.*, one electron spin being insulating and the other being metallic) *via* a directional external electric field.<sup>84,85</sup> Spin polarization with half metallicity is of great importance in spintronics applications.

Carbon doping of 2D BN nanostructures to form in-plane BNNS-graphene hybrids is one of the most investigated methods for bandgap and conductivity modulation. It will be discussed in more detail in Section 5.1. It is interesting to note here that half metallicity of zigzag BNNRs may be achieved *via* C termination at the nanoribbon edges.<sup>86,87</sup>

Hydrogen modification of BNNRs may also induce significant changes in electronic and magnetic properties. A common conclusion from several reports was that the consequences of modification on zigzag and armchair BNNRs are quite different. To be more specific, while hydrogen-modified armchair BNNRs remain nonmagnetic semiconductors, zigzag ribbons could display half-metallicity and become ferromagnetic metals with either hydrogen termination only at the B-edge<sup>88–93</sup> or full surface hydrogenation.<sup>94–96</sup> It was also shown that a gradual transition of a zigzag BNNR from a nonmagnetic semiconductor to a ferromagnetic metal might be achievable by controlling the degree of hydrogenation (Fig. 6).<sup>94</sup> A recent experimental study confirmed that it is possible to use hydrogenation for bandgap reduction of BNNSs.<sup>97</sup> Although the exact hydrogenation degree was not

reported, the measured bandgap of BNNSs was reduced from 5.6 eV to 4.25 eV after 250 s of hydrogen plasma treatment.

Some authors suggested that fluorine (F) termination could be a more plausible modulation route since B atoms are more electrophilic and may preferentially bind with F atoms.<sup>84</sup> This is consistent with more recent theoretical work by Zhang *et al.*, who found that full F coverage on surface B atoms occurred during fluorination of the outermost surfaces of few-layered BNNSs due to the high B–F binding energy.<sup>98</sup> Interestingly, the hexagonal structure spontaneously transforms into a cubic (diamond-like) structure with F moieties remaining at the outer surfaces, and the final fluorinated product exhibits a significantly reduced bandgap. In a related report, zigzag BNNRs could be transformed into robust half metals with 2 F terminations at B-edges and 1 F termination at N-edges regardless of ribbon width.<sup>99</sup>

It has been recently suggested that carrier doping could be used to control the sites of functionalization (such as hydrogenation and fluorination) being primarily at B or N atoms.<sup>100</sup> This may offer an interesting route to further fine-tune the electronic and magnetic properties of covalently functionalized BNNSs/BNNRs.

Many other covalent modification schemes can also be useful for electronic and magnetic modulation of the 2D BN nanostructures. For example, zigzag BNNRs may turn metallic with either O- or S-termination.<sup>101</sup> However, only O-termination yielded ferromagnetism at a B-edge, while S-terminated nanoribbons remained nonmagnetic. Various other functional moieties attached to the edge (*e.g.* Cl, NO<sub>2</sub> and OH)<sup>102,103</sup> or the basal plane (*e.g.* OH, CH<sub>3</sub>, CHO, CN, NH<sub>2</sub>)<sup>104</sup> may also induce notable bandgap reductions.

Compared to zigzag BNNRs, the electronic and magnetic properties of armchair BNNRs are usually much more robust against modification. However, it was reported that they can be transformed into half metal *via* termination of various transition metal atoms such as Fe, Mn, or Co.<sup>105</sup> Armchair nanoribbons with other metal atom terminations such as Cr, Ni, or Cu remain semiconductors but with different magnetic states.<sup>105</sup>

Many noncovalent functionalization strategies, such as those with polar organic molecules<sup>106</sup> or metal–arene complexes (also see Section 4.1.3.),<sup>107</sup> could also result in bandgap reduction of BNNSs and sometimes also induce spin polarization.

### 3.4. Thermal conductivity

Despite discrepancies in the actual numbers predicted under different models,<sup>108–111</sup> the consensus is that the 2D BN nanostructures are excellent thermal conductors although they are electrically insulating. The calculated thermal conductivity ( $\kappa$ ) values for BNNSs range from 300–2000 W m<sup>-1</sup> K<sup>-1</sup> and are somewhat lower than graphene (1500–2500 W m<sup>-1</sup> K<sup>-1</sup>). This difference may be due to softer phonon modes for BNNSs and the mass difference between B and N.<sup>109</sup> It was suggested that a monolayer BNNS would have a higher  $\kappa$  value than few-layered ones due to reduced interlayer phonon scattering. The  $\kappa$  value decreases with increasing layer number eventually converging to the value of h-BN.<sup>110,111</sup> BNNRs exhibit edge-induced phonon scattering and thus smaller  $\kappa$  values than nanosheets with infinite sizes.<sup>109</sup> As is with GNRs, the different extent of the scattering

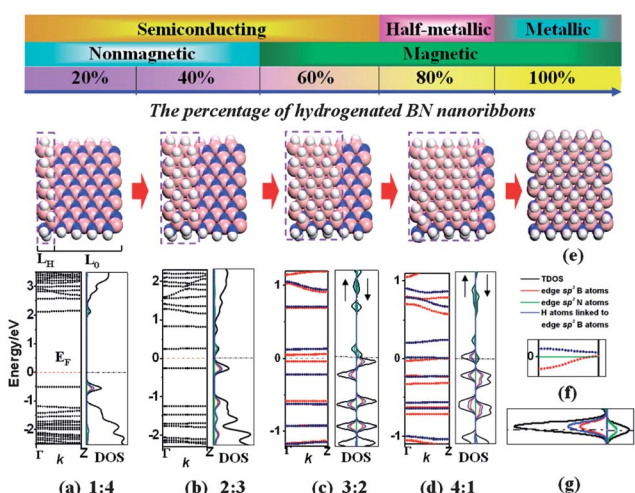


**Fig. 6** Modulation of electronic and magnetic properties of zigzag BNNRs *via* hydrogenation.<sup>94</sup>  $L_H$  and  $L_0$  are respective unit numbers of hydrogenated and pristine BNNR blocks. The hydrogenation degrees from left to right are (a) 20% ( $L_H : L_0 = 1 : 4$ ), (b) 40% (2 : 3), (c) 60% (3 : 2), (d) 80% (4 : 1), and (e) 100%, respectively. The blue and red lines in (c) and (d) denote the spin-up ( $\uparrow$ ) and spin-down ( $\downarrow$ ) channels, respectively. (f) and (g) zoom in on the regions of the Fermi level of the band structure and density of states of (d), respectively. Reproduced with permission from ref. 94 (Copyright © 2010 American Chemical Society).

effect of zigzag and armchair BNNRs makes the thermal conductivity of the former considerably higher than the latter.

Experimental data from direct measurements of  $\kappa$  values of 2D BN nanostructures are rare to date. We reported an in-plane value of  $\sim 40 \text{ W m}^{-1} \text{ K}^{-1}$  for a bulk BNNS sample facially settled on a filter membrane by filtering an aqueously dispersed BNNS sample.<sup>21</sup> Because of the small BNNS lateral sizes ( $1 \mu\text{m}$  or less), this value is obviously far off from the true  $\kappa$  for an individual monolayer BNNS because of the significant phonon scattering within the bulk sample. No experimental  $\kappa$  data for a monolayer BNNS are yet available at the time of this review. Nevertheless, significant thermal conductivity enhancement of polymer composites with BNNS fillers was reported<sup>112,113</sup> and will be discussed in more detail in Section 6.1.

### 3.5. Mechanical properties

Defect-free monolayer graphene is the strongest material known.<sup>114</sup> It was predicted that the structural similarity of BNNSs to graphene makes them almost equally strong and much stronger than other 2D materials.<sup>12,115–118</sup> In one study, the in-plane stiffness values of a monolayer BNNS and graphene were calculated to be 267 and  $335 \text{ N m}^{-1}$ , respectively.<sup>116</sup> Therefore, like graphene, BNNSs can be excellent reinforcing fillers for polymer composites, which will be discussed in a later section.

Song *et al.* used a nanoindentation method (the same method used for graphene evaluation<sup>114</sup>) to directly assess the mechanical performance of few-layered BNNSs grown from a CVD process.<sup>17</sup> The nanosheets were very flexible, with deflections of  $\sim 70 \text{ nm}$  before they were broken by the diamond indentation tip. It was shown that the modulus and breaking stress of BNNSs with thicknesses of 1–2 nm were in the range of  $220\text{--}510 \text{ N m}^{-1}$  and  $8\text{--}16 \text{ N m}^{-1}$ , respectively. Considering the multilayer nature of the nanosheets, these values were somewhat lower than expected. The authors attributed the less-than-ideal mechanical performance of BNNSs to the presence of intrinsic vacancy defects arising from the CVD growth. Indeed, simulations showed that both modulus and breaking strength of BNNSs decreased with the vacancy concentrations.<sup>17</sup>

In a study on BNNSs from sonication-assisted solvent-exfoliation (thicknesses  $\sim 25$  to  $300 \text{ nm}$ ), Li *et al.* found that the bending modulus of the nanosheets increased with reduced thickness.<sup>119</sup> The authors attributed this observation to the defect-induced stacking faults between nanosheet layers resulting from the exfoliation process.

Also interesting is the friction or tribological properties of BNNSs, which have appeared to be qualitatively similar to many other 2D nanomaterials. It is well known that bulk graphite and h-BN are widely used lubricant materials. The lubrication is due to the weak forces holding the adjacent basal planes in their structures, with external shear resulting in the sliding of the layers. At the level of a few layers of atomic sheets, a friction force microscopy study suggested that the frictional characteristics of few-layered graphene and BNNSs, as well as those of some other 2D nanomaterials such as MoS<sub>2</sub> and NbSe<sub>2</sub>, are thickness dependent.<sup>120</sup> The thinner nanosheets exhibited higher frictions due to increased susceptibility to out-of-plane deformation. More recently, it has been further shown that the friction force may induce reversible dynamic wrinkling on the most top

layer for various types of nanosheets such as graphene, BNNSs, and MoS<sub>2</sub>.<sup>121</sup>

## 4. Preparation

BNNSs can be obtained *via* top-down or bottom-up approaches, which mostly refer to the exfoliation of h-BN or synthesis from B and N precursors, respectively. Most methods have their unique advantages for specific targeted applications but often there are shortcomings as well. BNNSs from exfoliation methods are usually highly crystalline, but the lateral sizes are limited by those of the h-BN starting material. Also, the strong lip–lip interactions between layers make it difficult to achieve complete or high degrees of exfoliation. Consequently, the products typically contain only a small fraction of monolayers. In comparison, CVD methods as representative bottom-up approaches are very useful in the controlled preparation of thin BNNSs of large lateral sizes. However, the crystallinity is typically less than that obtained from exfoliation methods. Below, we discuss in detail these two categories of methods for BNNS preparation along with some potential applications. BNNRs and BNNMs, two special classes of 2D BN nanostructures, will also be discussed in the context of their preparation methodologies (BNNT unzipping and CVD, respectively).

### 4.1. Top-down methods

**4.1.1. Mechanical cleavage.** The simple adhesive tape peeling approach, now famously known as “the Scotch tape method” or the micromechanical cleavage method, enabled the isolation and characterization of monolayer graphene.<sup>5</sup> After their initial discovery, Novoselov *et al.* soon successfully applied the same isolation method to many other layered compounds including NbSe<sub>2</sub>, MoS<sub>2</sub>, Bi<sub>2</sub>Sr<sub>2</sub>CaCu<sub>2</sub>O<sub>x</sub>, and h-BN.<sup>6</sup> In this process, BNNSs could be obtained by peeling the adhesive tape from a starting h-BN sample and pressing onto a targeted substrate. Repeating the peeling–pressing process of the initially obtained particles rendered more exfoliated nanosheets down to a monolayer level. This approach has enabled a number of authors to obtain thin BNNSs for detailed structural studies.<sup>13,20,28–30</sup>

Exfoliated BNNSs thus obtained retain their original lateral sizes and the low defect density as of the parent h-BN crystal. Nanosheets obtained in this manner have the best combination of thicknesses and lateral sizes, making them ideal for fundamental studies in physics and electronics. However, this technique is less effective to isolate few-layered and monolayer BNNSs than graphene, partially because of the stronger lip–lip interactions between BN basal planes. In addition, compared to natural graphite crystals which easily reach several hundred micrometers or more in lateral sizes, most current commercially available h-BN powdery materials contain microcrystals with lateral dimensions only from a few to tens of micrometers. Large single crystals of h-BN have recently been prepared but are not yet widely available in large quantities.<sup>54–56</sup> Nevertheless, micromechanical cleavage from these h-BN crystals provided much better success in obtaining large area few-layered and monolayer BNNSs with lateral sizes over 100 micrometers (Fig. 1g and h).<sup>20</sup> This is comparable to graphene nanosheets obtained by a similar approach.

Compared to other exfoliation methods and bottom-up synthetic approaches, the Scotch tape method is perhaps the least scalable. There have been reports of mechanical cleavage methods to produce BNNSs on a much larger scale. Instead of the direct peeling forces applied in the Scotch tape method, these methods used shear forces from scalable mechanical processes.<sup>122–124</sup> Traditional ball-milling methods are quite aggressive and non-selective, yielding h-BN products with a significant number of defects.<sup>53,125–127</sup> Li *et al.* reported a mild wet ball-milling process that yields few-layered crystalline BNNSs with slight lateral size reduction (Fig. 7a).<sup>122</sup> The authors concluded that the use of a planetary mill instead of more aggressive high-energy mills was critical since the former allowed the rolling motions of the balls, thereby applying predominantly shear force to the h-BN microcrystals. It was also important to use a large number of small-sized balls and, in particular, to add a lubrication solvent. Benzyl benzoate as the lubricant in the wet process provided better exfoliation results than water, ethanol, and dodecane. This was attributed to the high viscosity and the similarity in surface tension of the solvent and the h-BN (conforming to the Hansen–Coleman model, see the next section).

Using a vortex fluidic device setup, Chen *et al.* rotated a small amount of h-BN suspension in *N*-methyl-2-pyrrolidinone (NMP) at 8000 rpm in a glass tube with a fixed-angle (45° being optimal) resulting in significant exfoliation (Fig. 7b).<sup>123</sup> It was suggested that the fluid formed a thin layer on the inner wall of the centrifuge tube at the given angle and speed and provided a shear force to partially lift the layers. This was followed by layer slippage and exfoliation. This method was equally applicable to the exfoliation of graphite. With a similar merit, few-layered BNNSs were obtained in a high pressure microfluidization process which was suggested to be potentially industrially scalable due to the continuous flow setup.<sup>124</sup> In this process, starting h-BN powder was simply added to a polar organic solvent [*N,N'*-dimethylformamide (DMF) : chloroform = 6 : 1] and pumped

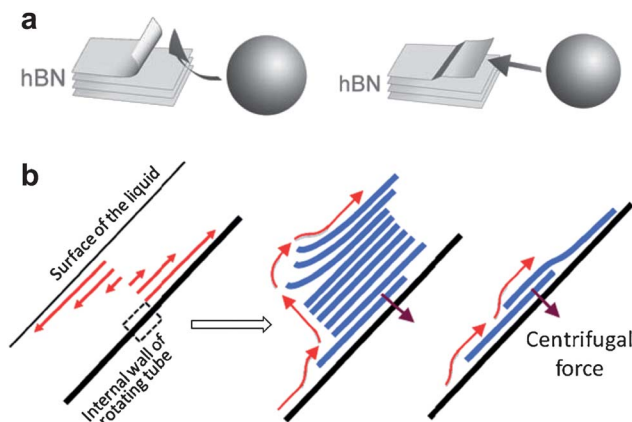


**Fig. 7** Scalable mechanical exfoliation approaches for BNNSs: (a) low-energy ball-milling:<sup>122</sup> cartoons illustrate the colliding (left) and sliding motions (right) of balls on h-BN layers, inducing shear forces that lead to exfoliation; (b) vortex fluid exfoliation:<sup>123</sup> fluid dynamics suggests upward liquid flow near the inner wall of the rotating tube (left), which resulted in shear forces that led to the exfoliation of h-BN microcrystals at the tube wall by partial lifting (middle) or direct slippage (right). Reproduced with permission from ref. 122 (Copyright © 2011 Royal Society of Chemistry) and ref. 123 (Copyright © 2012 Royal Society of Chemistry), respectively.

through a microfluidic processor at a pressure as high as 207 MPa with multiple circulations. The authors suggested that such high pressure in the microfluidic channel generated a large shear force, which resulted in the exfoliation of h-BN microcrystals into nanosheets in just a few minutes. A large quantity of few-layered BNNSs in a stable dispersion was obtained. No sonication was involved.

**4.1.2. Sonication-assisted direct solvent exfoliation.** The use of surfactants to disperse nanomaterials is common and has been experimented with for exfoliation and dispersion of BNNSs.<sup>128</sup> More interestingly, without the use of surfactants or functional groups, effective exfoliation of h-BN could be achieved just by sonication of the starting material in many common solvents.

**Organic solvents.** Zhi *et al.* first reported a simple process in which h-BN was sonicated in DMF to give few-layered BNNSs with retained crystallinity but somewhat reduced lateral sizes.<sup>15</sup> The authors attributed the exfoliation to the strong interactions between the locally polarized BN sheet surface and the polar solvent DMF. Spectroscopic evidence and theoretical calculations from a more recent report<sup>129</sup> suggest that the polar solvent–nanosheet interactions were between the oxygen atoms of the carbonyl group and the boron atoms on BNNSs, similar to the Lewis acid–base interactions that will be discussed in the next section.

The simple solvent exfoliation and dispersion of BNNSs is not restricted to DMF. For example, our results showed that many other strong polar organic solvents, such as NMP, *N,N'*-dimethylacetamide (DMAc), 1,2-dichlorobenzene, and ethylene glycol, among others, are effective in exfoliating h-BN with sonication to yield stable BNNS dispersions. In contrast, many non-polar solvents such as toluene and hexanes were ineffective (Fig. 8).<sup>130</sup>

Following their dispersion efforts on single-walled carbon nanotubes (SWNTs)<sup>131</sup> and graphene,<sup>60</sup> Coleman and



**Fig. 8** (a) Pictures of direct organic dispersions of BNNSs from simple bath sonication right after preparation. The solvents from left to right are: NMP, *N,N'*-dimethylacetamide (DMAc), 1,2-dichlorobenzene (DCB), DMF, ethylene glycol (EthGly), ethanol (EtOH), IPA (isopropanol), acetone, tetrahydrofuran (THF), chloroform (CHCl<sub>3</sub>), ethyl acetate (EtAc), methanol (MeOH), dimethyl sulfoxide (DMSO), toluene, and hexanes. (b) The same dispersions were irradiated with a laser beam from the left side of each vial to visually indicate the Tyndall effect (more intense reflection suggesting a higher concentration). (c) Pictures were taken after ~1 week (day 7–9).

co-workers attempted to use the Hansen solubility parameter theory to explain and guide the direct solvent dispersion of various 2D inorganic nanosheets, including BNNSs and many metal chalcogenides such as MoS<sub>2</sub> and WS<sub>2</sub>.<sup>7</sup> Within this theoretical framework (herein called “the Hansen–Coleman model”), good solvents (or solvent mixtures) for directly dispersing nanosheets should be those that minimize the enthalpy of mixing and thus the energy of exfoliation. In other words, the solvent used should have a similar surface energy to the nanosheets. Survey of various organic solvents suggested that effective solvents for BNNSs have surface energies of around 65 mJ m<sup>-2</sup> (Fig. 9), with isopropanol (IPA) and NMP among the best. In fact, MoS<sub>2</sub>, WS<sub>2</sub> as well as SWNTs and graphene could all be effectively dispersed in solvents with surface energies close to 70 mJ m<sup>-2</sup> (or surface tension ~40 mJ m<sup>-2</sup>). The authors attributed the similarities in the solvent effectiveness for the different types of materials to the common van der Waals forces that the exfoliation processes needed to overcome.

The Hansen–Coleman model has been validated in a majority of experimental observations in the literature. Using this guidance, Zhou *et al.* proposed a mixed-solvent strategy in which

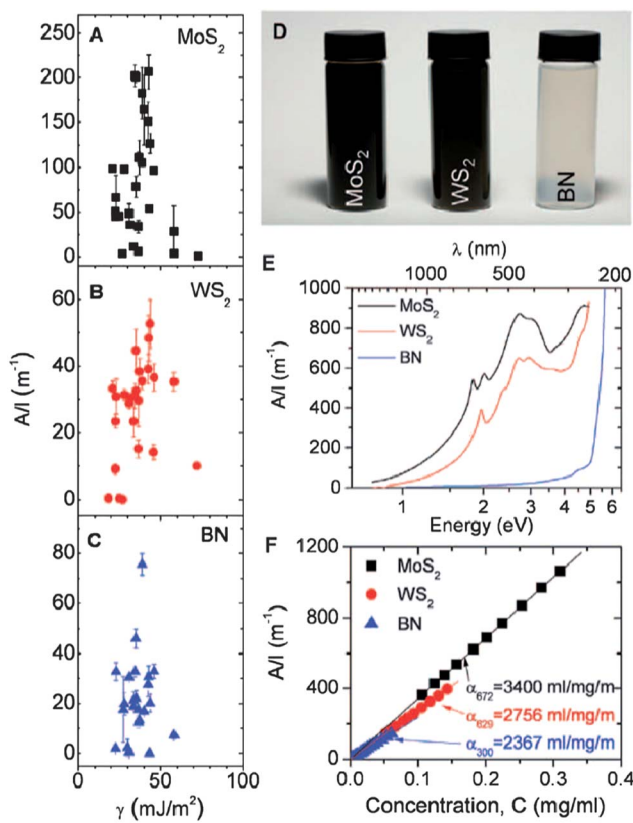


**Fig. 9** Preparation of organic dispersions of exfoliated inorganic nanosheets using guidance from the Hansen–Coleman model.<sup>7</sup> (A–C) Concentration remaining after centrifugation (plotted as absorbance per length, A/l) for nanosheets of MoS<sub>2</sub>, WS<sub>2</sub>, and BN dispersed in different solvents with various surface tension ( $\gamma$ ). Also shown are (D) photographs, (E) absorbance spectra, and (F) Lambert–Beer plots for dispersions of nanosheets of MoS<sub>2</sub> in NMP, WS<sub>2</sub> in NMP, and BN in IPA. Reproduced with permission from ref. 7 (Copyright © 2011 American Association for the Advancement of Science).

ethanol–water mixtures showed improved dispersion and exfoliation for h-BN, MoS<sub>2</sub> and WS<sub>2</sub> in comparison to the use of individual solvents.<sup>132</sup>

Some solvents that deviate from this model usually interact with the nanomaterials much more strongly or even react chemically. For example, both water<sup>21</sup> and methanesulfonic acid (MSA)<sup>133</sup> have much higher surface energies than typical polar organic solvents but are effective for dispersion and exfoliation of BNNSs, which are discussed separately below.

**Water.** Carbon nanomaterials are insoluble in water unless significant oxygen-containing functional groups are created (*via* oxidative treatment, for example).<sup>50,134</sup> Comparably, BN materials are only slightly less hydrophobic,<sup>135,136</sup> while physical models suggest that water does not wet h-BN at room temperature.<sup>137</sup> Therefore, it seems somewhat counter-intuitive that dispersions of exfoliated BNNSs could be obtained by simply sonicating h-BN in water. We found that the solubilization efficiency using water for BNNSs was quite high (up to ~0.2 mg mL<sup>-1</sup> in an as-prepared dispersion), comparable to the good polar organic solvents such as DMF.<sup>21</sup> Interestingly, compared to those solvents, aqueous BNNS dispersions contained a higher fraction (~20%) of thin (down to monolayer) and small (<200 nm) nanosheets.

It was shown several decades ago that borazine, the B–N equivalent of benzene and the unit of h-BN, was reactive under hydrolysis conditions, yielding boron oxide with ammonia evolution.<sup>138</sup> It was thus proposed that, in addition to the solvent–BN polar interactions, sonication-assisted hydrolysis of h-BN sheets also contributed in the exfoliation. The unusual presence of a high fraction of thin and small sheets (“cutting”) indicated that hydrolysis did play a significant role in exfoliation (Fig. 10). Further evidence that supported this hypothesis included a positive test for dissolved ammonia and the presence of hydroxyl groups in the final BNNS product. The latter observation provided a rational explanation for the stable dispersion of BNNSs in water.

Without any added functional groups or surfactants, these aqueously dispersed BNNSs are “impurity-free” and thus available for further modification. For example, these nanosheets

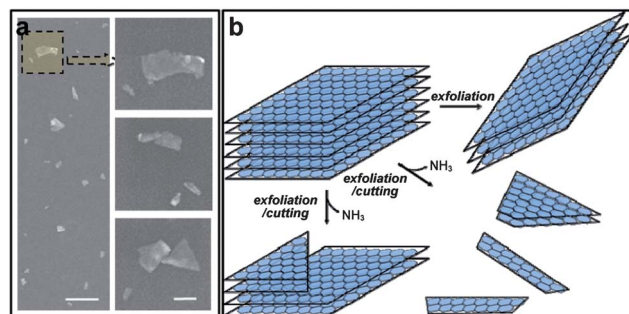


**Fig. 10** Water for exfoliation and cutting of h-BN.<sup>21</sup> (a) SEM images showing BNNSs with mostly sub-100 nm lateral sizes obtained with centrifugation of an aqueous BNNS dispersion at 20 800 × g. Scale bars = 200 nm (left) and 50 nm (right). (b) A cartoon of the exfoliation and cutting process, the latter of which is the result from sonication-induced hydrolysis and thus accompanied with ammonia release.

have been decorated with ferritin proteins<sup>21</sup> and Ag nanoparticles (see more discussions in Section 6.2.).<sup>57</sup> The aqueous dispersibility of BNNSs and their capability to conjugate with biomolecules are obviously attractive biologically since the BN compounds are usually considered non-toxic and thus biocompatible.

**Acid.** The stability of the above aqueous BNNS dispersion was not affected by the addition of strong base solutions; however, the addition of acid resulted in sedimentation within hours.<sup>21</sup> Inspired by the successful dispersion of rod-like polymers, CNTs and graphene, Wang *et al.* used MSA, a rather strong protic acid, to obtain exfoliated BNNS dispersions *via* sonication.<sup>133</sup> The solubility reached  $\sim 0.3 \text{ mg mL}^{-1}$ , comparable with water and the good organic solvents discussed above. The authors suggested that, similar to previous systems, MSA also protonated BNNS edges and surfaces during the process, resulting in the repulsion forces between adjacent layers leading to exfoliation. This is in a way similar to the electrostatic dispersion of monolayer graphene oxide prepared by Hummer's method.<sup>134</sup> Their hypothesis was supported by the orange color of the MSA-dispersed BNNSs, which could be the result of charge transfer between the acid molecules and the nanosheets. The color disappeared when the nanosheets were redispersed into organic solvents (*e.g.* NMP); those dispersions took on the common "milky" appearance. Spectroscopic investigations suggested that B–N bonds did not undergo oxidation with MSA as no additional oxygen containing groups were evident in FT-IR and no spectral broadening of B and N signals were observed in XPS.<sup>133</sup>

**4.1.3. Chemical functionalization.** Chemical functionalization has proven to be an effective way to exfoliate CNT<sup>50</sup> and BNNT bundles<sup>3,139</sup> as well as graphite<sup>134</sup> by overcoming the van der Waals forces that hold the unit entities (*i.e.*, individual CNTs/BNNTs and graphene layers) together. In a similar fashion, functionalization methods are quite effective in overcoming the lip–lip interactions among the layers of h-BN to achieve exfoliation.

The functionalization approaches may be roughly divided into noncovalent, Lewis acid–base (ionic), and covalent categories. Generally, bulky organic moieties are attached to the outermost h-BN crystal surface and perhaps also intercalate between the layers. When the functionalized h-BN is placed in a solvent either during or after a reaction, the solvation force induced by the attached functional groups is sufficient to overcome the van der Waals forces that hold the layers to the parent crystal. Exfoliated BNNSs can then give dispersions in organic solvents or water, depending upon the functional groups attached.

Before discussing different functionalization approaches in detail, it should be clarified that BN polymorphs (including BNNTs and BNNSs) are sometimes misleadingly described as "chemically inert". This is inaccurate because BNNSs and other hexagonal BN polymorphs such as BNNTs are actually quite ionically active due to the locally polarized B–N bonds. Instead, the "inertness" should refer to their excellent resistance against wet and air oxidation.

Strong solution oxidation approaches such as Hummer's method and its variations have been popularly used to synthesize dispersed monolayer graphene sheets (in the form of graphene

oxide) and are thus of central importance in graphene chemistry and related applications.<sup>134</sup> However, the inertness of h-BN against wet oxidation techniques has prevented the preparation of BNNSs *via* similar intensive oxidation approaches.

h-BN and BNNSs do not oxidize unless they are heated above *ca.* 800 °C in air. Such inertness was also implied theoretically: the desorption of molecular oxygen from a monolayer BNNS is much more favorable than the formation of oxidation products.<sup>140</sup> Nevertheless, during the air oxidation of BN polymorphs at high temperature, oxygen atoms gradually and irreversibly replace the nitrogen atoms in the BN lattice.<sup>141</sup> This eventually yields B<sub>2</sub>O<sub>3</sub> and N<sub>2</sub> is evolved, resulting in a weight increase (from solid BN to solid B<sub>2</sub>O<sub>3</sub>) that can be conveniently quantified *via* thermogravimetric analysis (TGA).

**Noncovalent functionalization.** In a pioneering study, Han *et al.* obtained exfoliated BNNSs by sonicating a h-BN single-crystal sample in a dichloroethane solution of a conjugated polymer, poly(*m*-phenylenevinylene-*co*-2,5-dioxy-*p*-phenylenevinylene).<sup>14</sup> Such polymers have been well-known to noncovalently functionalize and exfoliate CNTs,<sup>50</sup> graphene<sup>134</sup> and BNNTs,<sup>142</sup> and could generate GNRs in a similar sonication-assisted procedure.<sup>143</sup> Although the mechanism was not discussed in much detail, the exfoliation is likely due to noncovalent functionalization *via*  $\pi$ – $\pi$ -like interactions between the conjugated polymer and the h-BN surface.

There have been several theoretical reports on the noncovalent interactions between BNNSs and various functional molecules that contain planar or aromatic moieties.<sup>106,107,144,145</sup> The general observation has been that the polarity of the functional molecule plays an important role in its optimal orientation on the BNNSs. In one example, both an electron acceptor (tetracyanoquinodimethane, TNCQ) and a donor (tetraphiafulvalene, TTF) were noncovalently stacked on BNNSs or BNNRs.<sup>106</sup> The optimized functional molecule–nanosheet distances (3.3–3.7 Å) were equivalent to or slightly larger than the typical BN layer distance. The lowest energy molecular orientation was governed by the electrostatic interactions between the functional molecules and the nanosheet surface. Similarly, transition metal–arene complexes (MC<sub>6</sub>H<sub>6</sub>, M = Ti, V, Cr, Mn, Fe, and Co) were predicted to noncovalently stack on the BNNS surface, with the most stable configuration being one with the metal atoms above the centers of borazine rings.<sup>107</sup> After functionalization, bandgap reduction and spin polarization of BNNSs were observed. In addition, the reactivity of the nanosheets was improved, as demonstrated by enhanced adsorption of oxygen molecules.

In an *ab initio* study, Duan and coworkers predicted that the five nucleobases [guanine (G), adenine (A), thymine (T), cytosine (C), and uracil (U)] prefer to interact facially with BNNSs (rather than attach perpendicularly) with essentially the same stacking order.<sup>144</sup> In optimized configurations, the N and O atoms of nucleobases are located above the B atoms of the nanosheets (Fig. 11) despite somewhat varied adsorption energies (0.5–0.7 eV) (in the order of G > A > T > C > U). Because of the ionic characteristics, the noncovalent interactions between nucleobases and BNNSs are stronger than the  $\pi$ – $\pi$  interactions between similar molecules and CNTs<sup>50,134</sup> or graphene.<sup>146</sup> It is expected that assembly of DNAs and RNAs on BNNSs could

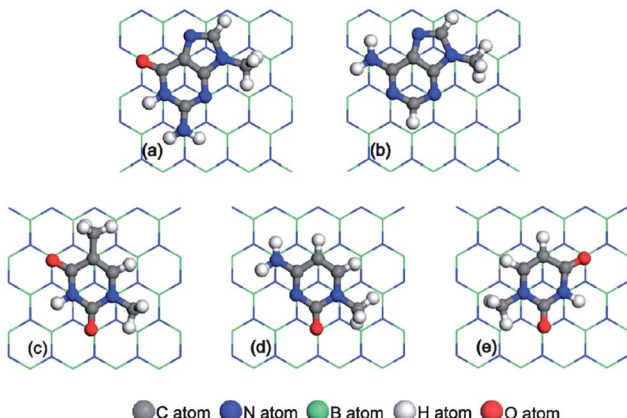


**Fig. 11** Optimized configurations of the five nucleobases adsorbed on a BNNS.<sup>144</sup> (a) guanine (G), (b) adenine (A), (c) thymine (T), (d) cytosine (C) and (e) uracil (U). Reproduced with permission from ref. 144 (Copyright © 2011 Royal Society of Chemistry).

soon be observed experimentally, pointing toward exciting biological applications.

**Lewis acid–base complexation.** The locally polarized B–N bonds allow convenient targeting of either B or N atoms for Lewis acid–base interactions. Strictly speaking, such complexations are also noncovalent in nature – but with strong ionic (electrostatic) characteristics. Electrophilic attack at the N atoms on BNNSs should be possible but no experimental reports are available to date. Inspired by the successful attempts on BNNTs,<sup>139</sup> there have been several reports on attaching functional groups to the B atoms on BNNSs.<sup>16,53,112,147</sup> Mechanistically, the electron deficient B atoms possess Lewis acid characteristics and are susceptible to the attack by Lewis base compounds (such as amines and phosphines) to form stable Lewis acid–base complexes.

We demonstrated that Lewis acid–base adducts could be formed between B atoms on the h-BN surface and the amino groups of octadecylamine (ODA) or an amine-terminated oligomeric polyethylene glycol (PEG) (Fig. 12).<sup>16</sup> The long lipophilic and hydrophilic “tails” of ODA and PEG could both effectively functionalize the surface of the h-BN microcrystals (commercially available powder) in melt reactions. The functional molecules intercalated into and exfoliated the h-BN layers, resulting in ODA–BNNS and PEG–BNNS adducts that could be extracted using organic solvents (in the case of ODA) or water (in the case of PEG). Similar to solvent dispersions discussed in the previous section, these functionalized and exfoliated BNNS dispersions also appeared transparent at low concentrations (see Fig. 3c) yet “milky” at higher concentrations, and were stable over several months. The BNNSs were mostly few-layered, with thicknesses in the range of 1–7 nm (or 3–20 layers) and lateral sizes in the range of a few hundreds of nanometers to over 1 μm. There was also evidence of monolayer BNNSs, but they were either of small lateral size (<100 nm) or found at the edge of a larger exfoliated nanosheet.

In a similar attempt, Nag *et al.* showed that trioctylamine and trioctylphosphine can also form soluble adducts with few-layered

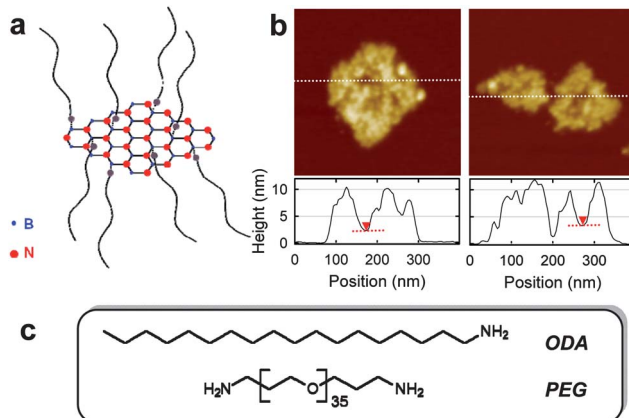


**Fig. 12** Lewis base complexation and exfoliation of h-BN.<sup>16</sup> (a) A cartoon diagram of functionalized BNNS with amine moieties of the functional groups attached to the surface B atoms. (b) AFM images (dimensions 400 nm × 400 nm) of PEG-functionalized few-layered BNNSs and the corresponding height profiles. The amorphous materials, likely PEG functional groups, covered most of the nanosheet surfaces. (c) Structures of ODA and PEG molecules used in the reactions.

BNNSs *via* simple sonication of the bottom-up grown nanosheets in solutions containing the functional molecules.<sup>147</sup>

The efficiency of functionalization and solubilization of BNNSs *via* Lewis acid–base complexation could be improved by the presence of defects on starting h-BN (also see Section 2.2.). We reported the use of ball-milling to introduce defects on pristine h-BN particles.<sup>53</sup> The increase in defects was confirmed by much broader and weaker (002) and  $E_{2g}$  peaks in XRD and Raman, respectively. The data indicated the presence of increased stacking faults as a result of large amounts of vacancies and edges. The same melt functionalization reaction using ODA as the functional molecule followed by solvent extraction resulted in a much higher uptake of starting h-BN (*e.g.* ~40% solubilized for a h-BN sample after 60 min ball-milling *vs.* ~10% for pristine h-BN). The solubilized 2D BN nanostructures included not only smaller and thinner BNNSs, but also highly defective multicrystalline particles that consisted of multiple hexagonal phases that were buckled and tangled together by the aggressive ball-milling process.

The nature of amine-B attachment in the Lewis acid–base complexation schemes was strongly supported by nuclear magnetic resonance (NMR) spectroscopic results (Fig. 13).<sup>16,53,112</sup> For example, compared to the unchanged alkyl-end “tail” C–H signals, the amino-end “head” signals in the ODA structure diminished after attachment onto BNNSs (Fig. 13b).<sup>16,112</sup> Similar phenomena have been commonly seen in the functionalization of other nanostructures (such as CNTs<sup>50</sup>) and were attributed to the limited mobility of the functional end of the molecule in the solution induced by its attachment to a large entity – in this case a BNNS. It was quite interesting that, with highly defective h-BN starting materials, the same “head” C–H signals of the ODA functional group in NMR shifted to new positions instead of simply diminishing while other signals remained unaffected (Fig. 13c).<sup>53</sup> This result suggested that it was still the amino end of the ODA molecules that was attached to the B atoms of the defective BNNSs in a Lewis acid–base interaction scenario.

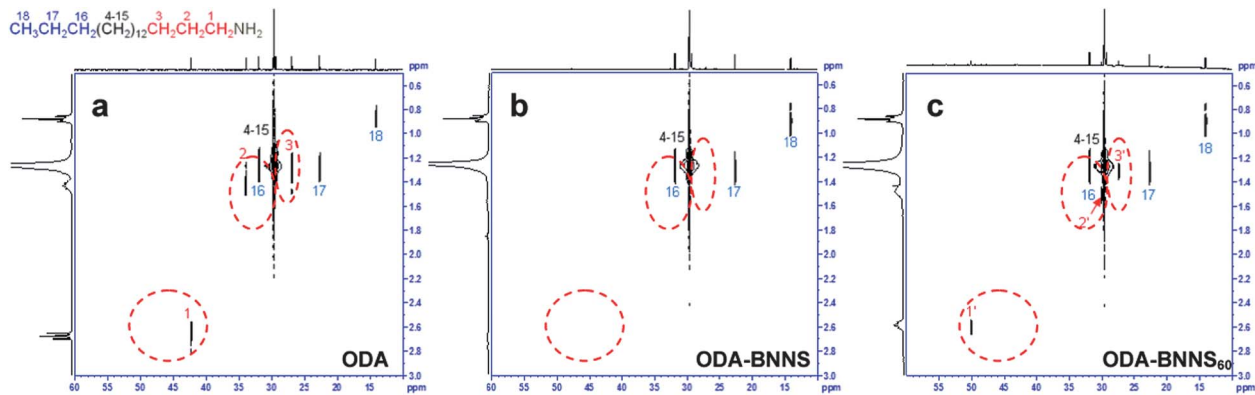


**Fig. 13** 2D <sup>13</sup>C{<sup>1</sup>H} HETCOR NMR spectra ( $\text{CDCl}_3$ , room temperature) of (a) ODA, and ODA-functionalized BNNSs from (b) non-treated h-BN and (c) defective h-BN that had been ball-milled for 60 min (“BNNS<sub>60</sub>”).<sup>16,53</sup> The corresponding <sup>1</sup>H and <sup>13</sup>C NMR spectra (acquired separately) were placed in the vertical and horizontal projections, respectively. Spectral assignments to individual C–H pairs of the ODA molecule are shown. The dashed red circles highlight the changes before and after functionalization. The three “head” C–H pair signals diminished with non-treated h-BN but shifted with defective h-BN.

However, such attachments were somehow surprisingly regular in terms of the chemical environment that affected the NMR shifts, which have yet to be mechanistically elucidated.

It is foreseeable that, by tailoring the bulky group of the Lewis base, such facile chemistry for h-BN functionalization and exfoliation could potentially be very straightforward and versatile. Different oligomeric, polymeric or bio-inspired molecules with Lewis base characteristics (*i.e.*, with amines or other nucleophilic moieties) may be conveniently used to obtain functionalized and exfoliated BNNSs for a variety of targeted applications.

**Covalent functionalization.** Direct covalent functionalization of a BNNS basal plane is yet to be reported at the time of this review. Alternatively, functional groups can be covalently attached to hydroxyl groups at the nanosheet edges of certain h-BN starting materials, as reported by Yu *et al.*<sup>112</sup> In this work,  $\gamma$ -aminopropyl-triethoxysilane was attached to the hydroxyl groups to obtain h-BN with amino moieties at the edges, which was subsequently linked to a hyperbranched aromatic polyamide.<sup>112</sup> The authors incorporated into an epoxy matrix unfunctionalized h-BN or nanosheets with either ODA (in terms of Lewis acid–base complexation) or covalently attached polyamide functionalities. The improved filler–matrix interactions in the composites with functionalized BNNSs resulted in improved dispersion within the matrix and performance enhancement in thermal degradation temperature, thermal conductivity, glass transition temperature, and elastic modulus (also see Section 6.1.).<sup>112</sup>

**4.1.4. BNNRs from BNNT unzipping.** As discussed in Section 3.3., BNNRs as a special category of BNNSs are of particular fundamental interest because of the edge effect and have many potential applications in electronics and spintronics. However, the preparation of such high aspect ratio nanosheets with narrow widths is quite challenging. To date, only a couple of approaches that use BNNTs as the starting material (thus also “top-down”) are currently available.<sup>58,68</sup> Both methods were inspired by previously discovered GNR preparations.

Zeng *et al.* first reported the use of controlled Ar plasma etching,<sup>58</sup> previously used by Dai and co-workers for GNRs from multi-walled CNTs,<sup>148</sup> to produce BNNRs from multi-walled BNNTs (Fig. 14a). In the process, precursor BNNTs were deposited onto a Si substrate and spin-coated with a layer of poly(methyl methacrylate) (PMMA). The polymer layer with embedded nanotubes was peeled off, turned over, and subjected to plasma treatment. While the bottom and the side of each nanotube were protected by the polymer, the nanotube top surfaces were ablated away and they became “half-opened” BNNRs with widths as narrow as  $\sim$ 15 nm and lengths up to a few  $\mu\text{m}$ . The plasma treatment conditions could be tailored to controllably form BNNRs with defined ranges of layers down to

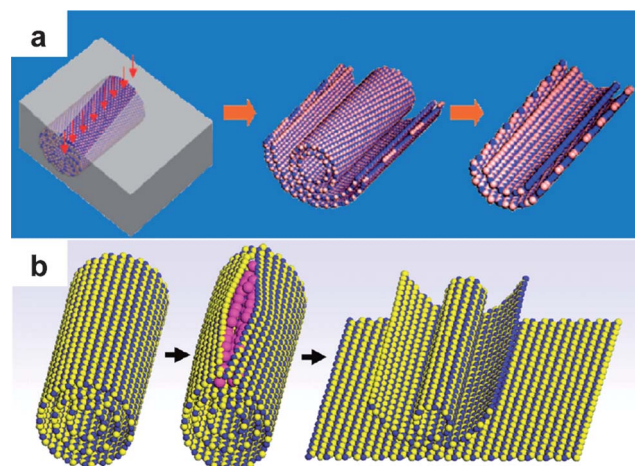


**Fig. 14** Schematics for the syntheses of BNNRs from BNNTs. (a) Plasma etching:<sup>58</sup> BNNTs were embedded within a thin PMMA film and partially etched with Ar plasma from the top. Further thinning and exfoliation lead to BNNRs. (b) Intercalation-induced unzipping:<sup>68</sup> the pristine BNNT (left) begins to locally unzip owing to potassium intercalation induced pressure buildup (middle), which results in further splitting of the nanotube in the longitudinal direction to form few-layered BNNRs. Reproduced with permission from ref. 58 (Copyright © 2010 American Chemical Society) and ref. 68 (Copyright © 2011 American Chemical Society), respectively.

a single sheet. In general, BNNT starting materials and BNNSSs are insulators, but BNNRs exhibited semiconducting behavior from *in situ* electrical measurements of a single ribbon, consistent with theoretical predictions.<sup>71–75,149</sup>

Intercalation of h-BN with alkali metal is known to be more difficult than graphite and has been much less reported.<sup>150</sup> However, Erickson *et al.* found that the intercalation of vaporized potassium metal into BNNT walls (300 °C for 72 h in vacuum) was efficient enough to induce longitudinal splitting of BNNTs (Fig. 14b).<sup>68</sup> High aspect ratio and few-layered BNNRs were obtained with lengths over 1 μm, widths between 20 and 50 nm, and thickness between 2 and 10 layers. Despite the relatively low yield (~1%), this route is a bulk process and might potentially be scalable if an effective purification/separation procedure could be established. Mechanistically, the intercalated potassium atoms might have formed islands that continuously grew to induce circumferential strain around the BNNT surface, which eventually led to bond breakage at the weakest points such as sp<sup>3</sup> bonding sites. Subsequent cleavage was preferably longitudinal along the BNNT axis likely because of the repulsion forces of potassium-bonded breakage points. Many BNNRs were still attached to the parent nanotubes after formation and could be separated by sonication in a solvent such as isopropanol. The authors suggested that since most BNNTs were of either armchair or zigzag chiralities, the resultant BNNRs should inherit these structural characteristics due to the longitudinal nature of the “unzipping” process.<sup>68</sup>

## 4.2. Bottom-up methods

**4.2.1. Epitaxial BNNSSs from CVD.** CVD preparation of epitaxial BNNSSs (“boron nitride thin films”) may be dated back to the 1960s. The first journal article on the subject was published in 1968, in which Rand and Roberts used diborane (B<sub>2</sub>H<sub>6</sub>) and ammonia (NH<sub>3</sub>) as precursors for the deposition of BNNSSs in the temperature range of 600–1080 °C on various substrates, including Si, Ta, Mo, Ge, and fused silica.<sup>151</sup> Several excellent review articles are available that summarize many early efforts in the last few decades of the twentieth century.<sup>152</sup> Generally, the CVD precursors for BNNSSs could be either separate B and N compounds (*e.g.* BF<sub>3</sub>–NH<sub>3</sub>, BCl<sub>3</sub>–NH<sub>3</sub>, B<sub>2</sub>H<sub>6</sub>–NH<sub>3</sub>) or a single precursor [*e.g.* ammonia borane (or borazane, BH<sub>3</sub>NH<sub>3</sub>), borazine (B<sub>3</sub>N<sub>3</sub>H<sub>6</sub>)]. Although relatively less stable, the single precursors are usually more desirable because of low toxicity and the inherently defined 1 : 1 B : N stoichiometry.<sup>18</sup>

It has been recently predicted<sup>153</sup> and demonstrated<sup>154–156</sup> that high-quality BNNSSs could serve as dielectric substrates analogous to and advantageous over conventional Si substrates for high performance graphene electronics. This is because BNNSSs not only have a matching lattice with graphene, but are also atomically smooth and free of dangling bonds. The top-down preparation of BNNSSs, such as the Scotch tape method and wet exfoliation methods, either lack scalability and/or could only produce exfoliated nanosheets with insufficient lateral sizes. Therefore, some researchers turned their attention to modifying the conventional CVD production methods. Many of those previously reported methods,<sup>152</sup> however, only yielded small crystalline area monolayer BNNSSs that were difficult to transfer

onto arbitrary substrates, and thus not suitable for electronic applications.

Song *et al.* first demonstrated an ambient pressure CVD method to prepare large area, transferrable few-layered BNNSS films with continuous areas up to a few cm<sup>2</sup>.<sup>17</sup> The experiments were conducted using sublimated ammonia borane as a precursor. It was decomposed at 1000 °C on a Cu substrate in Ar/H<sub>2</sub> flow. Comprehensive microscopy and spectroscopy characterizations suggested that the nanosheets prepared were mostly of 2–5 layers and exhibited structural and electronic properties consistent with the expected hexagonal structures. The similar lattice constants of the Cu substrate and BNNSSs (0.255 vs. 0.25 nm, or only ~2% mismatch) were essential to generate large flat nanosheets.

Under such CVD conditions, however, the formation of impurities in the form of particles is common and could be detrimental for electronic applications.<sup>17,19,156</sup> Kim *et al.* suggested that the large particle impurities were the byproducts from the precursor pyrolysis and were transferred into the growth zone by the carrier gas.<sup>19</sup> Therefore, in a modified system, no carrier gas was used and the ammonia borane vapor was allowed to diffuse into the growth zone. Indeed, clean BNNSSs were obtained since the heavier particulate impurities could not diffuse as far. Various spectroscopic and microscopic analyses indicated that the nanosheets were smooth monolayers (Fig. 1e) with surface roughness as low as 0.181 nm. In comparison, the underlying SiO<sub>2</sub>/Si substrate showed a higher roughness of 0.222 nm. Although the monolayer BNNSSs were of large area over centimeters (Fig. 3a), nanosheet films larger than 4 μm<sup>2</sup> usually contained multiple domains as different sets of crystalline orientations were shown in the electron diffraction.

Triangular-shaped structures, either as “dots” (islands/nanosheets) or “antidots”<sup>41,44</sup> (vacancy defects), seem to be signatures for 2D BN nanostructures. The experimental results revealed that, during the nucleation of monolayer BNNSSs, triangular-shaped or asymmetric diamond-shaped islands were first formed at lower (60 °C) or higher (70–90 °C) sublimation temperatures, respectively (Fig. 15).<sup>19</sup> The islands continued to grow until merging to cover the entire Cu substrate, with further growth inducing multilayer formation. It was speculated that these triangles were N-edged because they are more energetically favorable than B-edged ones. Because the interactions between a BNNSS and the Cu substrate were weak, these islands were randomly oriented. The use of other substrates with stronger interactions with BNNSSs may result in well oriented triangular islands, as shown with Ni(111)<sup>157,158</sup> and Rh(111) substrates.<sup>159</sup> Interestingly, a recent report indicated that initial islands formed with the use of Ru(0001) substrates were of random shape but followed the substrate steps during growth.<sup>160</sup>

Multiple authors suggested that the quality of the Cu foil is critical for the high quality nanosheet formation.<sup>17,19,156</sup> For example, Lee *et al.*<sup>156</sup> reported a combined thermal annealing and chemical polishing technique to enhance the surface morphology (*i.e.*, flatten and increase the grain size) of Cu foil substrates (Fig. 16a–c) in a similar CVD process to that reported by Song *et al.*<sup>17</sup> The resultant few-layered BNNSSs were impurity-free and atomically flat (Fig. 16d–f), thus exhibiting high performance as dielectric substrates for graphene field effect transistors (FETs). The graphene FET devices

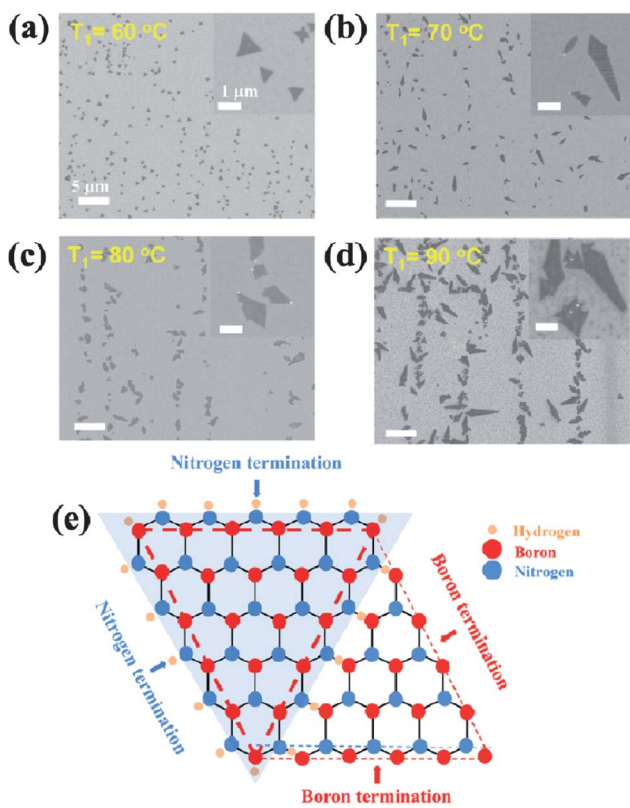


**Fig. 15** SEM images showing the dependence of nucleation of CVD-grown monolayer BNNS on the evaporation temperature of precursor ammonia borane ( $T_1$ ) at (a) 60, (b) 70, (c) 80, and (d) 90 °C. Insets show higher magnification images. (e) Schematic illustration of an N-terminated BNNS triangle; the triangle next to it can only have boron termination at the edges. Reproduced with permission from ref. 19 (Copyright © 2012 American Chemical Society).

with these BNNS substrates exhibited 2–3 fold enhancements in both on/off ratio and mobility in comparison to the use of Si substrates.

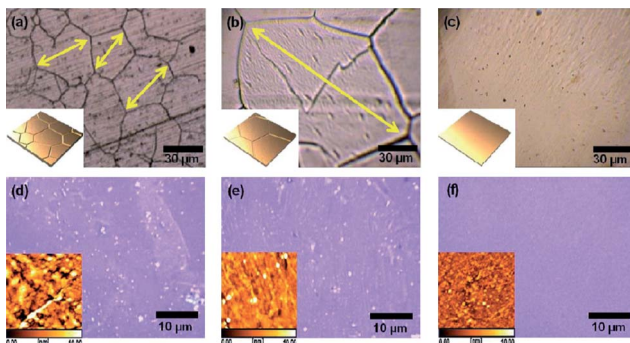


**Fig. 16** Optical images of (a) a pristine Cu foil and those by (b) thermal annealing at 1020 °C for 2 h, and (c) the same thermal annealing followed by chemical polishing. The inset images in (a–c) reveal the schematic illustrations of the morphology-controlled Cu foils. (d)–(f) are optical images showing surface morphologies of BNNSs transferred onto SiO<sub>2</sub>/Si substrates after their growth on the foils shown on (a)–(c), respectively. The inset images of (d)–(f) show the corresponding AFM images (scan area is 1 × 1 μm<sup>2</sup>; height color bar at the bottom of each image indicates 0–10 nm from left to right). Reproduced with permission from ref. 156 (Copyright © 2012 American Chemical Society).

Alternatively, CVD growth of centimeter-area few-layered BNNSs (thicknesses ~5 to 50 nm) was achieved by using borazine as a precursor for pyrolysis on polycrystalline Ni substrates.<sup>18</sup> The reaction was conducted at ambient pressure with N<sub>2</sub> as the carrier gas and at a moderate temperature of 400 °C, followed by post-annealing at 1000 °C. The relatively low CVD temperature was necessary as a higher temperature resulted in non-continuous nanosheet films. With the lattice mismatch of Ni(111) and BNNS being only 0.4%, the homogeneity of the BNNS crystalline essentially followed the underlying Ni grains. However, in another report also using Ni as a substrate (ammonia borane and hydrogen as a precursor and carrier gas, respectively), the nanosheets grew fast on Ni with a (100)-like direction, but none were detected with (111)-like facets.<sup>161</sup> This was tentatively attributed to the higher surface energy or higher catalytic activity of Ni(100) vs. Ni(111) facets. With a magnetic substrate, Ni-supported BNNSs may be used as magnetoresistive junctions that may outperform their graphene counterparts.<sup>162</sup>

Similar to the conventional CVD growth of BNNSs,<sup>152</sup> instead of a single precursor, separate B and N precursors, in this case decaborane and ammonia,<sup>158</sup> were also used in the epitaxial CVD growth of few-layered BNNSs (~2 to 15 nm) on either Ni or Cu substrates.<sup>158</sup> There was a suggestion of a 3-step approach for monolayer BNNSs on the Rh/YSZ/Si (111) substrate, where boration, oxidation, and nitration were carried out sequentially.<sup>163</sup> Trimethyl borate and ammonia were used as the B and N sources, respectively.

**4.2.2. The case of BN “nanomeshes” (BNNMs): substrate effect on monolayer BNNSs from CVD.** Epitaxial CVD growths of BNNSs have been more successful on metal substrates. The crystalline matching and the interaction strengths of the substrate with the nanosheets are both critical to the morphology of the final nanosheet structures. In 2004, Corso *et al.* reported curious epitaxial BN “nanomesh” (*i.e.* BNNM) structures observed under scanning tunneling microscopy (STM) (Fig. 17a).<sup>164</sup> Unlike the more recent CVD preparations of BNNSs discussed in the previous section which were carried out in low-pressure chambers with lattice-matched Cu or Ni substrates,<sup>17–19,156</sup> the BNNMs were grown from a borazine precursor in an ultrahigh vacuum chamber on a hot (~800 °C) Rh(111) surface. Rh(111) has a lattice mismatch of ~7% with h-BN, leading to arrays of pore-like structures with an ordered periodicity of ~3.2 nm as seen in STM images. In the original hypothesis, it was proposed that 2 incomplete flat atomic layers were formed and offset at the pore locations with different diameters in the top and bottom layers, with the pores being actual structural openings.<sup>164</sup>

However, it was soon argued that such double-layer structures would be highly unstable.<sup>165–167</sup> Furthermore, the “layer–layer distance” deduced from the above model was only ~0.055 nm, much smaller than the van der Waals distance (~0.33 nm) in typical few-layered BNNSs and h-BN. An alternative monolayer model was then proposed that not only resolved the above inconsistencies, but also explained the STM and the related spectroscopic results.<sup>165–168</sup> In this revised model, the “nanomesh” is a complete but highly corrugated monolayer. The “pores” are in fact the shallow regions that strongly interact with the substrate thus with a closer distance, while the surrounding

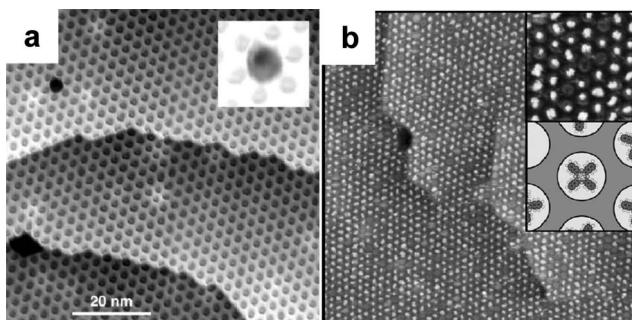


**Fig. 17** (a) A STM image (bias voltage =  $-1.0$  V; tunneling current =  $2.5$  nA) of BNNM grown on a Rh(111) surface *via* ultrahigh vacuum CVD of borazine.<sup>164</sup> The inset is a high contrast view of a defect structure on the main figure. (b) A STM image ( $120 \times 120$  nm $^2$ ; bias voltage =  $1.3$  V; tunneling current =  $0.3$  nA) showing a nearly complete monolayer coverage of naphthalocyanine molecules on a BNNM on Rh(111).<sup>168</sup> The inset on the top shows an enlargement ( $19 \times 19$  nm $^2$ ) and gives a high-resolution view that shows the trapping of the naphthalocyanine molecules inside the nanomesh pores. The inset on the bottom shows a schematic representation of the molecules in the pores. Reproduced with permission from ref. 164 (Copyright © 2004 American Association for the Advancement in Science) and ref. 168 (Copyright © 2007 Wiley-VCH), respectively.

area (the “wires”) are less strongly attached (Fig. 18a).<sup>168</sup> This happens because the nanosheet–metal interactions are such that N atoms are attracted to the metal atoms while the B ones are repelled from them. With the presence of a lattice mismatch between the BNNS and the substrate, there are periodic areas where N atoms are sitting right above Rh atoms and thus have the most interaction strength while there are offsets at other regions (Fig. 18b).

Interestingly, the corrugation of the “BNNM” structure on Rh(111) could be relieved and it could be converted into a flat BNNS by insertion of H atoms *via* exposure to atomic hydrogen.<sup>169</sup> This provided direct experimental evidence that the “pores” were topographical rather than structural. *In situ* STM studies showed that the formation of BNNMs also went through intermediate islands with triangular shapes,<sup>159</sup> as in the non-corrugated BNNS growth on Cu and Ni substrates discussed in the previous section.<sup>19,157,158</sup>

It was found that the bonding of epitaxial BNNSs/BNNMs with various transition metal substrates all fell within this monolayer model but with different interaction strengths and lattice mismatching degrees.<sup>170–172</sup> DFT calculations suggested that the interactions between BNNSs/BNNMs and the metals on the 4d row are the largest, but decrease with an increasing number of d electrons.<sup>171</sup> Such predictions were supported by experimental results that the use of weakly bonding metal facets such as Cu(111) or Ag(111) would require the borazine precursor dosages to be increased by nearly 10 and 300 times those used in the case of Rh(111).<sup>172</sup>

It should be cautioned that a large lattice mismatch does not necessarily lead to strong corrugation, which is more dependent on the nanosheet–substrate interaction strength. For example, Pt(111) and Ir(111) both have a larger lattice mismatch with BNNSs (10.8% and 8.6%, respectively) than Rh(111) and Ru(0001) (7.6% and 8.2%, respectively), but little to no

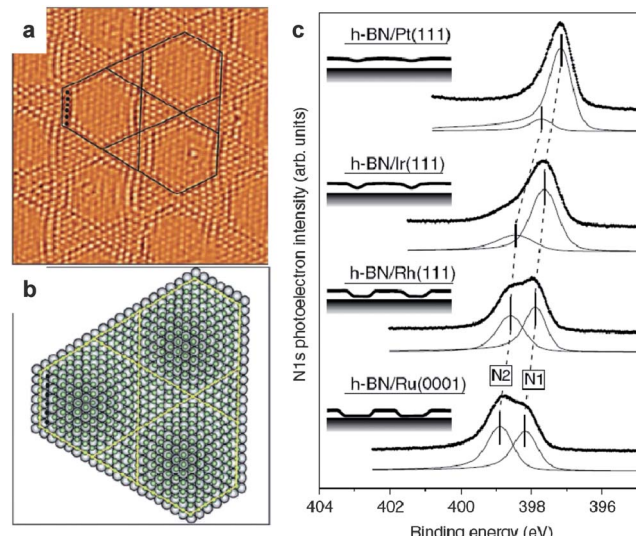


**Fig. 18** Monolayer model for “BNNMs”. (a) A filtered STM image of a BNNM on Rh(111) emphasizing the atomic corrugation. (b) An atomic model of the nanomesh for the highlighted area in (a). Only N atoms (green-colored) in the BN structure are shown for clarity. Larger light-colored spheres are the Rh lattice underneath. The model clearly shows a lattice mismatch between BN and Rh(111). The area where N atoms sit on top of the Rh atom exhibits stronger bonding, resulting in “pores”. (c) Spectroscopic evidence (N 1s photoelectron spectra) and the corresponding schematic representations (insets) of different interaction strengths for monolayer BNNS/BNNM with different metal substrates: Pt(111) < Ir(111) < Rh(111) < Ru(0001). The higher energy N<sub>2</sub> component in the photoelectron spectra was attributed to N atoms interacting more strongly with the metal substrate. Reproduced with permission from ref. 168 (Copyright © 2007 Wiley-VCH) and ref. 172 (Copyright © 2007 Elsevier), respectively.

corrugation was found on the grown monolayer (Fig. 18c).<sup>172</sup> The latter two substrates were among ones that interact strongly with BNNSs, resulting in nanosheets with periodic corrugation of different morphologies including the originally observed nanomeshes.<sup>164–170,173</sup> It is interesting to acknowledge that, instead of single crystal Rh(111), the use of an epitaxially grown Rh(111) film [on Si(111) with a yttrium-stabilized-zirconia buffer layer] slightly changed the supported BNNM periodicity. The different thermal expansion characteristics of the substrate resulted in a slightly different lattice mismatch.<sup>174</sup> Substrates with weaker interactions with BNNSs led to nanosheets with either a variety of corrugation domains [Pd(110),<sup>175</sup> Pd(111)<sup>176</sup>] or much flatter planar nanostructures [Pt(111)<sup>177,178</sup>]. The uni-directional lattice matching of BNNSs and a Fe(110) surface created a highly periodic “wavy” epitaxial monolayer nanosheet.<sup>179</sup>

BNNMs retained the dielectric properties of nanosheets despite their corrugated topography<sup>180</sup> and were thermally stable.<sup>181</sup> Under ultrahigh vacuum conditions, the oxidative etching of BNNM occurred beyond  $600$  °C at  $1 \times 10^{-6}$  mbar O<sub>2</sub> concentration.<sup>182</sup> Deposition of Au nanoparticles masked the defects where etching propagated and improved the stability of the nanomesh against oxidation.<sup>182</sup> Although prepared under ultrahigh vacuum, the morphology of BNNMs was stable in air,<sup>183</sup> aqueous conditions with acidic pH, or even under electrochemical conditions.<sup>184</sup> The stability of BNNMs enabled unique

applications for templated formation of supramolecular periodic structures in the corrugated “pores”. The species trapped with BNNMs included organic molecules [such as naphthalocyanine (Fig. 17b),<sup>168</sup> Cu-phthalocyanine,<sup>185</sup> and pentacene<sup>186</sup>], nanoparticles (such as Au<sup>167,187</sup> and Co<sup>188</sup>), fullerene C<sub>60</sub> molecules,<sup>164</sup> or even ice clusters at low temperature.<sup>189</sup>

It is worth noting that similar epitaxial graphene “nanomeshes” with shallow corrugated “pore” structures could also be prepared on Rh(111)<sup>190</sup> or Ru(0001) substrates.<sup>191</sup> The “pores” were also shown to trap organic molecules, forming ordered arrays.<sup>190</sup>

**4.2.3. Non-epitaxial growths.** There have been many bottom-up preparation methods with CVD or solid-state reactions for non-epitaxial BNNSSs of various morphologies. Industrial productions of h-BN powder (typically a few to tens of micrometers in lateral size and a few hundred nanometers in thickness) often use solid-state reactions between a boron precursor, such as B<sub>2</sub>O<sub>3</sub> or H<sub>3</sub>BO<sub>3</sub>, and a nitrogen precursor, such as melamine or urea.<sup>152</sup> Gaseous ammonia is also used.<sup>152</sup> Similar processes were also developed to produce BNNSSs with various thicknesses. For example, Nag *et al.* directly heated a mixture of boric acid and urea with various ratios at 900 °C under N<sub>2</sub> to prepare thin BNNSSs with surface areas as high as 927 m<sup>2</sup> g<sup>-1</sup>.<sup>147</sup> It was claimed that the layer number of BNNSSs could be controlled *via* increasing the urea content in the precursor mixture. Nanosheets with 1 to 4 layers were obtained with a 1 : 48 boric acid-to-urea ratio. In another attempt, much thicker BNNSSs (or “thin h-BN discs”) of ~35 nm thickness and close to 1 μm diameter were prepared by heating a B<sub>2</sub>O<sub>3</sub> and melamine mixture at 1200 °C under N<sub>2</sub>.<sup>192</sup> The thicknesses of the discs could be further reduced to ~20 nm by increasing the reaction temperature to 1300 °C. More recently, BNNSSs with thicknesses of ~30 nm and lateral sizes of a few hundred nm have been prepared by combustion of a slurry of precursors, *i.e.*, a gel like aqueous solution of boric acid, sodium azide, ammonium chloride, and urea, followed by annealing the disordered BN products at temperatures above 1200 °C.<sup>193</sup>

Several groups of authors described different processes in which the formed BNNSSs protruded from the substrate used.<sup>129,136,194–199</sup> For example, vertical BNNSS structures were formed on an n-type Si substrate *via* microwave plasma CVD from a gaseous mixture of BF<sub>3</sub>, N<sub>2</sub>, and H<sub>2</sub> at 800 °C with a microwave power of 800 W (Fig. 19a).<sup>194,195</sup> The authors suggested that the vertical growth pattern was likely induced by the electric field in the plasma sheath.<sup>194</sup> It was also proposed that the nanosheet formation was a balanced interplay between the etching effect of fluorine and the neutralizing effect of hydrogen atoms in the system. As a result, the nanosheets became thinner and grew higher and longer into branched hierarchical structures at low H<sub>2</sub>/BF<sub>3</sub> flow rate ratios. At high H<sub>2</sub> flow conditions (thus no F-etching), the h-BN particle products became more coarse and granular. The growth conditions could be tuned so that the products were mostly few-layered and monolayer BNNSSs.<sup>195</sup> Alternatively, Pakdel *et al.* used B powder and flowing NH<sub>3</sub> gas as precursors with MgO and FeO as catalysts for the growth of vertically aligned few-layered BNNSSs on Si/SiO<sub>2</sub> substrates at temperatures between 1000 and 1200 °C (Fig. 19b and c).<sup>136</sup> It was suggested that the initial growth was planar, but the

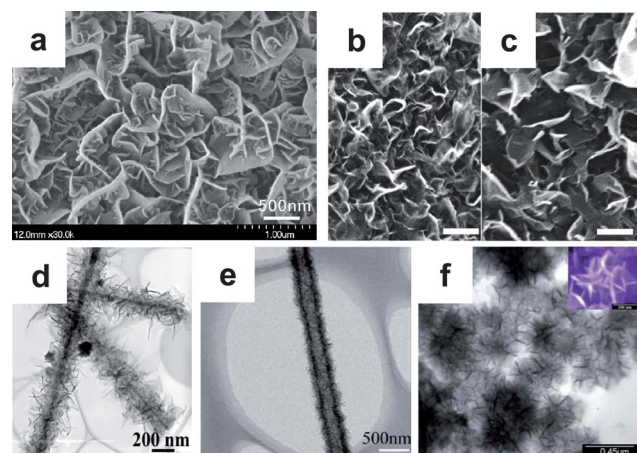


**Fig. 19** Non-epitaxially grown BNNSSs: (a) vertically grown BNNSSs on a Si wafer from microwave plasma CVD growth using BF<sub>3</sub>, N<sub>2</sub>, and H<sub>2</sub> as a precursor gaseous mixture (flow rate ratio of BF<sub>3</sub> : H<sub>2</sub> = 5 : 10);<sup>194</sup> (b and c) vertically grown BNNSSs on a Si/SiO<sub>2</sub> substrate from CVD growth using B, MgO, FeO and ammonia as precursors/catalysts at 1100 and 1200 °C, respectively (scale bars = 200 nm);<sup>136</sup> (d) protruding BNNSSs decorated on Si<sub>3</sub>N<sub>4</sub> nanowires from sequential growth of Si<sub>3</sub>N<sub>4</sub> nanowires from heating Si powder in N<sub>2</sub> followed by BNNSS formation with further heating the nanowires with a B–N–O mixture and B<sub>2</sub>O<sub>3</sub> in N<sub>2</sub>/NH<sub>3</sub>;<sup>197</sup> (e) protruding BNNSSs decorated on BN fibers from CVD growth with a B–N–O–Fe precursor using ZnS powder as templates;<sup>198</sup> and (f) BN nanoflowers from heating a mixture of NaBF<sub>4</sub>, NaN<sub>3</sub> and NH<sub>4</sub>Cl in an autoclave.<sup>129</sup> Reproduced with permission from ref. 194 (Copyright © 2010 American Chemical Society), ref. 136 (Copyright © 2011 American Chemical Society), ref. 197 (Copyright © 2006 American Chemical Society), ref. 198 (Copyright © 2011 Royal Society of Chemistry) and ref. 129 (Copyright © 2011 Royal Society of Chemistry), respectively.

overgrowth at grain boundaries led to layers that curled upward, resulting in the vertical growth. The thicknesses of the BNNSSs were mostly less than 4 nm, with the nanosheets grown at higher temperatures exhibiting more crystallinity.

Both the above as-prepared BNNSS structures exhibited superhydrophobicity due to the vertically aligned topography.<sup>136,194</sup> In a somewhat related report, protruding BNNSS structural coatings imparted water resistance to phosphor (SrAl<sub>2</sub>O<sub>4</sub>:Eu<sup>2+</sup>) particles.<sup>196</sup> The BNNSS-coated phosphors were prepared in a one-pot reaction, in which B<sub>2</sub>O<sub>3</sub> was mixed with solid precursors of the phosphor and reacted at 1300 °C under a N<sub>2</sub>/NH<sub>3</sub> flow.

Protruding BNNSSs were also synthesized on 1D nanomaterial template surfaces in CVD processes, forming hierarchical nanostructures. For example, Zhu *et al.* synthesized BNNSS-coated Si<sub>3</sub>N<sub>4</sub> nanowires by using a two-stage solid phase synthesis (Fig. 19d).<sup>197</sup> In this process, the nanowires were formed first followed by vapor deposition of BNNSSs from B–N–O precursors in flowing N<sub>2</sub>/NH<sub>3</sub> at 1750 °C. Alternatively, Chen and Zou mixed ZnS powder into solid B–N–O–Fe precursors with NH<sub>3</sub> to prepare BN fibers with surface-protruding BNNSS (Fig. 19e).<sup>198</sup> Both hierarchical hybrid structures containing protruding BNNSS were shown to be excellent field emitters (see Section 6.3.).<sup>197,198</sup> Instead of ZnS powder, ZnS ribbons were also used in a similar process as templates.<sup>199</sup> BNNSSs thus formed coated both sides of the ZnS ribbons at thicknesses of ~12 nm.<sup>199</sup>

ZnS was subsequently thermally evaporated, leaving hollow micron-sized 2D BN ribbons as the final structure.

Without the use of substrates, particles consisting of protruding BNNSSs (“nanoflowers”) were synthesized in a solid state reaction of NaBF<sub>4</sub>, NH<sub>4</sub>Cl, and NaN<sub>3</sub> in an autoclave at 300 °C for 20 h (Fig. 19f).<sup>129</sup> The BNNSSs in the nanoflowers could be isolated/exfoliated and dispersed in DMF *via* simple sonication.

It should be noted that many of these protruding BNNSSs are highly polycrystalline in nature. There were a large number of facets from the hexagonal phases, making each particle appear corrugated when dispersed in solvents.<sup>129,136,194,195</sup> Thus, they are morphologically quite different from the flat nanosheets obtained from exfoliation or epitaxial growth that were discussed previously. Gram-quantity corrugated BNNSSs may also be prepared by using B<sub>2</sub>O<sub>3</sub> and hydrazine as precursors in the presence of Zn metal in an autoclave reaction at 500 °C for 12 h.<sup>200</sup> The reducing power of the metal appeared to be crucial, as replacing Zn with Fe dramatically decreased the yield while the use of Mg produced a similar yield but with somewhat thicker nanosheets. These corrugated BNNSSs powders exhibited a high surface area (226 m<sup>2</sup> g<sup>-1</sup>) and could be used to support nanoparticles for catalysis applications (see Section 6.2.).<sup>200</sup>

An interesting “chemical blowing” approach was used to produce few-layered BNNSSs with large lateral dimensions (over 100 μm) from CVD of ammonia borane (Fig. 20).<sup>201</sup> In the catalyst-free and substrate-free process, hydrogen was rapidly released by the ammonia borane decomposition and became encapsulated in the soft aminoborane polymers that initially formed below 200 °C. This resulted in bubbles within the polymer walls that eventually transformed into BNNSSs when heated

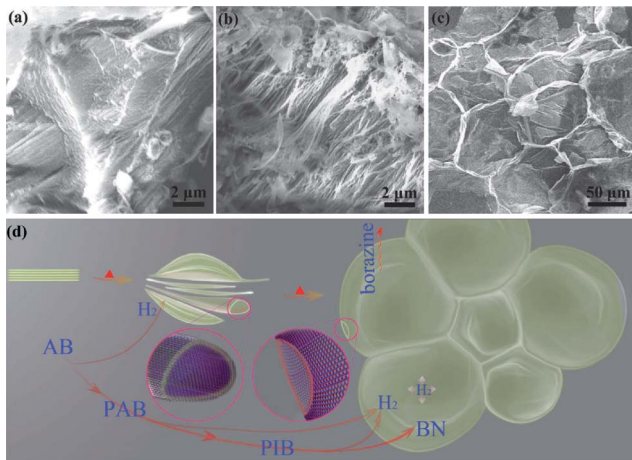


**Fig. 20** BNNSSs from “chemical blowing”:<sup>201</sup> (a) SEM image of a raw ammonia borane molecular crystal with the ribbon-like morphology at room temperature; (b) morphology of the slightly disordered ribbon-stack of an intermediate obtained after pretreatment at 80 °C for 30 min; (c) morphology of an intermediate (produced at 400 °C) showing densely packed bubbles connecting with each other in a manner resembling a soap form; (d) a sketch explaining the growth process during the chemical blowing that consists of self-bubbling of a B–N–H polymer under dehydrogenation until it has atomically thin walls (AB: ammonia borane; PAB: polymeric aminoborane; PIB: polyiminoborane). Reproduced with permission from ref. 201 (Copyright © 2011 Wiley-VCH).

to 1200 °C. The nanosheets thus produced were polycrystalline, suggesting the presence of surface structural defects. Nevertheless, polymer composites containing these electrically insulating BNNSSs as fillers exhibited high transparency and enhancement in mechanical properties.

Last but not least, the preparation of BNNSSs may also be achieved in a substitution reaction using graphene sheets as the template material. In a process similar to that developed to produce BNNTs from CNTs,<sup>203</sup> Han *et al.* placed B<sub>2</sub>O<sub>3</sub> powder as the B source in the bottom of a crucible, then a layer of molybdenum oxide as a “promoter”, and finally a layer of chemically exfoliated graphene sheets as the template.<sup>202</sup> By flowing N<sub>2</sub> (N source) at a temperature of 1650 °C for 30 min, majority of the carbon atoms on the graphene planar structure were replaced by B and N. By taking advantage of the much better oxidation resistance of B–N bonds in comparison to C–C bonds, the excess carbon was removed by thermal oxidation at 650 °C in air while the BN domains were unaffected, yielding pure BNNSSs as the final product.

## 5. BNNSS-graphene hybrid nanostructures

BNNSSs and graphene are structural analogs and thus can form intimate hybrid nanostructures. These can be roughly divided into in-plane and interlayer (or heterolayer) categories. The studies on in-plane BNNSS-graphene hybrids (also called BCN hybrid nanosheets) are essentially an extension of the research on various BCN structures in the notion to synthesize an intermediate compound between conducting C and insulating BN. Similar to the research on BNNSSs, there have been decades of work on BCN structures.<sup>204,205</sup> BNNSS-graphene heterolayer structures were first prepared in the mid-1990s.<sup>206</sup> Recent research in this direction mainly targets applications in graphene electronic devices in which BNNSSs usually act as high performance dielectric substrates and/or unique thin dielectric separation layers in the devices. Therefore, such heterolayers should be treated as novel device architectures rather than new materials.

### 5.1. In-plane BNNSS-graphene hybrids: BCN hybrid nanosheets and nanoribbons

**5.1.1. Hybrid nanosheets.** The structural similarities between graphene and a BNNSS allow them to form essentially seamless in-plane hybrids with continuously tunable C:BN stoichiometry. Since the two types of nanosheets are zero-gap (conductive) and wide-gap semiconductors (insulating), respectively, the electronic structures of such hybrids with various compositions can enable unique device architectures.

Many CVD approaches for BNNSSs, including both epitaxial and non-epitaxial growth methods, may be conveniently tailored to produce BCN hybrid nanosheets simply by adding a gaseous carbon source in the reaction mixture<sup>199,201,207,208</sup> or with the presence of graphite.<sup>209</sup> A significant breakthrough on the controlled CVD preparation and characterization of epitaxial BCN nanosheets has recently been reported by Ci *et al.*, who prepared hybrid nanosheets on Cu substrates by adding methane as the carbon source along with ammonia borane as the BN source at 900–1000 °C (Fig. 21).<sup>207</sup> This procedure was quite similar to that for pure epitaxial BNNSSs reported separately by

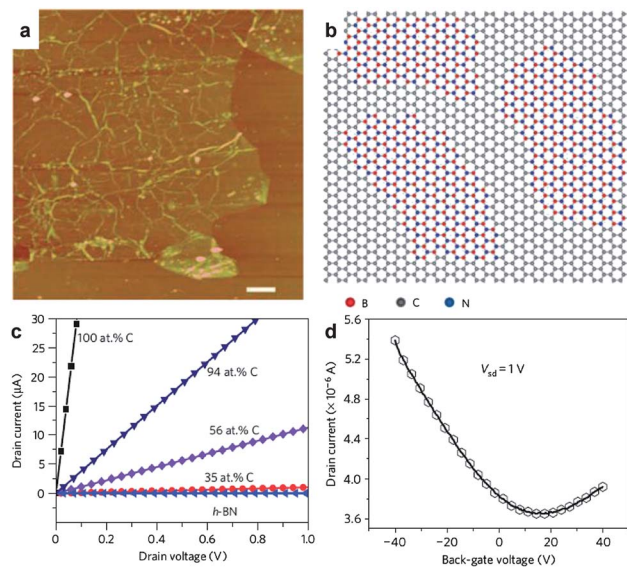


**Fig. 21** CVD-grown BCN hybrid nanosheets.<sup>207</sup> (a) An AFM image showing a large lateral area with uniform thickness (scale bar = 1  $\mu\text{m}$ ); (b) proposed atomic model of the nanosheets showing hybridized BNNS and graphene domains; (c) room temperature current–voltage characteristics of as-grown nanosheets with different percentages of carbon; (d) the drain current as a function of the voltage applied to the back gate for a 7  $\mu\text{m}$  wide BCN ribbon with 40% carbon (drain–source voltage  $V_{\text{sd}}$  was fixed at 1 V). Reproduced with permission from ref. 207 (Copyright © 2010 Nature Publishing Group).

the same group of authors (see Section 4.2.1.).<sup>17</sup> The hybrid nanosheets were of  $\sim$ 1 nm in thicknesses (2 or 3 layers) with rotational stacking faults (neither AB nor AA' stacking). The carbon content was continuously tunable from 10–100% (*i.e.*, graphene). With change in the carbon concentration, the hybrid films showed resistivity from insulating to a reasonably low value (*e.g.*  $10^{-3} \Omega \text{ cm}$  at 94% C) (Fig. 21c). The FET devices fabricated using these nanosheets exhibited typical ambipolar semiconducting behavior (Fig. 21d).

Other than bottom-up CVD growths, BCN hybrid nanosheets could also be prepared by either doping BN structures with C or replacing C atoms in graphene with BN. For example, Wei *et al.* have recently reported the C-doping of various BN nanostructures including BNNTs, BNNSs, and BNNRs by electron beam irradiation in the presence of solid paraffin wax as the carbon source in an electron microscope.<sup>210</sup>

The reverse way of doping, *i.e.*, the substitution of C atoms in graphene using B and N, was already discussed in the previous section, but only the direct products BCN hybrid nanosheets were further oxidized to remove carbon to obtain pure BNNSs.<sup>202</sup> Several authors have produced BCN hybrid nanosheets by applying this method to either substrate-supported<sup>211</sup> or powdery graphene starting materials.<sup>202,212</sup> In the reactions using B and N to substitute carbon, either boron oxide<sup>202,211</sup> or boric acid<sup>212</sup> could be applied as the B source. The use of ammonia instead of  $\text{N}_2$  could reduce the reaction temperature to less than 1000 °C.<sup>211,212</sup> This feature in the preparation of substrate-supported BCN hybrid nanosheets could be advantageous in comparison to epitaxial CVD growth methods since target substrates such as  $\text{SiO}_2/\text{Si}$  could be directly used to support

graphene starting materials at this temperature. This could avoid the complex transfer process involving sacrificial metal substrates and/or adhesive films. The carbon contents in the hybrid nanosheets from these reactions could be controlled to a certain extent by applying different reaction temperature,<sup>211</sup> reaction time,<sup>212</sup> or subsequent controlled oxidation.<sup>202</sup> A FET device with these hybrid nanosheets from BN-substituted graphene also showed very similar ambipolar behavior as seen with the CVD-grown nanosheets shown in Fig. 21d.<sup>211</sup> Interestingly, the BCN hybrid nanosheets also exhibited excellent catalytic performance for oxygen reduction reaction, which is an important fuel cell process.<sup>212</sup>

Theoretical calculations suggested that the BCN hybrid nanosheets were not from random C atom insertion in BNNSs (or random BN pair insertion in graphene), but had structures with maximal numbers of B–N and C–C bonds, thus discrete BNNS–graphene domains that are thermodynamically stable (Fig. 21b).<sup>207,213</sup> A recent computation study further suggested that the clusters of either BN in C or C in BN should take well-defined geometrical shapes such as triangles (zigzag-edged) and hexagons (armchair-edged) under equilibrium conditions.<sup>214</sup> This appears to be consistent with the most common shapes of the BNNS islands and defects discussed previously. For the synthesis reactions where B and N substitute for C atoms in graphene, a theoretical study implied that the substitution should initially occur at the defect domains of graphene.<sup>215</sup> This suggested that the remaining  $\text{sp}^2$  carbon domains could retain high crystallinity.

Experimental evidence also supported the phase-segregation scenario. For example, in the XPS data of the CVD-grown BCN hybrid nanosheets, B–N and C–C bonds dominated the respective 1s spectra.<sup>207</sup> If there were random atomic distribution, B–C and N–C signals would have been much more significant. Another possible scenario was the BNNS–graphene stacked structure (or “heterolayers”, see the next section). However, the fact that the C:BN ratio could be tuned over the full range can only be explained by an in-plane hybrid structure. That for double-layered stacked structures would have been  $\sim$ 50%. Also, Raman spectra showed a significantly higher D-band in comparison to the graphene sample using the same procedure (C  $\sim$  100%; BN  $\sim$  0%), which could be explained by the disorder and boundaries between C and BN phases.

The tunable conductive properties of the BNNS–graphene hybrid nanosheets are consistent with theoretical predictions based on such a separate domain model.<sup>216–221</sup> It was shown that the energy states near the Fermi level in such hybrid structures would be strongly localized at the graphene domains,<sup>216</sup> but the confinement might be relaxed by the surrounding BN lattice.<sup>217</sup> Both electronic and magnetic properties of the hybrid nanosheet are strongly affected by both the size and shape of the graphene or BN islands.<sup>214,217–220</sup> For example, larger sizes of graphene island should provide a reduced bandgap (*i.e.*, “more C, more conductive”).

**5.1.2. Hybrid nanoribbons.** The in-plane BNNS–graphene hybrids in the form of nanoribbons, *i.e.*, BNNR–GNR hybrids, have been theoretically investigated by many authors. Again, the systems could be viewed as either C-doped BN (thus with a decreased bandgap as compared to BNNR) or BN-doped C (thus with an increased bandgap as compared to GNR). The

systems that have been studied consist of two or more alternative BNNR–GNR phases that are bonded along either the length side (herein dubbed as “l-type”; Fig. 22a)<sup>219,222–233</sup> or the width side (“w-type”; Fig. 22b).<sup>234–236</sup> Recent experiments showed that C-doping of few-layered BNNRs *via* electron irradiation in the presence of a carbon source seemed to both occur at the edges and form domains along the ribbon body.<sup>210</sup> These experimentally prepared structures are apparently much less defined than the theoretical models of l- and w-type BNNR–GNR hybrids.

It was predicted that the C–BN boundary stress in l-type graphene–BNNS hybrid structure is much lower than the edge stresses in GNR and BNNR.<sup>230</sup> This suggests that the C–BN interface has less tendency to ripple, unlike the parent sheets/ribbons of graphene and a BNNS. Since l-type armchair BNNR edges are more stable than zigzag ones, BNNR strips would preferably exist external to GNR strips in armchair l-type hybrids, while the reverse is true in zigzag configurations.<sup>231</sup>

Similar to graphene domains in graphene–BNNS hybrid nanosheets, the GNR strips in l-type hybrid nanoribbons are the confined conductive channels and thus often referred to as “graphene nanoroads”. For hybrids with zigzag edges, the bandgap values decreases with increasing width in GNR strips (similar to “more C, more conductive”) but are independent of the BNNR width.<sup>222–226</sup> In addition to the GNR strips, zigzag C–B bonding interfaces could also provide additional transport channels.<sup>227</sup> From the viewpoint of BN-doping of graphene, the bandgap of armchair GNRs (originally zero) is opened by confinement of BNNRs on both edges.<sup>222,224,225</sup> Magnetically, zigzag hybrid nanoribbons may become spin-polarized at the GNR edges, creating half-metallicity<sup>222,223,228,229,232,233,237</sup> with bandgaps tunable with an external electrical field.<sup>222</sup> Interestingly, doping with C ad-atoms may also induce magnetism on BNNTs and BNNSs.<sup>238</sup>

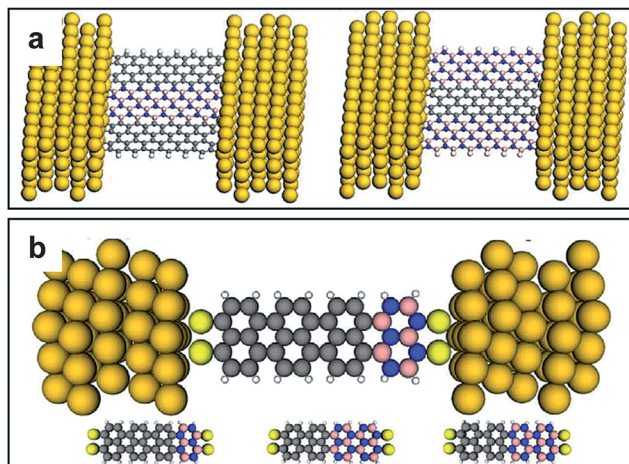


**Fig. 22** Schematics of BCN hybrid nanoribbon devices: (a) examples of “l-type”: a zigzag GNR–BNNR–GNR structure (left) and a zigzag BNNR–GNR–BNNR structure, both with two phases bonded along the length side of the nanoribbons;<sup>227</sup> (b) examples of “w-type”: the two armchair phases are bonded at the width side (other configurations are shown at the bottom of the image).<sup>235</sup> Golden-colored spheres represent the Au electrodes. Reproduced with permission from ref. 227 (Copyright © 2011 American Chemical Society) and ref. 235 (Copyright © 2011 American Institute of Physics), respectively.

w-type BNNR–GNR hybrids are much less prevalent in the literature. In this case, both BNNR and GNR domains share the same type of edges, but with no direct conductive GNR channels. As in neat armchair BNNRs, the bandgap of w-type armchair BNNR–GNR hybrids oscillates with the ribbon width, but increases with the lengths of the BNNR.<sup>234</sup> These armchair hybrid ribbons also exhibit distinct negative differential resistance (NDR) behavior.<sup>235</sup> Similar to their neat nanoribbon counterparts, w-type zigzag BNNR–GNR hybrid ribbons may also exhibit spin polarization and become half-metal at a suitable width and C:BN ratio.<sup>236</sup>

## 5.2. BNNS–graphene (BN–G) heterolayer architectures

As discussed in the previous sections, the recent attention on 2D BN nanostructures has been partially driven by their potential application as dielectric substrates for high quality graphene electronics. Conventional SiO<sub>2</sub> substrates result in graphene devices with properties much lower than expected due to a variety of factors that limit the carrier mobility, such as surface roughness, charged impurities, and surface optical phonons. While suspended graphene without any substrate may provide high performance, such devices are too delicate to be scalably prepared and applied. BNNSs have very similar dielectric properties to SiO<sub>2</sub> with a dielectric constant of ~4 and a breakdown voltage of ~0.7 V nm<sup>-1</sup>.<sup>154</sup> As the isoelectric analog of graphene, a BNNS seems to be a perfect candidate as the dielectric substrate because it has a large bandgap and a very similar lattice constant to graphene, as well as an atomically smooth surface that is free of dangling bonds and charge traps.<sup>154</sup> Also, it has been recently suggested that BNNSs inserted between two graphene layers could not only suppress interlayer scattering of graphene electrons and improve carrier mobility and current density, but also provide additional heat diffusion pathways for conductive multi-layer graphene channels<sup>239,240</sup> and enhanced magnetoelectric effects.<sup>241</sup>

**5.2.1. Preparation of BN–G heterolayers.** Although the attempt to prepare graphene–BNNS double layer systems could be dated much earlier,<sup>206</sup> the first graphene-on-BNNS electronic device was only fabricated very recently by Dean *et al.*<sup>154</sup> The device was prepared by transferring a mechanically exfoliated monolayer or bilayer graphene onto a relatively thick (~14 nm) few-layered BNNS that was mechanically exfoliated from h-BN single crystals. The graphene layer conformed well with the highly smooth BNNS layer underneath, whose roughness was three times less than SiO<sub>2</sub>. This was further confirmed in a subsequent STM study, which showed that not only topography of the graphene layer but also its charge density were significantly reduced by using a BNNS as the substrate as compared to SiO<sub>2</sub> (Fig. 23).<sup>242</sup> Although CVD-grown graphenes are usually less perfect than mechanically exfoliated ones, a similar microscopic homogeneity and a flat topography were also found with a CVD-grown monolayer graphene that was transferred onto a mechanically exfoliated BNNS.<sup>243</sup>

Instead of the exfoliate/grow-and-transfer technique, direct CVD growth of graphene on BNNS/h-BN was attempted without the use of metal substrates.<sup>245,246</sup> However, monolayer graphenes thus produced were non-continuous and of individual “pad”

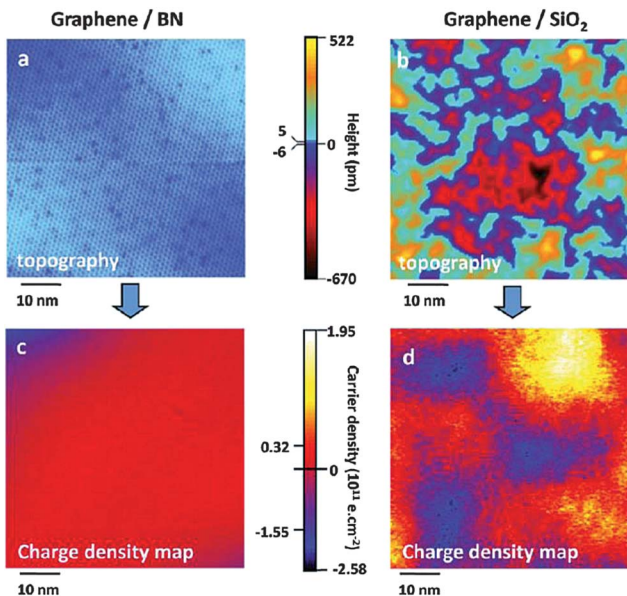


**Fig. 23** Comparing topography and charge density for graphene on BNNS *vs.* SiO<sub>2</sub> substrates.<sup>242</sup> (a and b) The 60 nm × 60 nm STM topographs of (a) graphene/BN (tunneling current  $I_T = 0.2$  nA, bias voltage  $V_b = 0.25$  V, gate voltage  $V_g = 6$  V) and (b) graphene/SiO<sub>2</sub> ( $I_T = 0.02$  nA,  $V_b = 0.225$  V,  $V_g = 15$  V). Charge density maps obtained from conductance maps are shown for (c) graphene/BN (the same area as in (a), acquired simultaneously) and (d) graphene/SiO<sub>2</sub> (the same area as in (b), acquired simultaneously). The minima and maxima marked in the scales are the minima and maxima of the respective images. Reproduced with permission from ref. 242 (Copyright © 2011 Nature Publishing Group).

structures with lateral sizes of only a few hundred nanometers. Alternatively, Yan *et al.* reported a rather generic direct growth approach involving metal catalysts, in which bilayer graphene could be prepared on many insulating substrates including BNNSs.<sup>247</sup> While classical methods directly used Cu or Ni as the growth substrate, these authors evaporated a Ni layer on top of a thin polymer film (precursor for graphene) that was spin coated onto the insulating substrate. By heating the stacked structure in a reducing atmosphere, the polymer was decomposed and converted into bilayer graphene. The top Ni layer could be subsequently removed to expose the substrate-supported graphene.

Conversely, Liu *et al.* directly grew BNNSs onto various graphene substrates, including previously grown CVD graphene, mechanically exfoliated graphene, or HOPG (Fig. 24).<sup>248</sup> The experimental conditions were essentially the same as those previously used for BNNS grown on Cu substrates.<sup>17</sup> Raman spectroscopy data showed that after the growth of a BNNS top layer, the sample exhibited a distinctively different signal intensity profile in comparison to the original graphene substrates. Depth profiling of the stacked layers monitored by XPS confirmed that the product contained BNNS-top-graphene-bottom structures. They were distinctively different from those of the in-plane BNNS-graphene domained hybrids discussed in the previous section.<sup>207</sup> Nevertheless, the thicknesses of graphene (from CVD or mechanical exfoliation) could be controlled below 5 nm, but the BNNSs were thicker (6–20 nm as reported) under the given conditions.<sup>248</sup>

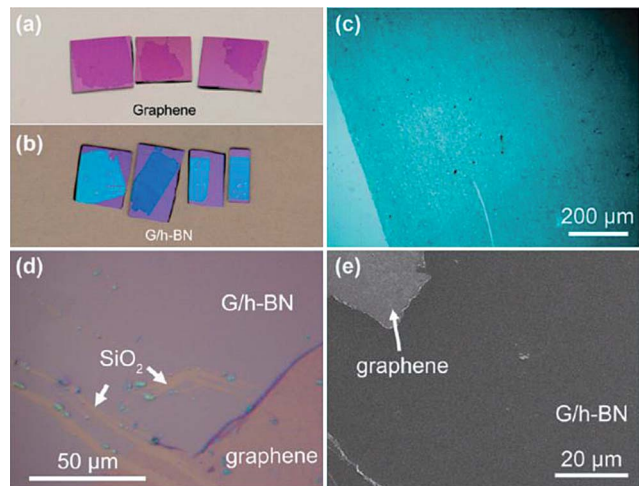


**Fig. 24** Optical and SEM images of graphene and G/h-BN (*i.e.*, graphene/BNNS) stacks that were CVD grown on Cu foils and transferred onto SiO<sub>2</sub> substrates.<sup>248</sup> (a and b) Photographs show the graphene and graphene/BNNS films on SiO<sub>2</sub> substrates. Graphene (purple), graphene/BNNS film (blue), and SiO<sub>2</sub> (light purple) are identified by different colors. (c–e) Optical and SEM images of graphene/BNNS films. The films are uniform and continuous on the substrate. Some SiO<sub>2</sub> regions are visible through an intended scratch to bare and show the graphene and graphene/BNNS regions clearly. Reproduced with permission from ref. 248 (Copyright © 2011 American Chemical Society).

A rapid hydrogen flame synthesis was reported to grow quasi-free-standing few-layered graphene on h-BN microcrystals by thermal decomposition of PMMA pre-coated on the ceramic flakes.<sup>249</sup> According to the microscopy data, however, the graphene layers obtained by this technique were crumpled and did not form flat facial contact with the h-BN substrate despite tight anchoring.

**5.2.2. BN–G heterolayers for graphene electronic devices.** Graphene FET devices using BNNS substrates exhibited much higher carrier mobility values and lower inhomogeneity than those that used SiO<sub>2</sub> substrates. For example, a monolayer graphene device from mechanical exfoliation and transfer onto BNNS substrates exhibited mobility as high as  $\sim 60\ 000\ \text{cm}^2\ \text{V}^{-1}\ \text{s}^{-1}$ .<sup>242</sup> CVD graphene-based FET devices with BNNS substrates also showed much enhanced performance when compared to ones on SiO<sub>2</sub> substrates (Fig. 25).<sup>244</sup>

Multilayer BNNS-graphene heterostructures, especially those with “sandwich” configurations, have received much recent attention. For example, a BNNS-graphene-BNNS sandwich device from mechanical exfoliation and dry transferring showed extraordinary mobility enhancement.<sup>155</sup> The mobility and mean free path values were as high as  $\sim 500\ 000\ \text{cm}^2\ \text{V}^{-1}\ \text{s}^{-1}$  and over 3  $\mu\text{m}$ , respectively. For the originally reported graphene devices on SiO<sub>2</sub> substrates at similar carrier concentrations ( $10^{12}\ \text{cm}^{-2}$ ), the values were  $\sim 10\ 000\ \text{cm}^2\ \text{V}^{-1}\ \text{s}^{-1}$  and 100 nm, respectively.<sup>5</sup> The longitudinal conductivity was limited by the graphene width, rather than scattering into the bulk as observed previously with other dielectric substrates.

The use of BNNSs as dielectric substrates as in the examples above usually requires an extreme flatness with a sufficiently

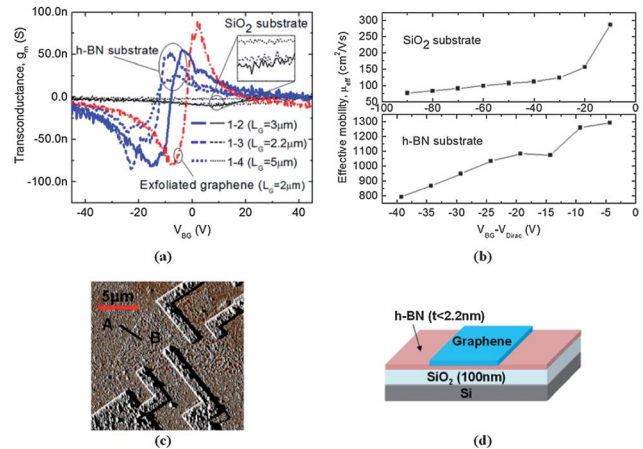


**Fig. 25** FET devices using CVD graphene on BNNS.<sup>244</sup> (a) Small-signal transconductances of the FETs with CVD-graphene on BNNS (blue) and SiO<sub>2</sub> substrates (black). The plot with exfoliated graphene on SiO<sub>2</sub> is also shown for comparison (red). (b) Extracted effective mobility of the FET devices with CVD-graphene on SiO<sub>2</sub> (top) and BNNS (bottom). (c) AFM image of a graphene FET device on BNNS showing that the BNNS thickness is  $\sim 2.2$  nm along the A–B line. (d) Schematic of the graphene FET device on BNNS. Reproduced with permission from ref. 244 (Copyright © 2011 American Institute of Physics).

large area, but does not impose a stringent requirement on the nanosheet thicknesses. However, the control of layer numbers of BNNSs becomes more critical when they are used in field-effect tunneling transistors,<sup>250</sup> another distinct type of device configuration based on BN–G heterolayers. This type of device takes advantage of the insulating nature of BNNSs coupled with their atomic thicknesses, which allows 2D electron gas coupling<sup>251</sup> and current tunnelling<sup>252</sup> between two graphene layers separated by a thin BNNS. In one such field-effect tunneling transistor shown very recently,<sup>250</sup> BNNSs were used as a vertical transport barrier in a sandwich configuration between two graphene electrodes, allowing the tunneling current to penetrate through (Fig. 26). It should be noted that the top graphene layer may also be replaced by a metal such as Cu.<sup>253</sup> While thick BNNSs were usually prone to electrical breakdown, devices with an appropriate number of BNNS layers (*i.e.*, 4–7 layers) showed low conductivity at zero-bias and a strong dependence of the tunneling current on the gate voltage. At a sufficiently large gate voltage, the on/off ratio could be over  $10^4$ , 10 times higher than graphene-based classical planar FETs. Also, importantly, the path of current through the thickness of the BNNS separation layer is only nanometers long in these vertical FET devices as compared to sub-micrometer in conventional configurations, thus providing a much faster electron transit time – only a few femtoseconds. Further thinning of the layer numbers resulted in an exponential increase of the tunneling current, typical for a quantum tunneling effect.<sup>67,250</sup>

**5.2.3. Electronic modulation of graphene in BN–G heterolayers.** In addition to the carrier mobility enhancement, it was predicted that another benefit to using BNNS as the dielectric substrate is the opening of a bandgap by the order of 50 meV at the graphene Dirac point.<sup>153</sup> Although the most stable configuration for graphene–BNNS stacking would be graphene C atoms

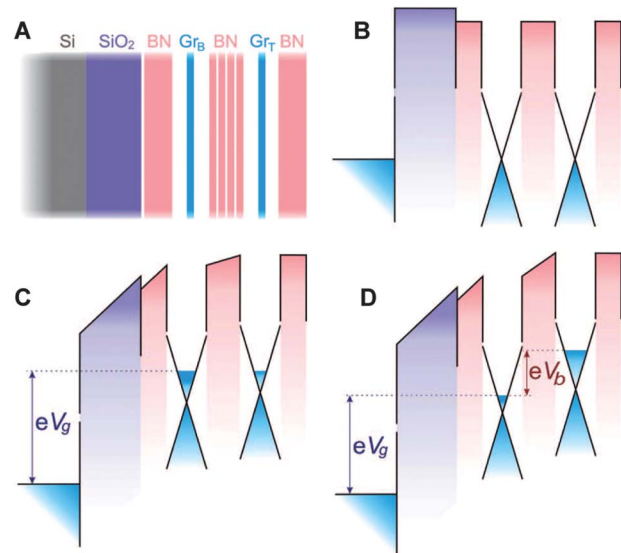


**Fig. 26** Graphene field-effect tunneling transistor with a few-layered BNNS as the tunneling barrier.<sup>250</sup> (A) Schematic structure of the experimental devices. The graphene–BNNS–graphene sandwich structure was encapsulated within two thick h-BN crystals for higher graphene electrode performance. SiO<sub>2</sub> substrate (300 nm thick, an oxidized Si wafer) was the gate electrode. In the most basic version of the FET, only one graphene electrode (Gr<sub>B</sub>) is essential, and the outside electrode (Gr<sub>T</sub>) can be made from a metal. (B) The corresponding band structure with no gate voltage applied. (C) The same band structure for a finite gate voltage  $V_g$  and zero bias  $V_b$ . (D) Both  $V_g$  and  $V_b$  are finite. The cones illustrate graphene's Dirac-like spectrum and, for simplicity, the tunnel barrier for electrons is considered. Reproduced with permission from ref. 250 (Copyright © 2012 American Association for the Advancement of Science).

alternatively sitting on top of B atoms and borazine ring of the BNNS, other stacking orders (*e.g.*, C above B and N; C above N and borazine ring) may also induce a similar bandgap opening.<sup>153</sup> Other theoretical studies suggested that the bandgap of the graphene top layer could be further tuned in a larger range by application of transverse electric field<sup>254</sup> or in-plane strain<sup>255</sup> to the heterobilayer. By introducing finite masses of Dirac fermions, graphene transistor devices with such bandgaps could have large on/off ratios.<sup>254</sup>

However, a common experimental observation was that no bandgap opening was induced<sup>154,242,248</sup> even for the graphene–BNNS hybrid layers with 0° rotation angle – supposedly the best possible structural matching.<sup>248</sup> There was also a report on using an Au intercalation approach to relieve the planar strain of the BNNS layer from the Ni(111)/W(110) substrate.<sup>256</sup> Still, no bandgap opening was found for the subsequently grown graphene layer. Most theoretical models used perfectly stacked systems, which induced a symmetry breaking effect leading to bandgap opening. Xue *et al.* suggested that it could be that the lattice mismatch between graphene and BNNSs in actual systems, although as small as 1.8%, was sufficient enough to neutralize the symmetry breaking.<sup>242</sup>

Nevertheless, chemically modifying the graphene layer or the entire layered structure<sup>257,258</sup> or applying an electric field<sup>258,259</sup> might be more robust options for electronic modulation of graphene in BN–G heterolayer architectures. For example,

hydrogenation of graphene with the BNNS substrate reduced the bandgap value due to polarization effects.<sup>257</sup> Fluorination of BNNS-graphene-BNNS multilayers might result in hybrid cubic BN-diamond films with  $sp^3$  hybridization throughout the structures.<sup>258</sup> The bandgap of such structures could be tuned by either controlling the BN/C ratio and film thickness or applying an external electric field. Bandgap opening of unfunctionalized graphene in sandwich structures was also investigated, with some arguments on whether the bandgap is sensitive to the transverse electric field.<sup>260–262</sup> It does appear that the stacking orders of the sandwich structures strongly affect the bandgap sensitivity to the external field, as some configurations are insensitive but some others are tunable by 0.30 eV.<sup>262</sup> In comparison to monolayer graphene systems, bilayer graphene sandwiched between BNNS layers is much less affected by stacking disorders and thus could be a more practical choice in bandgap engineering.<sup>261</sup>

Experimentally, the rotation angle between graphene and BNNS layers seems to be always random from either direct CVD growth or post-growth stacking. However, the two types of layer surfaces can still be well conformed to each other and exhibit various Moiré patterns as revealed by STM imaging (Fig. 27a–c),<sup>242</sup> consistent with results from first principle calculations.<sup>263</sup> Most of the previous studies have focused on devices with low or zero graphene–BNNS rotational angle at low energies near the graphene Dirac point. Very recently, it has been found that the rotational graphene–BNNS surface conformation could induce periodic potentials for charge carriers, resulting in superlattice Dirac points in addition to those for graphene itself.<sup>264</sup> These new Dirac points showed as asymmetric dips in

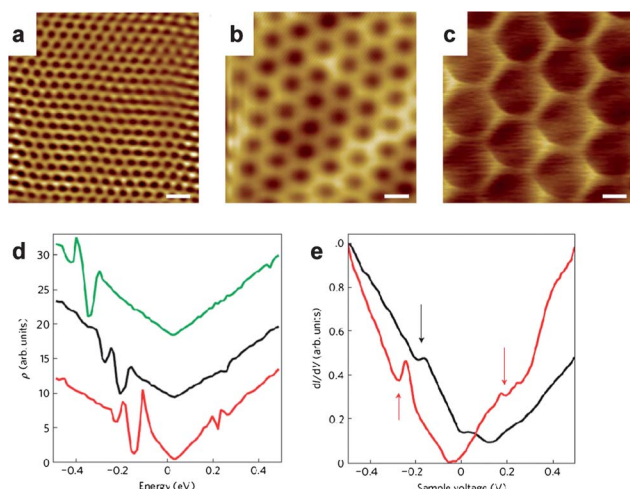


**Fig. 27** Rotational graphene–BNNS stacking and the induced superlattice Dirac points. STM topographic images showing Moiré patterns with a periodicity (or Moiré wavelength) of 2.4 (a), 6.0 (b), and 11.5 nm (c), respectively (scale bars = 5 nm) as a result of a decrease in the rotation angle between graphene and BNNS.<sup>242</sup> (d) Theoretical LDOS curves for three different rotation angles between graphene and BNNS: red: 0.5° (corresponding Moiré wavelength is 12.5 nm), blue: 1° (10.0 nm) and green: 2° (6.3 nm). The curves have been vertically offset for clarity.<sup>264</sup> (e) Experimental  $dI/dV$  curves for two different Moiré wavelengths, 9.0 nm (black) and 13.4 nm (red).<sup>264</sup> The dips in the curves are marked by arrows. Reproduced with permission from ref. 242 (Copyright © 2011 American Chemical Society) and ref. 264 (Copyright © 2012 Nature Publishing Group), respectively.

the local density of states (LDOS) on both sides of the original Dirac point, with the one on the valence band side being much deeper (Fig. 27d and e). The energy distance between the new and the original Dirac points shortens with the increase of rotation angle, which could be calculated by the periodicity of the Moiré patterns. The discovery of such superlattice Dirac points in graphene–BNNS heterolayers opens up new avenues for manipulation of electronic performance of such devices.

## 6. Applications beyond graphene electronics

The unique combination of electronic, mechanical, thermal, and chemical properties of 2D BN nanomaterials has allowed them to be used in various applications. In previous sections, we briefly mentioned some applications of different forms of 2D BN nanomaterials such as BNNMs, BNNRs, and BCN hybrid nanosheets. For example, the periodic topographic mesh structure of BNNMs could be used as a template to form ordered arrays of organic molecules or nanoparticles.<sup>164,167,168,185–189</sup> BCN hybrid nanosheets could be used not only in electronic devices with controlled bandgaps or conductivity<sup>207,211</sup> but also fuel cells.<sup>212</sup> Both BN and BCN nanoribbons for transistors and spintronics remain unexplored experimentally, though many theoretical investigations have already implicated significant potential.

As discussed in much detail in the previous section, the most unique and important applications for BNNSs are their uses as either dielectric substrates<sup>154,155,242,244</sup> or ultrathin dielectric separation layers<sup>264</sup> in *graphene electronic devices*, which are the major driving force for CVD production of large area BNNSs. There are also some applications of these nanosheets that take advantage of other properties and do not specifically require or need samples from large area epitaxial growth. These applications include the use of BNNSs as multifunctional composite fillers, robust catalytic<sup>200</sup> and sensing substrates<sup>57</sup> that are resistant to heat and oxidation, highly durable field emission devices, superhydrophobic surfaces for self-cleaning,<sup>136,194</sup> etc. Some of these are highlighted below.

### 6.1. Multifunctional composite fillers

BNNSs can be excellent fillers for high performance polymeric composites. These nanosheets are almost as strong and thermally conductive as graphene and have better thermal stability and oxidation resistance. Unlike the usually conductive carbon-based composites, the BNNS-filled composites may inherit the insulating properties of the polymer matrix. In addition, BNNSs do not absorb in the visible region and thus have much less impact on the optical transmission of the polymer matrix than do highly absorptive carbon fillers. Although BNNS-filled composite films are usually transparent at low nanosheet loadings, they do appear white at higher contents due to the strong scattering of the nanosheets with lateral sizes larger than the visible wavelengths as discussed in Section 3.1.

It should be noted that thick h-BN microcrystals have been used as composite fillers for decades for mechanical, thermal and optical enhancements.<sup>265</sup> However, the use of nanosheet fillers resulted in composite properties that are either superior to those

with h-BN fillers or need much less loading to achieve the same performance, as in the case of graphene vs. graphite fillers.<sup>266</sup>

In order to be used as polymeric composite fillers, BNNSs need to be obtained in reasonable scale (minimally milligram quantities). They are also preferably dispersible in common solvents so that conventional solution processing methods can be applied in composite fabrication. Therefore, BNNSs obtained from solvent dispersion and chemical functionalization methods (Sections 4.1.2. and 4.1.3.) are the best candidates.

For example, BNNSs from DMF and MSA exfoliation and dispersion were incorporated into PMMA (a well known commodity polymer often used as “organic glass”)<sup>15</sup> and also poly[2,2'-(*p*-oxydiphenylene)-5,5'-bibenzimidazole] (OPBI, a high-temperature polymer that is also oxidation resistant)<sup>133</sup> via facile solution processing methods. While both polymers are transparent by themselves, their light transmission properties did not change significantly. An example of a BNNS–OPBI film is shown in Fig. 28a. The use of pristine h-BN powder in the same amount, however, made the composite opaque (also shown in Fig. 28a).<sup>133</sup> The difference was attributed to the much reduced thickness of the exfoliated nanosheets in comparison to the parent microcrystals. The composites showed improved tensile strength and modulus in comparison to the neat polymers (Fig. 28b). The enhancement was comparable to that with graphene fillers.<sup>133</sup>

While graphene fillers have shown promise in significantly improving thermal transport properties of polymer composites,<sup>267</sup> the use of BNNS fillers for the same purpose is intriguing as it provides an alternative option for thermal management without imparting electrical conductivity. By using large quantities of exfoliated few-layered BNNS fillers from an IPA suspension, Song *et al.* recorded in-plane thermal diffusivity values as high as  $19 \text{ mm}^2 \text{ s}^{-1}$  (equivalent to a thermal conductivity of  $\sim 30 \text{ W m}^{-1} \text{ K}^{-1}$ ) for epoxy films embedded with 50

vol% of BNNSs.<sup>113</sup> The thermal transport properties of the composites were strongly dependent on the matrix used, as a poly(vinyl alcohol) matrix with the same 50 vol% filler loading had a much lower thermal diffusivity value ( $\sim 6 \text{ mm}^2 \text{ s}^{-1}$ ) (Fig. 28c). Furthermore, alignment of the BNNS fillers *via* stretching of the polymer films could also significantly enhance the in-plane thermal transport properties of the composite in the filler alignment direction.

Chemically functionalized BNNSs were also used for composite fabrication. Yu *et al.* incorporated exfoliated BNNSs with ODA or hyperbranched aromatic polyimide functionalities into an epoxy matrix.<sup>112</sup> The resultant composites showed improved mechanical properties. In addition, the thermal conductivity of the composites increased by  $\sim 20$  to 30% with only 5 wt% loading. The composites with polyimide-functionalized BNNS fillers exhibited better mechanical and thermal properties than those with ODA-functionalized BNNS fillers, while those containing BNNSs with no functionalities (from DMF dispersion) exhibited the least performance enhancement. The differences exemplified the importance of the presence of nanosheet-attached bulky functional groups, which may interact with the matrix molecules more strongly than bare nanosheets, thus improving the interfacial compatibility between the matrix and the nanosheet fillers.

Kiran *et al.* incorporated trioctylamine-functionalized BNNSs into a PMMA matrix *via* solution mixing.<sup>268</sup> The preparation process of the starting BNNSs<sup>147</sup> had allowed the facile control of the nanosheet layer numbers by varying the precursor ratio (boric acid : urea) (also see Section 4.2.3.). Interestingly, it was observed that the mechanical properties of PMMA composites in terms of hardness and modulus increased with fewer layers of nanosheet fillers at the same loading level. This was attributed to the enhanced matrix–filler interactions due to larger surface area for fewer-layered BNNSs.

It was commonly observed that BNNS fillers increased the glass transition temperature ( $T_g$ ) of the polymer composites due to the decrease of the polymer chain mobility as a result of the filler incorporation.<sup>15,112</sup> The use of bulky functional groups may further induce  $T_g$  increases due to stronger polymer mobility limitations.<sup>112</sup> Such a mobility change might have also resulted in a significantly reduced thermal expansion coefficient even with a very low nanosheet loading level.<sup>15</sup>

The thermally conductive but electrically insulating behavior of BNNSs may also be transferrable as fillers to heat transfer fluids. As Taha-Tijerina *et al.* very recently reported, BNNSs from exfoliation–dispersion with IPA were re-dispersed in mineral oil, a common heat transfer fluid for transformers.<sup>269</sup> Mineral oil with only 0.1 wt% stably dispersed BNNSs exhibited a significant thermal conductivity enhancement of 80–100% at 100 °C in comparison to the neat fluid. While the use of graphene as fillers reduced the electrical resistivity of mineral oil, BNNSs retained or even slightly increased the resistivity value as a result of their insulating nature.

## 6.2. Unique substrate for catalytic and sensing applications

Nanoscale substrates, such as nanotubes, nanowires, and nanosheets, often provide synergistic effects to enhance the performance of the supported nanoparticles in hierarchical nanohybrid

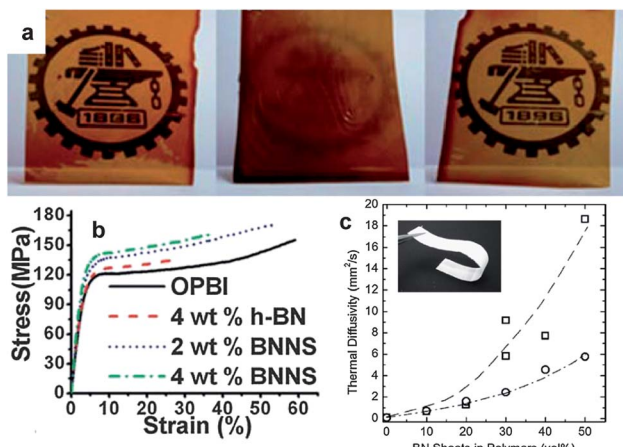


**Fig. 28** Polymeric composites using BNNS fillers. (a) Photographs showing a pure OPBI film (left) and composite films with 4 wt% pristine h-BN (middle) and MSA-exfoliated BNNSs (right).<sup>133</sup> (b) Typical stress–strain curves of OPBI and composites based on either pristine h-BN or MSA-exfoliated BNNSs.<sup>133</sup> (c) Thermal diffusivity values as a function of BNNS loading for epoxy (□) and PVA (○) composite films.<sup>113</sup> The inset is a photo of a piece of epoxy film with 50 vol% BNNS loading. Reproduced with permission from ref. 133 (Copyright © 2011 Royal Society of Chemistry) and ref. 113 (Copyright © 2012 Wiley-VCH).

materials in a variety of applications.<sup>270</sup> The unique properties of BNNSs make them also attractive as substrate supports for nanoparticles. An example of the synergistic effect provided by BNNS substrates was shown in a recent theoretical study, which suggested that atomic Au clusters attached to either pristine or defective BNNSs exhibited enhanced O<sub>2</sub> adsorption.<sup>271</sup> In addition, the intrinsic localized polarity in BNNS structures may promote the charge transfer between Au and O<sub>2</sub> even with a defect-free nanosheet support, resulting in enhanced catalytic activity of the supported Au clusters.

In an experimental study, BNNSs with corrugated surfaces but high surface area (226 m<sup>2</sup> g<sup>-1</sup>) from a gram-scale solid-state synthetic process were used to support Pt and Au nanoparticles.<sup>200</sup> These nanoparticles were deposited *via* reduction of the corresponding metal salts in the presence of BNNSs. The thermal and oxidation stability of BNNSs enabled the metal-BNNS nanohybrids to function as excellent reliable catalytic systems for CO conversion/removal *via* gaseous oxidation. Pt nanoparticles supported on these corrugated high surface area BNNSs performed better in terms of conversion temperature reduction than those supported on many other substrates (*e.g.* Al<sub>2</sub>O<sub>3</sub>, CeO<sub>2</sub>).

We recently took advantage of the impurity-free surface of water-exfoliated BNNSs<sup>21</sup> for facile anchoring of Ag nanoparticles in homogeneous aqueous dispersion (Fig. 29a).<sup>57</sup> As in the example above, the Ag nanoparticles were formed *in situ* *via* the reduction of a Ag salt in the presence of BNNSs. Results

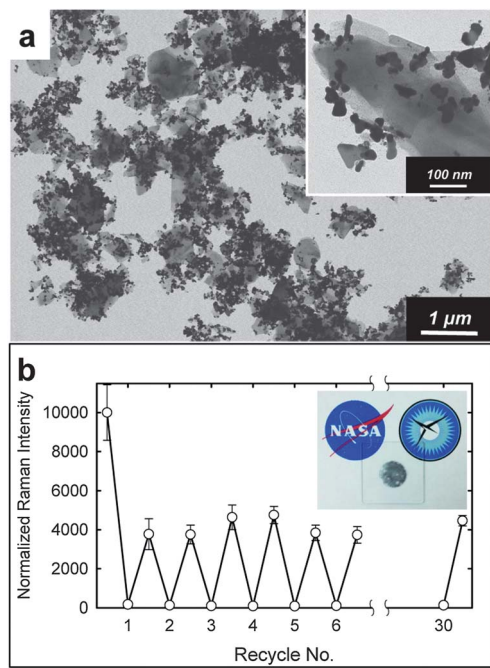


**Fig. 29** Ag–BNNS nanohybrids for reusable SERS devices.<sup>57</sup> (a) A TEM image of the Ag–BNNS hybrids from aqueous dispersion. The inset shows a higher magnification image of a nanosheet with a surface decorated with Ag nanoparticles. (b) SERS responses (traced by the peak signal at 610 cm<sup>-1</sup>) of a Ag–BNNS sensor device on quartz toward a Rhodamine 6G solution (10<sup>-4</sup> M in ethanol) during repeated measurement–thermal oxidation cycles. Each thermal oxidation treatment was carried out at 400 °C in air for 2 min. The inset shows a picture of an as-prepared device.

showed that the noble metal nanoparticles were grown on BNNSs using the nanosheets as templates and thus robustly anchored. The Ag–BNNS hybrid products remained dispersible in water, allowing facile subsequent processing *via* filtration and transferring onto a quartz substrate for surface enhanced Raman spectroscopy (SERS) measurements. The quartz-supported Ag–BNNS film devices thus prepared were robust against solvent washing in repeated measurements and had high SERS sensitivity. The device performance in terms of the enhancement factor was comparable with those reported for Ag–graphene hybrids. More importantly, the thermal and oxidation stability of BNNS supports allowed the convenient recycling of the SERS devices *via* annealing at 400 °C in air for a short period to completely remove the residual analyte molecules from previous runs. One of such devices was recycled as many as 30 times with repeatable stable performance (Fig. 29b).

In addition to the *in situ* reduction methods discussed above, the preparation of BNNS-supported nanoparticles may borrow many other successful approaches from the use of substrates such as graphene and carbon nanotubes.<sup>270</sup> For example, we have recently developed a few general routes to deposit metal or metal oxide nanoparticles onto nanocarbon and other substrates including 2D BN nanostructures under solvent-free conditions.<sup>272–274</sup> In these processes, precursor organic metal salts were mixed with substrate materials such as h-BN in solid-state and directly subjected to thermal treatment *via* conventional oven heating,<sup>272</sup> mechanochemical agitation (*i.e.*, ball-milling),<sup>273</sup> or microwave heating.<sup>274</sup> Despite the efficiency difference among these heating methods, the metal salt decomposed, forming metal or metal oxide particles that were anchored onto the substrate surface. These approaches are highly versatile and scalable, and applicable to the formation of a variety of metal or metal oxide nanoparticles.

Another general route to prepare metal–BNNS hybrid materials is atomic layer deposition (ALD). ALD was previously shown to be effective to deposit Al<sub>2</sub>O<sub>3</sub> onto a graphene surface.<sup>275</sup> Recently, Liu *et al.* used a similar method to deposit the same high- $\kappa$  (*i.e.*, dielectric constant) dielectric metal oxide onto BNNSs and exfoliated MoS<sub>2</sub> nanosheets alike.<sup>276</sup>

### 6.3. Vertical BNNS edges as field emitters

It is desirable for field-emission devices to have low turn-on voltages but high emission currents and durability. The mechanical strength, thermal conductivity, and thermal/oxidation inertness of BNNSs would make them viable candidates as durable field emitters under suitable conditions if deficiencies from their large bandgap could be overcome.

The edges of BNNSs are usually the electron emitting sites and thus should be exposed during field emission, making the nanosheets from vertical growth techniques one of the preferable choices (see Section 4.2.3.). However, vertically grown BNNSs on Si wafers were usually quite thick. This appeared detrimental to the field emission due likely to the insulating nature of BNNSs.<sup>194</sup> Films thicker than 3 μm did not exhibit any field emission, while those with thicknesses of 1–2 μm required very high turn-on voltages (~44 V μm<sup>-1</sup>) and gave low current density (0.072 μA cm<sup>-2</sup>). In comparison, BNNSs protruding from micro- or nanoscale substrates such as Si<sub>3</sub>N<sub>4</sub> nanowires<sup>197</sup> and

BN fibers,<sup>198</sup> both with nanosheet heights on the order of only 200 nm or less, showed much lower turn-on voltages of 4.2 and 1.9 V  $\mu\text{m}^{-1}$ , respectively. These devices showed excellent long-term stability with little or no current reduction for over 10 h. In a related report, Terrones *et al.*<sup>277</sup> prepared porous BN nanospheres from porous carbon templates in a C-to-BN conversion/substitution reaction (similar to the reaction used for BNNS preparation,<sup>202</sup> see Section 4.2.3.). The surface of each nanosphere consisted of thousands of nanosheet edges. With high current stability in field emission, the turn-on voltage for this material was as low as 1–1.3 V  $\mu\text{m}^{-1}$ . The authors attributed the low value to the metallic behavior of zigzag BNNS edges.<sup>277</sup>

It is worth mentioning that depositing metal nanoparticles on BNNTs has significantly enhanced the field emission properties of insulating nanotubes.<sup>278</sup> A similar strategy may potentially be adapted to help optimize the turn-on voltage of BNNS edges from various growth techniques.

## 7. Summary and perspectives

In this article, we have reviewed the current status of the research on 2D BN nanostructures: their structural characteristics, properties, preparations, and applications. Although the main period covered is only a short 8 year period from 2004 to the time of this review (mid-2012), there has been significant growth of this field with many breakthroughs occurring in the last three to four years.

2D BN nanostructures are derivatives of h-BN, which are typically identified by their thicknesses (*e.g.*, few-layered *vs.* monolayer BNNSs), aspect ratios (*e.g.*, BNNRs), surface topography (*e.g.*, “BNNMs”), edge types (*e.g.*, zigzag *vs.* armchair), and morphology (*e.g.*, vertically grown BNNSs). As the isoelectric analog of graphene materials, 2D BN nanostructures (or BNNSs in a more general definition) share many similar properties but do have distinct differences such as the stacking order, large bandgap (insulating “white graphenes”), geometrically well-defined defect morphologies, *etc.*

Various microscopic techniques including TEM, AFM, and even optical microscopy have been used to characterize BNNSs from their precise atomic structures to both nanoscopic and microscopic morphologies such as layer number and surface topography. There are also many spectroscopic signatures for BNNSs, such as those in optical absorption, FT-IR, Raman, XPS, XRD, *etc.*, allowing one to identify their bandgap, structural integrity, chemical bonding, and even layer number information. It should be noted that Raman spectroscopy has proven to be quite convenient in defect characterizations of  $\text{sp}^2$  carbon allotropes, but much less useful for the same purpose on 2D BN nanostructures. A reliable spectroscopic defect quantification method is yet to be established.

Both top-down (*e.g.* mechanical exfoliation, solvent exfoliation, or chemical functionalization) and bottom-up (*e.g.* epitaxial CVD) methods to prepare BNNSs are under rapid development. It should be acknowledged that a large portion of the current surge of interest in BNNSs remains in their potential applications in graphene electronics as shown recently by a few very promising studies. For these applications, it is important to use high crystalline quality BNNSs with controllable thickness and large lateral area. As a result, the famous “Scotch tape method”

is still being actively used by many researchers for device fabrication since high quality h-BN single crystals have become available as the starting material to be peeled from. Initial successes in epitaxial CVD growth of BNNSs are providing useful alternatives with more controllable lateral area and layer thicknesses although many improvements remain to be made.

Compared to the Scotch tape method, most other top-down approaches involve the use of solvents and are amenable to preparing larger quantities (milligram scale and above) of BNNSs with a distribution of sizes and thicknesses. Many polar organic solvents and even water can directly exfoliate h-BN starting materials with the assistance of sonication, resulting in dispersed BNNSs down to the monolayer level. These BNNSs are impurity-free (*i.e.*, no surfactants or functional groups) and solution-processible, which may enable applications *via* further surface treatments such as conjugation with biomolecules or decoration with metal nanoparticles in homogeneous dispersions.

h-BN can be functionalized using noncovalent, ionic (Lewis acid–base), and covalent strategies, which also result in the exfoliation of the layered structures. Despite their oxidation inertness, the chemistry of h-BN/BNNSs is expected to be quite rich due to the intrinsically polarized nature of the nanosheets. One example would be simply tailoring the bulky group of amine compounds for Lewis acid–base complexation with BNNS surfaces. It is expected that the use of different functional groups may enable a variety of applications such as providing more compatible interfaces with different matrix polymers in multi-functional composites.

All top-down exfoliation approaches are limited by the sizes of the available starting h-BN crystals (usually less than 10  $\mu\text{m}$ ). The use of sonication in wet approaches makes the final sizes of BNNSs even smaller (typically in the range of a few hundred nm to  $\sim$ 1  $\mu\text{m}$ ). It has thus been challenging to use these latter materials for electronic applications.

BNNRs and BNNMs are special forms of BNNSs. While the edge effect is negligible in BNNSs of large enough lateral sizes, BNNRs are those with narrow widths (preferably a few nanometers or less) so that the electronic and magnetic properties are significantly affected by the edge atoms. For example, theoretical studies suggest that BNNRs of certain structural or functional group characteristics may become half-metals although typical BNNSs are insulators. However, only a couple of methods are available to experimentally prepare BNNRs in small quantities. Both methods involve longitudinal “unzipping” of BNNT precursors. Much synthetic development is apparently needed, for which many strategies and concepts might continue to be borrowed from the more mature fabrication of graphene nanoribbons.

When initially discovered, BNNMs from ultrahigh vacuum CVD growth on Rh(111) substrates were thought to be double-layered BNNSs with periodic patterns of pores. However, subsequent investigations showed that the “pores” were actually shallow regions of a monolayer BNNS that interacted more strongly with the metal substrate underneath. The periodicity of the “pores” or other patterns was determined by the degree of BNNS–metal lattice mismatch, with the pore formation strongly affected by the substrate–BNNS interaction strength. Therefore, the use of different growth substrates resulted in either

"BNNMs" with different pore periodicities and topographical appearances or flat nanosheets with little to no surface roughness.

Non epitaxial CVD growth resulted in BNNSs with other morphologies. For example, BNNSs were grown vertically from macroscale or nanoscale substrates. The topography of the vertically aligned BNNSs resulted in superhydrophobicity. The exposed nanosheet edges were also used for field emission purposes.

The incorporation of  $sp^2$  C (*i.e.*, graphene) domains in the BNNS structure, or *vice versa*, resulted in hybrid nanosheets with tunable electronic properties. These BNNS-graphene hybrids (or BCN nanosheets) may have broad implications in electronic devices, composites, and energy conversion and storage.

Another type of BNNS-graphene hybrid is heterolayers of the two species. Rather than a type of nanomaterial, such heterolayers are more like architectures of graphene electronic devices, with BNNSs used either as the dielectric substrates or ultrathin separation layers. The BNNS-graphene heterolayers could be prepared either by stacking of the two types of nanosheets or growth of one on the other. The predicted bandgap opening of graphene was not observed experimentally due to the lattice mismatch as well as stacking faults in actual heterolayers. Nevertheless, graphene electronic devices of various configurations that incorporate BNNSs have shown much enhanced properties in comparison to the use of conventional  $SiO_2$  substrates. Multiple BNNS-graphene stacks such as "sandwich" structures are of particular interest in both conventional and vertical FET devices as they show even more intriguing performances. Interestingly, BNNS-graphene-BNNS sandwich structures were also proposed as pressure sensors.<sup>279</sup>

Despite much theoretical effort, experimental studies of independent (*i.e.*, graphene-free) electronic and magnetic/spintronics applications of BNNSs (especially BNNRs) are rare. One of the driving forces in this direction would obviously be more well-defined, reliable, and scalable preparation methods for BNNRs as discussed above.

There are many other applications of BNNSs. For example, polymeric composites with BNNS fillers have been shown to have multiple functions such as optical transparency, mechanical reinforcement, electrical insulation, and effective heat transfer. One of the other benefits to be exploited might be radiation shielding due to the high neutron absorption cross-section of B atoms (especially the  $^{10}B$  isotope<sup>280</sup>).

There have been reports on using BNNSs for unique catalysis, sensing, and field emission applications. Most of these applications took advantage of their excellent thermal stability and oxidation resistance in combination with other properties associated with their 2D structure such as their high surface area. Other applications such as robust coatings,<sup>281</sup> hydrogen storage,<sup>282-286</sup> and ultrathin support for HR-TEM imaging<sup>287</sup> have also been discussed.

Lastly, we would like to mention that aqueous dispersibility, stable structure, rich modification chemistry, and expected low toxicity make BNNSs intriguing objects for biological applications. Modifications of BNNSs with proteins<sup>21</sup> and nucleobases<sup>144</sup> have been demonstrated experimentally and theoretically, respectively, but much remains to be explored. It is interesting to note that h-BN, the parent material of BNNSs, has

been an important component in many commercial powdery and cream cosmetics products today because of its unique combination of properties such as stability, lubrication, low-color, and thermal conductivity.<sup>288</sup>

Future work on the various forms of 2D BN nanostructures will likely continue to focus on new and improved methods for preparing single layer sheets of larger dimensions, and subsequent evaluation in a variety of applications and devices. Like all materials, the unique combination of properties offered by BNNSs must be fully understood in order to effectively integrate with other materials to take full advantage of their attributes in system level applications.

## Acknowledgements

We thank T. Williams (Langley Aerospace Research Summer Scholar) and Dr W. Cao (Old Dominion U.) for their contributions to the BNNS research. We also thank Dr Christopher Bunker (Air Force Research Laboratory), Prof. Zhongfang Chen (U. of Puerto Rico), Prof. Peter Feng (U. of Puerto Rico), Dr Shiral Fernando (University of Dayton Research Institute), Dr Jae-Woo Kim (National Institute of Aerospace), and Prof. Ya-Ping Sun (Clemson U.) for fruitful collaborations and stimulating discussions. We are grateful to Dr Jeffrey Hinkley (NASA Langley Research Center) for his helpful suggestions during the preparation of this article.

## References

- (a) R. T. Paine and C. K. Narula, *Chem. Rev.*, 1990, **90**, 73; (b) W. Schnick, *Angew. Chem., Int. Ed.*, 1993, **32**, 806.
- (a) G. Seifert, P. W. Fowler, D. Mitchell, D. Porezag and T. Frauenheim, *Chem. Phys. Lett.*, 1997, **268**, 352; (b) V. V. Pokropivny, V. V. Skorokhod, G. S. Oleinik, A. V. Kurdyumov, T. S. Bartnitskaya, A. V. Pokropivny, A. G. Sisonyuk and D. M. Sheichenko, *J. Solid State Chem.*, 2000, **154**, 214.
- (a) D. Golberg, Y. Bando, C. Tang and C. Zhi, *Adv. Mater.*, 2007, **19**, 2413; (b) C. N. R. Rao and A. Govindaraj, *Adv. Mater.*, 2009, **21**, 4208; (c) J. Wang, C. H. Lee and Y. K. Yap, *Nanoscale*, 2010, **2**, 2082; (d) D. Golberg, Y. Bando, Y. Huang, T. Terao, M. Mitome, C. Tang and C. Zhi, *ACS Nano*, 2010, **4**, 2979.
- (a) A. K. Geim and K. S. Novoselov, *Nat. Mater.*, 2007, **6**, 183; (b) D. R. Dreyer, R. S. Ruoff and C. W. Bielawski, *Angew. Chem., Int. Ed.*, 2010, **49**, 9336.
- K. S. Novoselov, A. K. Geim, S. V. Morozov, D. Jiang, Y. Zhang, S. V. Dubonos, I. V. Grigorieva and A. A. Firsov, *Science*, 2004, **306**, 666.
- (a) K. S. Novoselov, D. Jiang, F. Schedin, T. J. Booth, V. V. Khotkevich, S. V. Morozov and A. K. Geim, *Proc. Natl. Acad. Sci. U. S. A.*, 2005, **102**, 10451; (b) M. Osada and T. Sasaki, *Adv. Mater.*, 2012, **24**, 210; (c) C. N. R. Rao and A. Nag, *Eur. J. Inorg. Chem.*, 2010, 4244.
- J. N. Coleman, M. Lotya, A. O'Neill, S. D. Bergin, P. J. King, U. Khan, K. Young, A. Gaucher, S. De, R. J. Smith, I. V. Shvets, S. K. Arora, G. Stanton, H.-Y. Kim, K. Lee, G. T. Kim, G. S. Duesberg, T. Hallam, J. J. Boland, J. J. Wang, J. F. Donegan, J. C. Grunlan, G. Moriarty, A. Shmeliov, R. J. Nicholls, J. M. Perkins, E. M. Grieveson, K. Theuwissen, D. W. McComb, P. D. Nellist and V. Nicolosi, *Science*, 2011, **331**, 568.
- P. Y. Huang, C. S. Ruiz-Vargas, A. M. van der Zande, W. S. Shitney, M. P. Levendorf, J. W. Kevek, S. Garg, J. S. Alden, C. J. Hustedt, Y. Zhu, J. Park, P. L. McEuen and D. A. Muller, *Nature*, 2011, **469**, 389.
- H. Sachdev, F. Muller and S. Hufner, *Diamond Relat. Mater.*, 2010, **19**, 1027.

- 10 K. O. Obodo, R. C. Andrew and N. Chetty, *Phys. Rev. B: Condens. Matter Mater. Phys.*, 2011, **84**, 155308.
- 11 T. B. Ngwenya, A. M. Ukpong and N. Chetty, *Phys. Rev. B: Condens. Matter Mater. Phys.*, 2011, **84**, 245425.
- 12 R. C. Andrew, R. E. Mapasha, A. M. Ukpong and N. Chetty, *Phys. Rev. B: Condens. Matter Mater. Phys.*, 2012, **84**, 125428.
- 13 D. Pacilé, J. C. Meyer, C. Ö. Girit and A. Zettl, *Appl. Phys. Lett.*, 2008, **92**, 133107.
- 14 W.-Q. Han, L. Wu, Y. Zhu, K. Watanabe and T. Taniguchi, *Appl. Phys. Lett.*, 2008, **93**, 223103.
- 15 C. Zhi, Y. Bando, C. Tang, H. Kuwahara and D. Golberg, *Adv. Mater.*, 2009, **21**, 2889.
- 16 Y. Lin, T. W. Williams and J. W. Connell, *J. Phys. Chem. Lett.*, 2010, **1**, 277.
- 17 L. Song, L. Ci, H. Lu, P. B. Sorokin, C. Jin, J. Ni, A. G. Kvashnin, D. G. Kvashnin, J. Lou, B. I. Yakobson and P. M. Ajayan, *Nano Lett.*, 2010, **10**, 3209.
- 18 Y. Shi, C. Hamsen, X. Jia, K. K. Kim, A. Reina, M. Hofmann, A. L. Hsu, K. Zhang, H. Li, Z.-Y. Juang, M. S. Dresselhaus, L.-J. Li and J. Kong, *Nano Lett.*, 2010, **10**, 4134.
- 19 K. K. Kim, A. Hsu, X. Jia, S. M. Kim, Y. Shi, M. Hofmann, D. Nezich, J. F. Rodriguez-Nieva, M. Dresselhaus, T. Palacios and J. Kong, *Nano Lett.*, 2012, **12**, 161.
- 20 R. V. Gorbachev, I. Riaz, R. R. Nair, R. Jalil, L. Britnell, B. D. Belle, E. W. Hill, K. S. Novoselov, K. Watanabe, T. Taniguchi, A. K. Geim and P. Blake, *Small*, 2011, **7**, 465.
- 21 Y. Lin, T. W. Williams, T.-B. Xu, W. Cao, H. E. Elsayed-Ali and J. W. Connell, *J. Phys. Chem. C*, 2011, **115**, 2679.
- 22 C. K. Oliveira, M. J. S. Matos, M. S. C. Mazzoni, H. Chacham and B. R. A. Neves, *Nanotechnology*, 2012, **23**, 175703.
- 23 P. Blake, E. W. Hill, A. H. Castro Neto, K. S. Novoselov, D. Jiang, R. Yang, T. J. Booth and A. K. Geim, *Appl. Phys. Lett.*, 2007, **91**, 063124.
- 24 O. Hod, *J. Chem. Theory Comput.*, 2012, **8**, 1360.
- 25 N. Marom, J. Bernstein, J. Garel, A. Tkatchenko, E. Joselevich, L. Kronik and O. Hod, *Phys. Rev. Lett.*, 2010, **105**, 046801.
- 26 J. H. Warner, M. H. Rummeli, T. Gemming, B. Buchner and G. A. D. Briggs, *Nano Lett.*, 2009, **9**, 102.
- 27 J. Ma, D. Alfè, A. Michaelides and E. Wang, *Phys. Rev. B: Condens. Matter Mater. Phys.*, 2009, **80**, 033407.
- 28 C. Jin, F. Lin, K. Suenaga and S. Iijima, *Phys. Rev. Lett.*, 2009, **102**, 195505.
- 29 J. C. Meyer, A. Chuvilin, G. Algara-Siller, J. Biskupek and U. Kaiser, *NanoLett.*, 2009, **9**, 2683.
- 30 N. Alem, R. Erni, C. Kisielowski, M. D. Rossell, W. Gannett and A. Zettl, *Phys. Rev. B: Condens. Matter Mater. Phys.*, 2009, **80**, 155425.
- 31 J. H. Warner, M. H. Rümmel, A. Bachmatiuk and B. Büchner, *ACS Nano*, 2010, **4**, 1299.
- 32 J. C. Charlier, *Acc. Chem. Res.*, 2002, **35**, 1063.
- 33 F. Banhart, J. Kotakoski and A. V. Krasheninnikov, *ACS Nano*, 2011, **5**, 26.
- 34 (a) S. Azevedo, et al., *Nanotechnology*, 2007, **18**, 495707; (b) I. Jiménez, et al., *Appl. Phys. Lett.*, 1996, **68**, 2816; (c) I. Jiménez, et al., *Phys. Rev. B: Condens. Matter Mater. Phys.*, 1997, **55**, 12025; (d) W. Orellana and H. Chacham, *Phys. Rev. B: Condens. Matter Mater. Phys.*, 2001, **63**, 125205.
- 35 F.-L. Zheng, Y. Zhang, J.-M. Zhang and K.-W. Xu, *J. Mol. Struct.*, 2010, **984**, 344.
- 36 A. Zobelli, A. Gloter, C. P. Ewels, G. Seifert and C. Colliex, *Phys. Rev. B: Condens. Matter Mater. Phys.*, 2007, **75**, 245402.
- 37 S. Okada, *Phys. Rev. B: Condens. Matter Mater. Phys.*, 2009, **80**, 161404.
- 38 L.-C. Yin, H.-M. Cheng and R. Saito, *Phys. Rev. B: Condens. Matter Mater. Phys.*, 2010, **81**, 153407.
- 39 J. Kotakoski, C. H. Jin, O. Lehtinen, K. Suenaga and A. V. Krasheninnikov, *Phys. Rev. B: Condens. Matter Mater. Phys.*, 2010, **82**, 113404.
- 40 O. Lehtinen, E. Dumur, J. Kotakoski, A. V. Krasheninnikov, K. Nordlund and J. Keinonen, *Nucl. Instrum. Methods Phys. Res., Sect. B*, 2011, **269**, 1327.
- 41 A. Zhang, H. F. Teoh, Z. Dai, Y. P. Feng and C. Zhang, *Appl. Phys. Lett.*, 2011, **98**, 023105.
- 42 W. Chen, Y. Li, G. Yu, Z. Zhou and Z. Chen, *J. Chem. Theory Comput.*, 2009, **5**, 3088.
- 43 E. C. Anota, R. E. R. Gutierrez, A. E. Morales and G. H. Cocoletzi, *J. Mol. Model.*, 2012, **18**, 2175.
- 44 A. Du, Y. Chen, Z. Zhu, R. Amal, G. Q. Lu and S. C. Smith, *J. Am. Chem. Soc.*, 2009, **131**, 17354.
- 45 Y. Pan and Z. Yang, *Phys. Rev. B: Condens. Matter Mater. Phys.*, 2010, **82**, 195308.
- 46 J. Yang, D. Kim, J. Hong and X. Qian, *Surf. Sci.*, 2010, **604**, 1603.
- 47 S. Tang and Z. Cao, *Comput. Mater. Sci.*, 2010, **48**, 648.
- 48 K. Yang, Y. Chen, Y. Xie, X. L. Wei, T. Ouyang and J. Zhong, *Solid State Commun.*, 2011, **151**, 460.
- 49 K. Muralidharan, R. G. Erdmann, K. Runge and P. A. Deymier, *AIP Adv.*, 2011, **1**, 041703.
- 50 (a) S. Niyogi, M. A. Hamon, H. Hu, B. Zhao, P. Bhowmik, R. Sen, M. E. Itkis and R. C. Haddon, *Acc. Chem. Res.*, 2002, **35**, 1105; (b) Y.-P. Sun, K. Fu, Y. Lin and W. Huang, *Acc. Chem. Res.*, 2002, **35**, 1096–1104; (c) D. Tasis, N. Tagmatarchis, A. Bianco and M. Prato, *Chem. Rev.*, 2006, **106**, 1105–1136; (d) S. Banerjee, T. Hemraj-Benny and S. S. Wong, *Adv. Mater.*, 2005, **17**, 17.
- 51 Y.-H. Zhang, K.-G. Zhou, X.-C. Gou, K.-F. Xie, H.-L. Zhang and Y. Peng, *Chem. Phys. Lett.*, 2010, **484**, 266.
- 52 S. Noorizadeh and E. Shakerzadeh, *Comp. Mater. Sci.*, 2012, **56**, 122.
- 53 Y. Lin, T. W. Williams, W. Cao, H. E. Elsayed-Ali and J. W. Connell, *J. Phys. Chem. C*, 2010, **114**, 17434.
- 54 K. Watanabe, T. Taniguchi and H. Kanda, *Nat. Mater.*, 2004, **3**, 404.
- 55 Y. Kubota, K. Watanabe, O. Tsuda and T. Taniguchi, *Science*, 2007, **17**, 932.
- 56 Y. Kubota, K. Watanabe, O. Tsuda and T. Taniguchi, *Chem. Mater.*, 2008, **20**, 1661.
- 57 Y. Lin, C. E. Bunker, K. A. S. Fernando and J. W. Connell, *ACS Appl. Mater. Interfaces*, 2012, **4**, 1110.
- 58 H. Zeng, C. Zhi, Z. Zhang, X. Wei, X. Wang, W. Guo, Y. Bando and D. Golberg, *Nano Lett.*, 2010, **10**, 5049.
- 59 Y. Liu, S. Bhowmick and B. I. Yakobson, *Nano Lett.*, 2011, **11**, 3113.
- 60 Y. Hernandez, V. Nicolosi, M. Lotya, F. M. Blighe, Z. Sun, S. De, I. T. McGovern, B. Holland, M. Byrne, Y. K. Gun'Ko, J. J. Boland, P. Niraj, G. Duesberg, S. Krishnamurthy, R. Goodhue, J. Hutchison, V. Scardaci, A. C. Ferrari and J. N. Coleman, *Nat. Nanotechnol.*, 2008, **3**, 563.
- 61 (a) P. Gevko, L. Bulusheva, A. Okotrub, V. Koroteev, I. Yushina, L. Bresson and A. Loiseau, *Phys. Status Solidi B*, 2008, **245**, 2107; (b) G. Brasse, S. Maine, A. Pierret, P. Jaffrennou, B. Attal-Tretout, F. Ducaestele and A. Loiseau, *Phys. Status Solidi B*, 2010, **247**, 3076.
- 62 Y. Wang, Z. Shi and J. Yin, *J. Mater. Chem.*, 2011, **21**, 11371.
- 63 S. Reich, A. C. Ferrari, R. Arenal, A. Loiseau, I. Bello and J. Robertson, *Phys. Rev. B: Condens. Matter Mater. Phys.*, 2005, **71**, 205201.
- 64 L. H. Li, Y. Chen, G. Behan, H. Zhang, M. Petracic and A. M. Glushenkov, *J. Mater. Chem.*, 2011, **21**, 11862.
- 65 J. Kawai, S. Tadokoro, Y. Muramatsu, S. Kashiwai, H. Kohzuki, M. Motoyama, H. Kato and H. Adachi, *Physica B*, 1995, **208–209**, 251.
- 66 G.-H. Lee, Y.-J. Yu, C. Lee, C. Dean, K. L. Shepard, P. Kim and J. Hone, *Appl. Phys. Lett.*, 2011, **99**, 243114.
- 67 L. Britnell, R. V. Gorbachev, R. Jalil, B. D. Belle, F. Schedin, M. I. Katsnelson, L. Eaves, S. V. Morozov, A. S. Mayorov, N. M. R. Peres, A. H. C. Neto, J. Leist, A. K. Geim, L. A. Ponomarenko and K. S. Novoselov, *Nano Lett.*, 2012, **12**, 1707.
- 68 K. J. Erickson, A. L. Gibb, A. Sinitskii, M. Rousseas, N. Alem, J. M. Tour and A. Zettl, *Nano Lett.*, 2011, **11**, 3221.
- 69 R. Mukherjee and S. Bhowmick, *J. Chem. Theory Comput.*, 2011, **7**, 720.
- 70 M. Wu, X. Wu, Y. Pei and X. C. Zeng, *Nano Res.*, 2011, **4**, 233.
- 71 S. Wang, Q. Chen and J. Wang, *Appl. Phys. Lett.*, 2011, **99**, 063114.
- 72 A. J. Du, S. C. Smith and G. Q. Lu, *Chem. Phys. Lett.*, 2007, **447**, 181.
- 73 Z. Zhang and W. Guo, *Phys. Rev. B: Condens. Matter Mater. Phys.*, 2008, **77**, 075403.
- 74 C.-H. Park and S. G. Louie, *Nano Lett.*, 2008, **8**, 2200.
- 75 K. Zhao, M. Zhao, Z. Wang and Y. Fan, *Physica E*, 2010, **43**, 440.
- 76 Y. Ding, Y. Wang, S. Shi and W. Tang, *J. Phys. Chem. C*, 2011, **115**, 5334.

- 77 Y. Wang, Y. Ding and J. Ni, *J. Phys. Chem. C*, 2012, **116**, 5995.
- 78 F. Zheng, Z. Liu, J. Wu, W. Duan and B.-L. Gu, *Phys. Rev. B: Condens. Matter Mater. Phys.*, 2008, **78**, 085423.
- 79 Z. Yang and J. Ni, *J. Appl. Phys.*, 2010, **107**, 104301.
- 80 J. Li, G. Gui and J. Zhong, *J. Appl. Phys.*, 2008, **104**, 094311.
- 81 J. Qi, X. Qian, L. Qi, J. Feng, D. Shi and J. Li, *Nano Lett.*, 2012, **12**, 1224.
- 82 A. Bhattacharya, S. Bhattacharya and G. P. Das, *Phys. Rev. B: Condens. Matter Mater. Phys.*, 2011, **84**, 075454.
- 83 M. L. Hu, J. L. Yin, C. X. Zhang, Z. Yu and L. Z. Sun, *J. Appl. Phys.*, 2011, **109**, 073708.
- 84 V. Barone and J. E. Peralta, *Nano Lett.*, 2008, **8**, 2210.
- 85 M. Wu, Z. Zhang and X. C. Zeng, *Appl. Phys. Lett.*, 2010, **97**, 093109.
- 86 S. Dutta, A. K. Manna and S. K. Pati, *Phys. Rev. Lett.*, 2009, **102**, 096601.
- 87 S. Tang and Z. Cao, *Phys. Chem. Chem. Phys.*, 2010, **12**, 2313.
- 88 F. Zheng, G. Zhou, Z. Liu, J. Wu, W. Duan, B.-L. Gu and S. B. Zhang, *Phys. Rev. B: Condens. Matter Mater. Phys.*, 2008, **78**, 205415.
- 89 Y. Ding, Y. Wang and J. Ni, *Appl. Phys. Lett.*, 2009, **94**, 233107.
- 90 M. Topsakal, E. Aktürk and S. Ciraci, *Phys. Rev. B: Condens. Matter Mater. Phys.*, 2009, **79**, 115442.
- 91 L. Lai, J. Lu, L. Wang, G. Luo, J. Zhou, R. Qin, Z. Gao and W. N. Mei, *J. Phys. Chem. C*, 2009, **113**, 2273.
- 92 E. Kan, F. Wu, H. Xiang, J. Yang and M.-H. Whangbo, *J. Phys. Chem. C*, 2011, **115**, 17252.
- 93 F.-L. Zheng, Y. Zhang, J.-M. Zhang and K.-W. Xu, *J. Phys. Chem. Solids*, 2011, **72**, 256.
- 94 W. Chen, Y. Li, G. Yu, C. Z. Li, S. B. Zhang, Z. Zhou and Z. Chen, *J. Am. Chem. Soc.*, 2010, **132**, 1699.
- 95 S. Tang and Z. Cao, *Chem. Phys. Lett.*, 2010, **488**, 67.
- 96 D. K. Samarakoon and X.-Q. Wang, *Appl. Phys. Lett.*, 2012, **100**, 103107.
- 97 H. X. Zhang and P. X. Feng, *ACS Appl. Mater. Interfaces*, 2012, **4**, 30.
- 98 Z. Zhang, X. C. Zeng and W. Guo, *J. Am. Chem. Soc.*, 2011, **133**, 14831.
- 99 Y. Wang, Y. Ding and J. Ni, *Phys. Rev. B: Condens. Matter Mater. Phys.*, 2010, **81**, 193407.
- 100 Z. Zhang and W. Guo, *J. Phys. Chem. Lett.*, 2011, **2**, 2168.
- 101 A. Lopez-Bezanilla, J. Huang, H. Terrones and B. G. Sumpter, *Nano Lett.*, 2011, **11**, 3267.
- 102 X.-J. Wu, M.-H. Wu and X. C. Zeng, *Front. Phys. China*, 2009, **4**, 367.
- 103 D.-B. Lu, Y.-L. Song, Y. Tian, H.-R. Xu and Z.-W. Lu, *Comput. Theor. Chem.*, 2012, **979**, 49.
- 104 A. Bhattacharya, S. Bhattacharya and G. P. Das, *Phys. Rev. B: Condens. Matter Mater. Phys.*, 2012, **85**, 035415.
- 105 Y. Wang, Y. Ding and J. Ni, *Appl. Phys. Lett.*, 2011, **99**, 053123.
- 106 Q. Tang, Z. Zhou and Z. Chen, *J. Phys. Chem. C*, 2011, **115**, 18531.
- 107 J.-X. Zhao, Y.-Y. Yu, Y. Bai, B. Lu and B.-X. Wang, *J. Mater. Chem.*, 2012, **22**, 9343.
- 108 T. Ouyang, Y. Chen, Y. Xie, K. Yang, Z. Bao and J. Zhong, *Nanotechnology*, 2010, **21**, 245701.
- 109 C. Sevik, A. Kinaci, J. B. Haskins and T. Cagin, *Phys. Rev. B: Condens. Matter Mater. Phys.*, 2011, **84**, 085409.
- 110 L. Lindsay and D. A. Broido, *Phys. Rev. B: Condens. Matter Mater. Phys.*, 2011, **84**, 155421.
- 111 L. Lindsay and D. A. Broido, *Phys. Rev. B: Condens. Matter Mater. Phys.*, 2012, **85**, 035436.
- 112 J. Yu, X. Huang, C. Wu, X. Wu, G. Wang and P. Jiang, *Polymer*, 2012, **53**, 471.
- 113 W.-L. Song, P. Wang, L. Cao, A. Anderson, M. J. Meziani, A. J. Farr and Y.-P. Sun, *Angew. Chem., Int. Ed.*, 2012, **51**, 6498.
- 114 C. Lee, X. Wei, J. W. Kysar and J. Hone, *Science*, 2008, **321**, 385.
- 115 A. Bosak, J. Serrano, M. Krisch, K. Watanabe, T. Taniguchi and H. Kanda, *Phys. Rev. B: Condens. Matter Mater. Phys.*, 2006, **73**, 041402.
- 116 H. Sahin, S. Cahangirov, M. Topsakal, E. Bekaroglu, E. Akturk, R. T. Senger and S. Ciraci, *Phys. Rev. B: Condens. Matter Mater. Phys.*, 2009, **80**, 155453.
- 117 K. H. Michel and B. Verberck, *Phys. Rev. B: Condens. Matter Mater. Phys.*, 2009, **80**, 224301.
- 118 L. Boldrin, F. Scarpa, R. Chowdhury and S. Adhikari, *Nanotechnology*, 2011, **22**, 505702.
- 119 C. Li, Y. Bando, C. Zhi, Y. Huang and D. Golberg, *Nanotechnology*, 2009, **20**, 385707.
- 120 C. Lee, Q. Li, W. Kalb, X.-Z. Liu, H. Berger, R. W. Carpick and J. Hone, *Science*, 2010, **328**, 76.
- 121 A. P. M. Barboza, H. Chacham, C. K. Oliveira, T. F. D. Fernandes, E. H. M. Ferreira, B. S. Archanjo, R. J. C. Batista, A. B. de Oliveira and B. R. A. Neves, *Nano Lett.*, 2012, **12**, 2313.
- 122 L. H. Li, Y. Chen, G. Behan, H. Zhang, M. Petracic and A. M. Glushenkov, *J. Mater. Chem.*, 2011, **21**, 11862.
- 123 X. Chen, J. F. Dobson and C. L. Raston, *Chem. Commun.*, 2012, **48**, 3703.
- 124 H. Yurdakul, Y. Goncu, O. Durukan, A. Akay, A. T. Seyhan, N. Ay and S. Turan, *Ceram. Int.*, 2012, **38**, 2187.
- 125 (a) J. Y. Huang, H. Yasuda and H. Mori, *J. Am. Ceram. Soc.*, 2000, **83**, 403; (b) J. Ghosh, S. Mazumdar, M. Das, S. Ghatak and A. K. Basu, *Mater. Res. Bull.*, 2008, **43**, 1023.
- 126 (a) A. N. Streletskeii, D. G. Permenov, B. B. Bokhonov, I. V. Kolbaney, A. V. Leonov, I. V. Berestetskaya and K. A. Streletzky, *J. Alloys Compd.*, 2009, **483**, 313; (b) A. N. Streletskeii, D. G. Permenov, K. A. Streletzky, B. B. Bokhonov and A. V. Leonov, *Colloid J.*, 2010, **72**, 544.
- 127 A. N. Streletskeii, D. G. Permenov, B. B. Bokhonov, A. V. Leonov and S. N. Mudretsova, *Colloid J.*, 2010, **72**, 553.
- 128 R. J. Smith, P. J. King, M. Lotya, C. Wirtz, U. Khan, S. De, A. O'Neill, G. S. Duesberg, J. C. Grunlan, G. Moriarty, J. Chen, J. Wang, A. I. Minett, V. Nicolosi and J. N. Coleman, *Adv. Mater.*, 2011, **23**, 3944.
- 129 G. Lian, X. Zhang, M. Tan, S. Zhang, D. Cui and Q. Wang, *J. Mater. Chem.*, 2011, **21**, 9201.
- 130 Y. Lin, T. V. Williams and J. W. Connell, unpublished results.
- 131 S. D. Bergin, V. Nicolosi, P. V. Streich, S. Giordani, Z. Sun, A. H. Windle, P. Ryan, N. P. P. Niraj, Z.-T. T. Wang, L. Carpenter, W. J. Blau, J. J. Boland, J. P. Hamilton and J. N. Coleman, *Adv. Mater.*, 2008, **20**, 1876.
- 132 K.-G. Zhou, N.-N. Mao, H.-X. Wang, Y. Peng and H.-L. Zhang, *Angew. Chem., Int. Ed.*, 2011, **50**, 10839.
- 133 Y. Wang, Z. Shi and J. Yin, *J. Mater. Chem.*, 2011, **21**, 11371.
- 134 (a) S. Park and R. S. Ruoff, *Nat. Nanotechnol.*, 2009, **4**, 217; (b) Y. Zhu, S. Murali, W. Cai, X. Li, J. W. Suk, J. R. Potts and R. S. Ruoff, *Adv. Mater.*, 2010, **22**, 3906.
- 135 G.-X. Li, Y. Liu, B. Wang, X.-M. Song, E. Li and H. Yan, *Appl. Surf. Sci.*, 2008, **254**, 5299.
- 136 A. Pakdel, C. Zhi, Y. Bando, T. Nakayama and D. Golberg, *ACS Nano*, 2011, **5**, 6507.
- 137 (a) R. C. Dutta, S. Khan and J. K. Singh, *Fluid Phase Equilib.*, 2011, **302**, 310; (b) M. C. Gordillo and J. Marti, *Phys. Rev. E: Stat. Nonlinear, Soft Matter Phys.*, 2011, **84**, 011602; (c) H. Li and X. C. Zeng, *ACS Nano*, 2012, **6**, 2401.
- 138 T. Yoshizaki, H. Watanabe and T. Nakagawa, *Inorg. Chem.*, 1968, **7**, 422.
- 139 (a) S.-Y. Xie, W. Wang, K. A. S. Fernando, X. Wang, Y. Lin and Y.-P. Sun, *Chem. Commun.*, 2005, 3670; (b) S. Pal, S. R. C. Vivekchand, A. Govindaraj and C. N. R. Rao, *J. Mater. Chem.*, 2007, **17**, 450; (c) X. Wu, W. An and X. C. Zeng, *J. Am. Chem. Soc.*, 2006, **128**, 12001; (d) T. Ikuno, T. Sainsbury, D. Okawa, J. M. Frechet and A. Zettl, *Solid State Commun.*, 2007, **142**, 643; (e) A. Maguer, E. Leroy, L. Bresson, E. Doris, A. Loiseau and C. Mioskowski, *J. Mater. Chem.*, 2009, **19**, 1271.
- 140 Y. Zhao, X. Wu, J. Yang and X. C. Zeng, *Phys. Chem. Chem. Phys.*, 2012, **14**, 5545.
- 141 K. A. Simonov, N. A. Vinogradov, M. L. Ng, A. S. Vinogradov, N. Mårtensson and A. B. Preobrajenski, *Surf. Sci.*, 2012, **606**, 564.
- 142 C. Zhi, Y. Bando, C. Tang, R. Xie, T. Sekiguchi and D. Golberg, *J. Am. Chem. Soc.*, 2005, **127**, 15996.
- 143 X. Li, X. Wang, L. Zhang, S. Lee and H. Dai, *Science*, 2008, **319**, 1229.
- 144 Q. Lin, X. Zou, G. Zhou, R. Liu, J. Wu, J. Li and W. Duan, *Phys. Chem. Chem. Phys.*, 2011, **13**, 12225.
- 145 J. M. G. Hernández, G. H. Cocoletzi and E. C. Anota, *J. Mol. Model.*, 2012, **18**, 137.
- 146 (a) M. Zheng, A. Jagota, E. D. Semke, B. A. Diner, R. S. McLean, S. R. Lustig, R. E. Richardson and N. G. Tassi, *Nat. Mater.*, 2003, **2**, 338; (b) X. Tu and M. Zheng, *Nano Res.*, 2008, **1**, 185; (c) T. Ahmed, S. Kilina, T. Das, J. T. Haraldsen, J. J. Rehr and A. V. Balatsky, *Nano Lett.*, 2012, **12**, 927.

- 147 A. Nag, K. Raidongia, K. P. S. S. Hembram, R. Datta, U. V. Waghmare and C. N. R. Rao, *ACS Nano*, 2010, **4**, 1539.
- 148 L. Jiao, L. Zhang, X. Wang, G. Diankov and H. Dai, *Nature*, 2009, **458**, 877.
- 149 S. Azadi and R. Moradian, *Phys. Lett. A*, 2010, **374**, 605.
- 150 (a) M. Sakamoto, J. S. Speck and M. S. Dresselhaus, *J. Mater. Res.*, 1986, **1**, 685; (b) G. L. Doll, J. S. Speck, G. Dresselhaus, M. S. Dresselhaus, K. Nakamura and S.-I. Tanuma, *J. Appl. Phys.*, 1989, **66**, 2554; (c) C. Shen, S. G. Mayorga, R. Biagioni, C. Piskoti, M. Ishigami, A. Zettl and N. Bartlett, *J. Solid State Chem.*, 1999, **147**, 74; (d) B.-Q. Dai and G.-L. Zhang, *Mater. Chem. Phys.*, 2002, **78**, 304; (e) E. Budak and C. Bozkurt, *J. Solid State Chem.*, 2004, **177**, 1768; (f) F. Oba, A. Togo, I. Tanaka, K. Watanabe and T. Taniguchi, *Phys. Rev. B: Condens. Matter Mater. Phys.*, 2010, **81**, 075125; (g) S. Okada and M. Otani, *Phys. Rev. B: Condens. Matter Mater. Phys.*, 2010, **81**, 233401; (h) B. Altintas, C. Parlak, C. Bozkurt and R. Eryigit, *Eur. Phys. J. B*, 2011, **79**, 301; (i) A. Sumiyoshi, H. Hyodo and K. Kimura, *J. Solid State Chem.*, 2012, **187**, 208.
- 151 M. J. Rand and J. F. Roberts, *J. Electrochem. Soc.*, 1968, **115**, 423.
- 152 (a) S. P. S. Arya and A. D'Amico, *Thin Solid Films*, 1988, **157**, 267; (b) C. Oshima and A. Nagashima, *J. Phys.: Condens. Matter*, 1997, **9**, 1.
- 153 G. Giovannetti, P. A. Khomyakov, G. Brocks, P. J. Kelly and J. van den Brink, *Phys. Rev. B: Condens. Matter Mater. Phys.*, 2007, **76**, 073103.
- 154 C. R. Dean, A. F. Young, I. Meric, C. Lee, L. Wang, S. Sorgenfrei, K. Watanabe, T. Taniguchi, P. Kim, K. L. Shepard and J. Hone, *Nat. Nanotechnol.*, 2010, **5**, 722.
- 155 A. Mayorov, R. V. Gorbachev, S. V. Morozov, L. Britnell, R. Jalil, L. A. Ponomarenko, P. Blake, K. S. Novoselov, K. Watanabe, T. Taniguchi and A. K. Geim, *Nano Lett.*, 2011, **11**, 2396.
- 156 K. H. Lee, H.-J. Shin, J. Lee, I.-Y. Lee, G.-H. Kim, J.-Y. Choi and S.-W. Kim, *Nano Lett.*, 2012, **12**, 714.
- 157 (a) W. Auwärter, M. Muntwiler, J. Osterwalder and T. Greber, *Surf. Sci.*, 2003, **545**, L735; (b) W. Auwärter, H. U. Suter, H. Sachdev and T. Greber, *Chem. Mater.*, 2004, **16**, 343.
- 158 S. Chatterjee, Z. Luo, M. Acerce, D. M. Yates, A. T. C. Johnson and L. G. Sneddon, *Chem. Mater.*, 2011, **23**, 4414.
- 159 G. Dong, E. B. Fourre, F. C. Tabak and J. W. M. Frenken, *Phys. Rev. Lett.*, 2010, **104**, 096102.
- 160 P. Sutter, J. Lahiri, P. Albrecht and E. Sutter, *ACS Nano*, 2011, **5**, 7303.
- 161 Y.-H. Lee, K.-K. Liu, A.-Y. Lu, C.-Y. Wu, C.-T. Lin, W. Zhang, C.-Y. Su, C.-L. Hsu, T.-W. Lin, K.-H. Wei, Y. Shi and L.-J. Li, *RSC Adv.*, 2012, **2**, 111.
- 162 O. V. Yazyev and A. Pasquarello, *Phys. Rev. B: Condens. Matter Mater. Phys.*, 2009, **80**, 035408.
- 163 F. Müller, S. Hüfner, H. Sachdev, S. Gsell and M. Schreck, *Phys. Rev. B: Condens. Matter Mater. Phys.*, 2010, **82**, 075405.
- 164 M. Corso, W. Auwärter, M. Muntwiler, A. Tamai, T. Greber and J. Osterwalder, *Science*, 2004, **303**, 217.
- 165 R. Laskowski, P. Blaha, T. Gallauer and K. Schwarz, *Phys. Rev. Lett.*, 2007, **98**, 106802.
- 166 A. B. Preobrazenski, A. S. Vinogradov, M. L. Ng, E. Ćavar, R. Westernström, A. Mikkelsen, E. Lundgren and N. Mårtensson, *Phys. Rev. B: Condens. Matter Mater. Phys.*, 2007, **75**, 245412.
- 167 A. Goriachko, Y. He, M. Knapp, H. Over, M. Corso, T. Brugger, S. Berner, J. Osterwalder and T. Greber, *Langmuir*, 2007, **23**, 2928.
- 168 S. Berner, M. Corso, R. Widmer, O. Groening, R. Laskowski, P. Blaha, K. Schwarz, A. Goriachko, H. Over, S. Gsell, M. Schreck, H. Sachdev, T. Greber and J. Osterwalder, *Angew. Chem., Int. Ed.*, 2007, **46**, 5115.
- 169 T. Brugger, H. Ma, M. Iannuzzi, S. Berner, A. Winkler, J. Hutter, J. Osterwalder and T. Greber, *Angew. Chem., Int. Ed.*, 2010, **49**, 6120.
- 170 R. Laskowski, P. Blaha and K. Schwarz, *Phys. Rev. B: Condens. Matter Mater. Phys.*, 2008, **78**, 045409.
- 171 F. Müller, S. Hüfner, H. Sachdev, R. Laskowski, P. Blaha and K. Schwarz, *Phys. Rev. B: Condens. Matter Mater. Phys.*, 2010, **82**, 113406.
- 172 A. B. Preobrazenski, M. A. Nesterov, M. L. Ng, A. S. Vinogradov and N. Mårtensson, *Chem. Phys. Lett.*, 2007, **446**, 119.
- 173 D. Martoccia, T. Brugger, M. Björck, C. M. Schleputz, S. A. Pauli, T. Greber, B. D. Patterson and P. R. Willmott, *Surf. Sci.*, 2010, **604**, L16.
- 174 F. Muller, S. Hufner and H. Sachev, *Surf. Sci.*, 2009, **603**, 425.
- 175 M. Corso, T. Greber and J. Osterwalder, *Surf. Sci.*, 2005, **577**, L78.
- 176 M. Morscher, M. Corso, T. Greber and J. Osterwalder, *Surf. Sci.*, 2006, **600**, 3280.
- 177 E. Ćavar, R. Westernström, A. Mikkelsen, E. Lundgren, A. S. Vinogradov, M. L. Ng, A. B. Preobrazenski, A. A. Zakharov and N. Mårtensson, *Surf. Sci.*, 2008, **602**, 1722.
- 178 R. Laskowski and P. Blaha, *Phys. Rev. B: Condens. Matter Mater. Phys.*, 2010, **81**, 075418.
- 179 N. A. Vinogradov, A. A. Zakharov, M. L. Ng, A. Mikkelsen, E. Lundgren, N. Mårtensson and A. B. Preobrazenski, *Langmuir*, 2012, **28**, 1775.
- 180 T. Greber, M. Corso and J. Osterwalder, *Surf. Sci.*, 2009, **603**, 1373.
- 181 D. Martoccia, S. A. Pauli, T. Brugger, T. Greber, B. D. Patterson and P. R. Willmott, *Surf. Sci.*, 2010, **604**, L9.
- 182 A. Goriachko, A. A. Zakharov and H. Over, *J. Phys. Chem. C*, 2008, **112**, 10423.
- 183 O. Bunk, M. Corso, D. Martoccia, R. Herger, P. R. Willmott, B. D. Patterson, J. Osterwalder, J. F. van der Veen and T. Greber, *Surf. Sci.*, 2007, **601**, L7.
- 184 R. Widmer, S. Berner, O. Groning, T. Brugger, J. Osterwalder and T. Greber, *Electrochim. Commun.*, 2007, **9**, 2484.
- 185 H. Dil, J. Lobo-Checa, R. Laskowski, P. Blaha, S. Berner, J. Osterwalder and T. Greber, *Science*, 2008, **319**, 1824.
- 186 M. L. Ng, A. B. Preobrazenski, A. A. Zakharov, A. S. Vinogradov, S. A. Krasnikov, A. A. Cafolla and N. Mårtensson, *Phys. Rev. B: Condens. Matter Mater. Phys.*, 2010, **81**, 115449.
- 187 (a) A. Goriachko, Y. B. He and H. Over, *J. Phys. Chem. C*, 2008, **112**, 8147; (b) M. L. Ng, A. B. Preobrazenski, A. S. Vinogradov and N. Mårtensson, *Surf. Sci.*, 2008, **602**, 1250; (c) H. P. Koch, R. Laskowski, P. Blaha and K. Schwarz, *Phys. Rev. B: Condens. Matter Mater. Phys.*, 2011, **84**, 245410; (d) B. Wang and M.-L. Bocquet, *J. Phys. Chem. Lett.*, 2011, **2**, 2341.
- 188 I. Brihuega, C. H. Michaelis, J. Zhang, S. Bose, V. Sessi, J. Honolká, M. A. Schneider, A. Enders and K. Kern, *Surf. Sci.*, 2008, **602**, L95.
- 189 H. Ma, T. Brugger, S. Berner, Y. Ding, M. Iannuzzi, J. Hutter, J. Osterwalder and T. Greber, *ChemPhysChem*, 2010, **11**, 399; Y. Ding, M. Iannuzzi and J. Hutter, *J. Phys. Chem. C*, 2011, **115**, 13685.
- 190 A. J. Pollard, E. W. Perkins, N. A. Smith, A. Saywell, G. Goretzki, A. G. Phillips, S. P. Argent, H. Sachdev, F. Müller, S. Hüfner, S. Gsell, M. Fischer, M. Schreck, J. Osterwalder, T. Greber, S. Berner, N. R. Champness and P. H. Beton, *Angew. Chem., Int. Ed.*, 2010, **49**, 1794.
- 191 A. B. Preobrazenski, M. L. Ng, A. S. Vinogradov and N. Mårtensson, *Phys. Rev. B: Condens. Matter Mater. Phys.*, 2008, **78**, 073401; T. Brugger, S. Gunther, B. Wang, J. H. Dil, M.-L. Bocquet, J. Osterwalder, J. Wintterlin and T. Greber, *Phys. Rev. B: Condens. Matter Mater. Phys.*, 2009, **79**, 045407.
- 192 R. Gao, L. Yin, C. Wang, Y. Qi, N. Lun, L. Zhang, Y.-X. Liu, L. Kang and X. Wang, *J. Phys. Chem. C*, 2009, **113**, 15160.
- 193 Z. Zhao, Z. Yang, Y. Wen and Y. Wang, *J. Am. Ceram. Soc.*, 2011, **94**, 4496.
- 194 J. Yu, L. Qin, Y. Hao, S. Kuang, X. Bai, Y.-M. Chong, W. Zhang and E. Wang, *ACS Nano*, 2010, **4**, 414.
- 195 L. Qin, J. Yu, M. Li, F. Liu and X. Bai, *Nanotechnology*, 2011, **22**, 215602.
- 196 J. Lin, Y. Huang, J. Zhang, F. Shi, S. Wei, J. Gao, Z. Huang, X. Ding and C. Tang, *Mater. Chem. Phys.*, 2008, **108**, 440.
- 197 Y. Zhu, Y. Bando, L. Yin and D. Golberg, *Nano Lett.*, 2006, **6**, 2982.
- 198 Z.-G. Chen and J. Zou, *J. Mater. Chem.*, 2011, **21**, 1191.
- 199 Z.-G. Chen, J. Zou, G. Liu, F. Li, Y. Wang, L. Wang, X.-L. Yuan, T. Sekiguchi, H.-M. Cheng and G. Q. Lu, *ACS Nano*, 2008, **2**, 2183.
- 200 L. Wang, C. Sun, L. Xu and Y. Qian, *Catal. Sci. Technol.*, 2011, **1**, 1119.
- 201 X. Wang, C. Zhi, L. Li, H. Zeng, C. Li, M. Mitome, D. Golberg and Y. Bando, *Adv. Mater.*, 2011, **23**, 4072.
- 202 W.-Q. Han, H.-G. Yu and Z. Liu, *Appl. Phys. Lett.*, 2011, **98**, 203112.
- 203 W. Han, Y. Bando, K. Kurashima and T. Sato, *Appl. Phys. Lett.*, 1998, **73**, 3085.
- 204 (a) R. B. Kaner, J. Kouvetakis, C. E. Warble, M. L. Sattler and N. Bartlett, *Mater. Res. Bull.*, 1987, **22**, 399; (b) A. Y. Liu, R. M. Wentzcovitch and M. L. Cohen, *Phys. Rev. B: Condens. Matter Mater. Phys.*, 1989, **39**, 1760; (c) Y. Miyamoto, A. Rubio,

- M. L. Cohen and S. G. Louie, *Phys. Rev. B: Condens. Matter Mater. Phys.*, 1994, **50**, 4976.
- 205 (a) O. Stephan, P. M. Ajayan, C. Colliex, P. Redlich, J. M. Lambert, P. Bernier and P. Lefin, *Science*, 1994, **266**, 1683; (b) K. Suenaga, C. Colliex, N. Demonty, A. Loiseau, H. Pascard and F. Willaime, *Science*, 1997, **278**, 654.
- 206 (a) A. Nagashima, Y. Gamou, M. Terai, M. Wakabayashi and C. Oshima, *Phys. Rev. B: Condens. Matter Mater. Phys.*, 1996, **54**, 13491; (b) C. Oshima, A. Itoh, E. Rokuta, T. Tanaka, K. Yamashita and T. Sakurai, *Solid State Commun.*, 2000, **116**, 37; (c) T. Kawasaki, T. Ichimura, H. Kishimoto, A. K. Akbar, T. Ogawa and C. Oshima, *Surf. Rev. Lett.*, 2002, **9**, 1459; (d) T. Tanaka, A. Ito, A. Tajima, E. Rokuta and C. Oshima, *Surf. Rev. Lett.*, 2003, **10**, 721.
- 207 L. Ci, L. Song, C. Jin, D. Jariwala, D. Wu, Y. Li, A. Srivastava, Z. F. Wang, K. Storr, L. Balicas, F. Liu and P. M. Ajayan, *Nat. Mater.*, 2010, **9**, 430.
- 208 L. Qin, J. Yu, S. Kuang, C. Xiao and X. Bai, *Nanoscale*, 2012, **4**, 120.
- 209 A. Pakdel, X. Wang, C. Zhi, Y. Bando, K. Watanabe, T. Sekiguchi, T. Nakayama and D. Golberg, *J. Mater. Chem.*, 2012, **22**, 4818.
- 210 X. Wei, M.-S. Wang, Y. Bando and D. Golberg, *ACS Nano*, 2011, **5**, 2916.
- 211 T.-W. Lin, C.-Y. Su, X.-Q. Zhang, W. Zhang, Y.-H. Lee, C.-W. Chu, H.-Y. Lin, M.-T. Chang, F.-R. Chen and L.-J. Li, *Small*, 2012, **8**, 1384.
- 212 S. Wang, L. Zhang, Z. Xia, A. Roy, D. W. Chang, J.-B. Baek and L. Dai, *Angew. Chem., Int. Ed.*, 2012, **51**, 4209.
- 213 J. D. R. Martins and H. Chacham, *ACS Nano*, 2011, **5**, 385.
- 214 Y. Liu, S. Bhowmick and B. I. Yakobson, *Nano Lett.*, 2011, **11**, 3113.
- 215 W. H. Brito, R. Kagimura and R. H. Miwa, *Phys. Rev. B: Condens. Matter Mater. Phys.*, 2012, **85**, 035404.
- 216 J. Li and V. B. Shenoy, *Appl. Phys. Lett.*, 2011, **98**, 013105.
- 217 S. Cahangirov and S. Ciraci, *Phys. Rev. B: Condens. Matter Mater. Phys.*, 2011, **83**, 165448.
- 218 J. Zhu, S. Bhandary, B. Sanyal and H. Ottosson, *J. Phys. Chem. C*, 2011, **115**, 10264.
- 219 J. He, K.-Q. Chen, Z.-Q. Fan, L.-M. Tang and W. P. Hu, *Appl. Phys. Lett.*, 2010, **97**, 193305.
- 220 A. K. Manna and S. K. Pati, *J. Phys. Chem. C*, 2011, **115**, 10842.
- 221 Z. M. Liu, Y. Zhu and Z. Q. Yang, *J. Chem. Phys.*, 2011, **134**, 074708.
- 222 S. Bhowmick, A. K. Singh and B. I. Yakobson, *J. Phys. Chem. C*, 2011, **115**, 9889.
- 223 P. P. Shinde and V. Kumar, *Phys. Rev. B: Condens. Matter Mater. Phys.*, 2011, **84**, 125401.
- 224 G. Seol and J. Guo, *Appl. Phys. Lett.*, 2011, **98**, 143107.
- 225 Y. Fan, M. Zhao, X. Zhang, Z. Wang, T. He, H. Xia and X. Liu, *J. Appl. Phys.*, 2011, **110**, 034314.
- 226 S. Junghawan, S. Limpijumnong and J.-L. Kuo, *Phys. Rev. B: Condens. Matter Mater. Phys.*, 2011, **84**, 235424.
- 227 Z. Yu, M. L. Hu, C. X. Zhang, C. Y. He, L. Z. Sun and J. Zhong, *J. Phys. Chem. C*, 2011, **115**, 10836.
- 228 Y. Liu, X. Wu, Y. Zhao, X. C. Zeng and J. Yang, *J. Phys. Chem. C*, 2011, **115**, 9442.
- 229 E. A. Basheer, P. Parida and S. K. Pati, *New J. Phys.*, 2011, **13**, 053008.
- 230 S. Jun, X. Li, F. Meng and C. V. Ciobanu, *Phys. Rev. B: Condens. Matter Mater. Phys.*, 2011, **83**, 153407.
- 231 B. Huang, H. Lee, B.-L. Gu, F. Liu and W. Duan, *Nano Res.*, 2012, **5**, 62.
- 232 J. M. Pruneda, *Phys. Rev. B: Condens. Matter Mater. Phys.*, 2010, **81**, 161409.
- 233 J. M. Pruneda, *Phys. Rev. B: Condens. Matter Mater. Phys.*, 2012, **85**, 045422.
- 234 M. Modarresi, M. R. Roknabadi and N. Shahtahmasbi, *Physica E*, 2011, **43**, 1751.
- 235 M. Qiu and K. M. Liew, *J. Appl. Phys.*, 2011, **110**, 064319.
- 236 E.-J. Kan, X. Wu, Z. Li, X. C. Zeng, J. Yang and J. G. Hou, *J. Chem. Phys.*, 2008, **129**, 084712.
- 237 A. Ramasubramaniam and D. Naveh, *Phys. Rev. B: Condens. Matter Mater. Phys.*, 2011, **84**, 075405.
- 238 J. Li, G. Zhou, Y. Chen, B.-L. Gu and W. Duan, *J. Am. Chem. Soc.*, 2009, **131**, 1796.
- 239 Y.-J. Li, Q.-Q. Sun, L. Chen, P. Zhou, P.-F. Wang, S.-J. Ding and D. W. Zhang, *AIP Adv.*, 2012, **2**, 012191.
- 240 S. D. Sarma and E. H. Hwang, *Phys. Rev. B: Condens. Matter Mater. Phys.*, 2011, **83**, 121405.
- 241 P. Lu, Z. Zhang, C. H. Woo and W. Guo, *J. Phys. Chem. C*, 2012, **116**, 626.
- 242 J. Xue, J. Sanchez-Yamagishi, D. Bulmash, P. Jacquod, A. Deshpande, K. Watanabe, T. Taniguchi, P. Jarillo-Herrero and B. J. LeRoy, *Nat. Mater.*, 2011, **10**, 282.
- 243 R. Decker, Y. Wang, V. W. Brar, W. Regan, H.-Z. Tsai, Q. Wu, W. Gannett, A. Zettl and M. F. Crommie, *Nano Lett.*, 2011, **11**, 2291.
- 244 E. Kim, T. Yu, E. S. Song and B. Yu, *Appl. Phys. Lett.*, 2011, **98**, 262103.
- 245 M. Son, H. Lim, M. Hong and H. C. Choi, *Nanoscale*, 2011, **3**, 3089.
- 246 (a) S. Tang, G. Ding, X. Xie, J. Chen, C. Wang, X. Ding, F. Huang, W. Lu and M. Jiang, *Carbon*, 2012, **50**, 329; (b) X. Ding, G. Ding, X. Xie, F. Huang and M. Jiang, *Carbon*, 2011, **49**, 2522; (c) X. Ding, H. Sun, X. Xie, H. Ren, F. Huang and M. Jiang, *Phys. Rev. B: Condens. Matter Mater. Phys.*, 2011, **84**, 174417.
- 247 Z. Yan, Z. Peng, Z. Sun, J. Yao, Y. Zhu, Z. Liu, P. M. Ajayan and J. M. Tour, *ACS Nano*, 2011, **5**, 8187.
- 248 Z. Liu, L. Song, S. Zhao, J. Huang, L. Ma, J. Zhang, J. Lou and P. M. Ajayan, *Nano Lett.*, 2011, **11**, 2032.
- 249 T. Lin, Y. Wang, H. Bi, D. Wan, F. Huang, X. Xie and M. Jiang, *J. Mater. Chem.*, 2012, **22**, 2859.
- 250 L. Britnell, R. V. Gorbachev, R. Jalil, B. D. Belle, F. Schedin, A. Mishchenko, T. Georgiou, M. I. Katsnelson, L. Eaves, S. V. Morozov, N. M. R. Peres, J. Leist, A. K. Geim, K. S. Novoselov and L. A. Ponomarenko, *Science*, 2012, **335**, 947.
- 251 L. A. Ponomarenko, A. K. Geim, A. A. Zhukov, R. Jalil, S. V. Morozov, K. S. Novoselov, I. V. Grigorieva, E. H. Hill, V. V. Cheianov, V. I. Fal'ko, K. Watanabe, T. Taniguchi and R. V. Gorbachev, *Nat. Phys.*, 2011, **7**, 958.
- 252 F. Amet, J. R. Williams, A. G. F. Garcia, M. Yankowitz, K. Watanabe, T. Taniguchi and D. Goldhaber-Gordon, *Phys. Rev. B: Condens. Matter Mater. Phys.*, 2012, **85**, 073405.
- 253 M. Bokdam, P. A. Khomyakov, G. Brocks, Z. Zhong and P. J. Kelly, *Nano Lett.*, 2011, **11**, 4631.
- 254 J. Ślawińska, I. Zasada and Z. Klusek, *Phys. Rev. B: Condens. Matter Mater. Phys.*, 2010, **81**, 155433.
- 255 H. Behera and G. Mukhopadhyay, *J. Phys. Chem. Solids*, 2012, **73**, 818.
- 256 D. Usachov, V. K. Adamchuk, D. Haberer, A. Gruneis, H. Sachdev, A. B. Preobrajenski, C. Laubschat and D. V. Vyalikh, *Phys. Rev. B: Condens. Matter Mater. Phys.*, 2010, **82**, 075415.
- 257 N. Kharche and S. K. Nayak, *Nano Lett.*, 2011, **11**, 5274.
- 258 Z. Zhang, X. C. Zeng and W. Guo, *J. Phys. Chem. C*, 2011, **115**, 21678.
- 259 J. E. Padilha, R. B. Pontes and A. Fazzio, *J. Phys.: Condens. Matter*, 2012, **24**, 075301.
- 260 J. Ślawińska, I. Zasada, P. Kosiński and Z. Klusek, *Phys. Rev. B: Condens. Matter Mater. Phys.*, 2010, **82**, 085431.
- 261 A. Ramasubramaniam, D. Naveh and E. Towe, *Nano Lett.*, 2011, **11**, 1070.
- 262 R. Quhe, J. Zheng, G. Luo, Q. Liu, R. Qin, J. Zhou, D. Yu, S. Nagase, W.-N. Mei, Z. Gao and J. Lu, *NPG Asia Mater.*, 2012, **4**, e6.
- 263 B. Sachs, T. O. Wehling, M. I. Katsnelson and A. I. Lichtenstein, *Phys. Rev. B: Condens. Matter Mater. Phys.*, 2011, **84**, 195414.
- 264 M. Yankowitz, J. Xue, D. Cormode, J. D. Sanchez-Yamagishi, K. Watanabe, T. Taniguchi, P. Jarillo-Herrero, P. Jacquod and B. J. LeRoy, *Nat. Phys.*, 2012, **8**, 382.
- 265 (a) H. Hatta, M. Taya, F. A. Kulacki and J. F. Harder, *J. Compos. Mater.*, 1992, **26**, 612; (b) H. Ishida and S. Rimdusit, *Thermochim. Acta*, 1998, **320**, 177; (c) K. Sato, H. Horibe, T. Shirai, Y. Hotta, H. Nakano, H. Nagai, K. Mitsuishi and K. Watari, *J. Mater. Chem.*, 2010, **20**, 2749; (d) H.-B. Cho, T. Nakayama, Y. Tokoi, S. Endo, S. Tanaka, T. Suzuki, W. Jiang, H. Suematsu and K. Niihara, *Compos. Sci. Technol.*, 2010, **70**, 1681; (e) H.-B. Cho, N. C. Tu, T. Fujihara, S. Endo, T. Suzuki, S. Tanaka, W. Jiang, H. Suematsu, K. Niihara and T. Nakayama, *Mater. Lett.*, 2011, **65**, 2426; (f) H.-B. Cho, Y. Tokoi, S. Tanaka, T. Suzuki, W. Jiang, H. Suematsu, K. Niihara and T. Nakayama, *J. Mater. Sci.*, 2011, **46**, 2318; (g) H.-B. Cho, Y. Tokoi, S. Tanaka, H. Suematsu, T. Suzuki, W. Jiang, K. Niihara and T. Nakayama, *Compos. Sci. Technol.*, 2011, **71**, 1046; (h) C. Kizilkaya, Y. Mülazim,

- M. V. Kahraman, N. K. Apohan and A. Güngör, *J. Appl. Polym. Sci.*, 2012, **124**, 706.
- 266 T. Kuilla, S. Bhadra, D. Yao, N. H. Kim, S. Bose and J. H. Lee, *Prog. Polym. Sci.*, 2010, **35**, 1350.
- 267 (a) A. Yu, P. Ramesh, M. E. Itkis, E. Bekyarova and R. C. Haddon, *J. Phys. Chem. C*, 2007, **111**, 7565; (b) S. Kim and L. T. Drzal, *Sol. Energy Mater. Sol. Cells*, 2009, **93**, 136; (c) L. M. Veca, M. J. Meziani, W. Wang, X. Wang, F. Lu, P. Zhang, Y. Lin, R. Fee, J. W. Connell and Y.-P. Sun, *Adv. Mater.*, 2009, **21**, 2088; (d) L. Tian, P. Anilkumar, L. Cao, C. Y. Kong, M. J. Meziani, H. J. Qian, L. M. Veca, T. J. Thorne, K. N. Tackett, II, T. Edwards and Y.-P. Sun, *ACS Nano*, 2011, **5**, 3052.
- 268 M. S. R. N. Kiran, K. Raidongia, U. Ramamurti and C. N. R. Rao, *Scr. Mater.*, 2011, **64**, 592.
- 269 J. Taha-Tijerina, T. N. Narayanan, G. Gao, M. Rohde, D. A. Tsentalovich, M. Pasquali and P. M. Ajayan, *ACS Nano*, 2012, **6**, 1214.
- 270 (a) G. G. Wildgoose, C. E. Banks and R. G. Compton, *Small*, 2006, **2**, 182; (b) V. Georgakilas, D. Gournis, V. Tzitzios, L. Pasquato, D. Guldi and M. Prato, *J. Mater. Chem.*, 2007, **17**, 2679; (c) P. V. Kamat, *J. Phys. Chem. Lett.*, 2010, **1**, 520; (d) S. Bai and X. Shen, *RSC Adv.*, 2012, **1**, 64.
- 271 M. Gao, A. Lyalin and T. Taketsugu, *J. Phys. Chem. C*, 2012, **116**, 9054.
- 272 Y. Lin, K. A. Watson, M. J. Fallbach, S. Ghose, J. G. Smith, D. M. Delozier, W. Cao, R. E. Crooks and J. W. Connell, *ACS Nano*, 2009, **3**, 871.
- 273 Y. Lin, K. A. Watson, S. Ghose, J. G. Smith, T. V. Williams, R. E. Crooks, W. Cao and J. W. Connell, *J. Phys. Chem. C*, 2009, **113**, 14858.
- 274 Y. Lin, D. W. Baggett, J.-W. Kim, E. J. Siochi and J. W. Connell, *ACS Appl. Mater. Interfaces*, 2011, **3**, 1652.
- 275 X. Wang, S. M. Tabakman and H. Dai, *J. Am. Chem. Soc.*, 2008, **130**, 8152.
- 276 H. Liu, K. Xu, X. Zhang and P. D. Ye, *Appl. Phys. Lett.*, 2012, **100**, 152115.
- 277 M. Terrones, J.-C. Charlier, A. Gloter, E. Cruz-Silva, E. Terres, Y. B. Li, A. Vinu, Z. Zanolli, J. M. Dominguez, H. Terrones, Y. Bando and D. Golberg, *Nano Lett.*, 2008, **8**, 1026.
- 278 H. Chen, H. Zhang, L. Fu, Y. Chen, J. S. Williams, C. Yu and D. Yu, *Appl. Phys. Lett.*, 2008, **92**, 243105.
- 279 Y. Xu, Z. Guo, H. Chen, Y. Yuan, J. Lou, X. Lin, H. Gao, H. Chen and B. Yu, *Appl. Phys. Lett.*, 2011, **99**, 133109.
- 280 J. Yu, Y. Chen, R. G. Elliman and M. Petracic, *Adv. Mater.*, 2006, **18**, 2157.
- 281 G.-J. Zhang, *J. Am. Ceram. Soc.*, 2009, **92**, 745.
- 282 (a) P. Wang, S. Orimo, T. Matsushima, H. Fujii and G. Majer, *Appl. Phys. Lett.*, 2002, **80**, 318; (b) P. Wang, S. Orimo and H. Fujii, *Appl. Phys. A: Mater. Sci. Process.*, 2004, **78**, 1235.
- 283 (a) D. Neiner, A. Karkamkar, J. C. Linehan, B. Arey, T. Autrey and S. M. Kauzlarich, *J. Phys. Chem. C*, 2009, **113**, 1098; (b) D. Neiner, A. Luedtke, A. Karkamkar, W. Shaw, J. Wang, N. D. Browning, T. Autrey and S. M. Kauzlarich, *J. Phys. Chem. C*, 2010, **114**, 13935.
- 284 S. A. Shevlin and Z. X. Guo, *Phys. Rev. B: Condens. Matter Mater. Phys.*, 2007, **76**, 024104.
- 285 N. S. Venkataraman, M. Khazaei, R. Sahara, H. Mizuseki and Y. Kawazoe, *Chem. Phys.*, 2009, **359**, 173.
- 286 K. R. Koswattage, I. Shimoyama, Y. Baba, T. Sekiguchi and K. Nakagawa, *J. Chem. Phys.*, 2011, **135**, 014706.
- 287 Y. A. Wu, A. I. Kirkland, F. Schäffel, K. Porfyrakis, N. P. Young, G. A. D. Briggs and J. H. Warner, *Nanotechnology*, 2011, **22**, 195603.
- 288 M. Engler, C. Lesniak, R. Damasch, B. Ruisinger and J. Eichler, *CFI, Ceram. Forum Int.*, 2007, **84**, E49.